Effect of extracellular vesicles on cancer cell lines *in vitro* and biodistribution in an ectopic osteosarcoma mouse model

by

Javier Abello

B.S., Nacional University of Colombia, 2005

AN ABSTRACT OF A DISSERTATION

submitted in partial fulfillment of the requirements for the degree

DOCTOR OF PHILOSOPHY

Department of Food, Nutrition, Dietetics and Health
College of Human Ecology

KANSAS STATE UNIVERSITY
Manhattan, Kansas

2018

Abstract

Human umbilical cord-derived mesenchymal stromal cells (HUC-MSCs) have an enormous therapeutic potential because of their immunomodulatory and anti-inflammatory properties. However, there are limitations for their therapeutic use due to low cell survival after implantation, the risk of culture-borne pathogens, and the risk of embolism and thrombosis after intravenous infusion. Exosomes, on the other hand, constitute an important part of the MSCs secretome and may play a role in their therapeutic effects. Here, it was demonstrated that HUC-MSC-derived exosomes accumulate in human and mouse osteosarcoma cell lines *in vitro* and reduce their proliferation. The distribution of HUC-MSCs exosomes was shown in osteosarcoma tumor-bearing mice. Exosome distribution *in vivo* was observed using Magnetic Resonance Imaging (MRI) of gadolinium-labeled exosomes and by fluorescent imaging after infusion of near infrared dye-labeled exosomes. HUC-MSC exosomes accumulated in the tumor throughout the 48 hours post-injection period. In contrast, synthetic lipid nanoparticle accumulates in tumor only for the first 3 hours post-injection. In summary, this study showed that HUC-MSCs exosomes can accumulate to osteosarcoma cells *in vitro* and *in vivo*, and thus they may be useful for detecting cancer metastasis.

Effect of extracellular vesicles on cancer cell lines *in vitro* and biodistribution in ectopic osteosarcoma mouse model

by

Javier Abello

B.S., National University of Colombia, 2005

A DISSERTATION

submitted in partial fulfillment of the requirements for the degree

DOCTOR OF PHILOSOPHY

Department of Food, Nutrition, Dietetics and Health
College of Human Ecology

KANSAS STATE UNIVERSITY
Manhattan, Kansas

2018

Approved by:

Co-Major Professor
Tonatiuh Melgarejo

Approved by:

Co-Major Professor
Mark Haub

Copyright

Abstract

Human umbilical cord-derived mesenchymal stromal cells (HUC-MSCs) have an enormous therapeutic potential because of their immunomodulatory and anti-inflammatory properties. However, there are limitations for their therapeutic use due to low cell survival after implantation, the risk of culture-borne pathogens, and the risk of embolism and thrombosis after intravenous infusion. Exosomes, on the other hand, constitute an important part of the MSCs secretome and may play a role in their therapeutic effects. Here, it was demonstrated that HUC-MSC-derived exosomes accumulate in human and mouse osteosarcoma cell lines *in vitro* and reduce their proliferation. The distribution of HUC-MSCs exosomes was shown in osteosarcoma tumor-bearing mice. Exosome distribution *in vivo* was observed using Magnetic Resonance Imaging (MRI) of gadolinium-labeled exosomes and by fluorescent imaging after infusion of near infrared dye-labeled exosomes. HUC-MSC exosomes accumulated in the tumor throughout the 48 hours post-injection period. In contrast, synthetic lipid nanoparticle accumulates in tumor only for the first 3 hours post-injection. In summary, this study showed that HUC-MSCs exosomes can accumulate to osteosarcoma cells *in vitro* and *in vivo*, and thus they may be useful for detecting cancer metastasis.

Table of Contents

List of Figures

List of Tables

List of Abbreviations

AO: acridine orange

BCA: bicinchoninic acid protein assay

BSA: bovine serum albumen fraction V

CM: cell-conditioned medium

DAPI: 4’,6-diamidino-2-phenylindole

ddH_2O: double distilled water

DiR: diIC18(7) (1,1'-dioctadecyl-3,3,3',3'-tetramethylindotricarbocyanine iodide)

DLS: dynamic light scattering

DMEM: dulbecco's modified eagle medium

DOTA: 1,4,7,10-tetraazacyclododecane-1,4,7,10-tetraacetic acid

DPBS: dulbecco's phosphate-buffered saline

dpHPL: pooled human platelet lysate depleted of exosomes

DSPE: 1,2-distearoylphosphatidylethanolamine

Exo-GdL: exosomes labeled with gadolinium lipid

Exo-RhB: exosomes labeled with rhodamine B

FA: flip angle

FLASH: flash slow angle shot

FMO: fluorescence minus one control

GdL: gadolinium lipid

GNPs: gadolinium oxide nanoparticles

HUC: human umbilical cord

ICP-MS: inductively coupled plasma mass spectrometry

LDS: sample loading buffer

m-IgG BP-HRP: mouse IgG kappa binding protein conjugated to horseradish peroxidase

MRI: magnetic resonance imaging; MSCs: mesenchymal stromal cells

MSC: mesenchymal stromal cell

MTT: (3-(4,5-dimethylthiazol-2-yl)-2,5-diphenyltetrazolium bromide)

NHS: N-hydroxysuccinimide

NIR: near infrared

NSF: nephrogenic systemic fibrosis

NTA: nanoparticle tracking analysis

PBS: phosphate-buffered salin

PDI: polydispersity index

PEGNP: pegylated nanoparticles

PEGNP: PEGylated nanoparticles

PI: propidium iodide

PVDF: polyvinylidene difluoride

RARE: acquisition with relaxation enhancement

RhB: rhodamine B

RIPA: radioimmunoprecipitation assay buffer

TE: echo time

TEM: transmission electron microscopy

TR: repetition time

VEGF: vascular endothelial growth factor

ZP: zeta potential

Acknowledgements

First, I want to thank doctor Mark Weiss for all the time and energy that he has invested in this process. Also I want to give my most heartfelt thank you to Dr. Mark Haub for the financial support and his guide. He was always there for me, his door was always open. This achievement would not be possible without the support of Dr. Anika Linde and Dr. Tonatiuh Melgarejo. They were light when I was surrounded by darkness. Next, I want to thank to Dr. Santosh Aryal for his support and knowledge. Also I want to thank to Juan David Muñoz for all this years of support. Finally, want to thank to my friends, especially to Tuyen Nguyen for her help with my experiments, and for being such a wonderful person. Special thanks to Departments of Food, Nutrition, Dietetics and Health and the Department of Anatomy and Physiology.

Dedication

To: Rodolfo Candela

Because you gave me the strength to continue

1. Introduction

1.1. History of EVs research

To talk about extracellular vesicles, and in particularly exosomes, it is necessary to understand the concept and the evolution of this research. The earliest report of extracellular vesicles (EVs) was in 1946 by the biochemist, Erwin Chargaff, who identify that a hemophiliac's blood could coagulate after adding the fraction obtained by ultracentrifugation of normal blood [1]. In 1967, Peter Wolf described the formation of microparticles, which he referred to as "platelet dust", as product of platelet activation [2]. In 1983, Pan and Johnstone's discovery of the externalization of the transferrin receptor during maturation of reticulocytes *in vitro* was the first report of the presence of microvesicles [3]. The term "exosome" was first used in 1981 by Trams *et al.* to describe the formation of microvesicles from murine and human primary cell cultures and cancer cell lines [4]. Then in 1987, Johnstone *et al.* proposed that the vesicles formed during the maturation of reticulocytes works as a selective mechanism of protein secretion [5]. In 1966 the secreted membrane vesicles were called outer membrane vesicles (OMV) in gram-negative bacteria [6]. The formation of similar structures that were delimited by membrane was reported in 1969 in cartilage and bones of rodents; those structures were later named "matrix vesicles" [7]. One of the most important discoveries was by Raposo *et al*. in 1996, they isolated exosomes from conditioned media of B-lymphocytes and showed that they were involved in antigen presentation. This finding indicated the involvement of exosomes in communication between immune cells [8]. In 2006, Ratajczak et al. demonstrated that embryonic stem cell-derived microvesicles carried mRNAs that were involved in the survival and the maintenance of potency of hematopoietic progenitor cells [9]. A year later Valadi et al. demonstrated that exosomes were involved in the genetic exchange between cells by tracking mRNA and microRNA transfer in human (HMC-1) and murine (MC/9) mast cell lines, bone marrow mast cells (BMMC) and $CD4^+$-T cells [10]. Importantly, RNAs were

not the only nucleic acids found in exosomes. In 2010 it was reported that exosomes from glioblastoma (U87MG) and primary rat astrocytes carried mitochondrial DNA [11]. In 2011 Balaj *et al*. demonstrated that exosomes isolated from medulloblastoma, melanoma and primary glioblastoma cells carried coding and non-coding DNAs, as well as mutated oncogene sequences, and transposable elements that may be involved in tumor progression [12]. In 2014 it was reported that chronic myelogenous leukemia (CML) exosomes contain double stranded DNAs that are directly associated with the mutational status of the tumor [13]. In 2015 Hoshino et al. showed that exosomes participate in organotropic metastasis of cancer. Their research suggested that exosomes possess a particular membrane "address" based on proteins that confer recognition of the preferable target tissues for metastasis [14].

1.2. Classification of Extracellular vesicles based on Their Biogenesis and

1.2.1. Function

The advances in the field of membrane vesicle research over the last 30 years has been significant, as discussed above. However, there is confusion about the differences in naturally occurring bioparticles. Some people have classified these vesicles by size. Unfortunately, classification by size has been a source of confusion because of the size overlap between different vesicle types. In this section, I discuss classification of membrane vesicles based on their biogenesis and function.

1.2.2. Extracellular vesicles (EVs)

In 2011 the term "EVs" was coined by Gyorgy *et al*. in an attempt to unify the naming system of secreted membrane vesicles, which was formerly proposed by Thery *et al*. in 2009. By definition, EVs are spherical structures produced and secreted by cells. EVs are enclosed by a lipid bilayer membrane and contain proteins, lipids, sugars and other molecules acquired during their biogenesis [15]. EVs have been identified in virtually

all living organisms from gram-positive bacteria, Archaea, Fungi [16, 17], mammals [18] and more recently in apoplastic fluids of leaves of *Arabidopsis thaliana* [19]. While the functions of EVs are diverse, complex and still under investigation, their main function is signaling between cells [15, 20]. EVs fit under an umbrella that includes microvesicles, ectosomes, endosomes, exosomes, apoptotic bodies, among others. There is a big concern among the scientific community regarding the nomenclature of these vesicles and there is a need to establish a consensus naming plan is avoid misunderstandings. For example, In the case of exosomes isolated from insects, Andrulis *et al.* reported the production of these EVs in *Drosophila melanogaster* [21, 22]. However, the "exosomes" described in this ***Nature*** paper are a 3'-5' exoribonucleases complex that degrade mRNAs in *Drosophila melanogaster*, and they are not exosomes [23].

1.2.3. Microvesicles

There are two differentiating characteristics between macrovesicles (MVs) and exosomes. First is their origin. Exosomes are generated as intraluminal vesicles (ILVs) in the late endosome, MVs are generated by directly budding of the plasma membrane [24]. Second, the release mechanism differs between the two. In exosomes it occurs by the fusion of the multivesicular bodies (MVBs), which does not happened with microvesicles. Recently was demonstrated that the protease activated receptor 2 (PAR2) is involved in the production of pro-metastatic MVs in cancer cells. The activation of PAR2 start a downstream metabolic pathway that involves phosphorylation of the protein kinase B (AKT), which subsequently activates Rab5a [25]. Interestingly, it was demonstrated that some proteins involved in the secretion of exosomes also are involved in the biogenesis of MVs. Such is the case of the neutral sphingomyelin phosphodiesterase (nSMase) -2 and 3. It was determined that the inhibition of nSMases induce the production of MVs and inhibit the production of exosomes [26]. Cytokines play an important role in cell communication and immune response. However, the role of cytokines in the production of MVs was just recently identified. Apparently, both pro-

and anti-inflammatory cytokines such as IFN-γ, IL-4, IL-13, IL-27, IL-23, and TGF-β can trigger the production of MVs in myeloid cells. Additionally, the mechanism activated by cytokines seems to be independent of the plasma membrane receptor P2R72, which is a strong stimulant of inflammation [27].

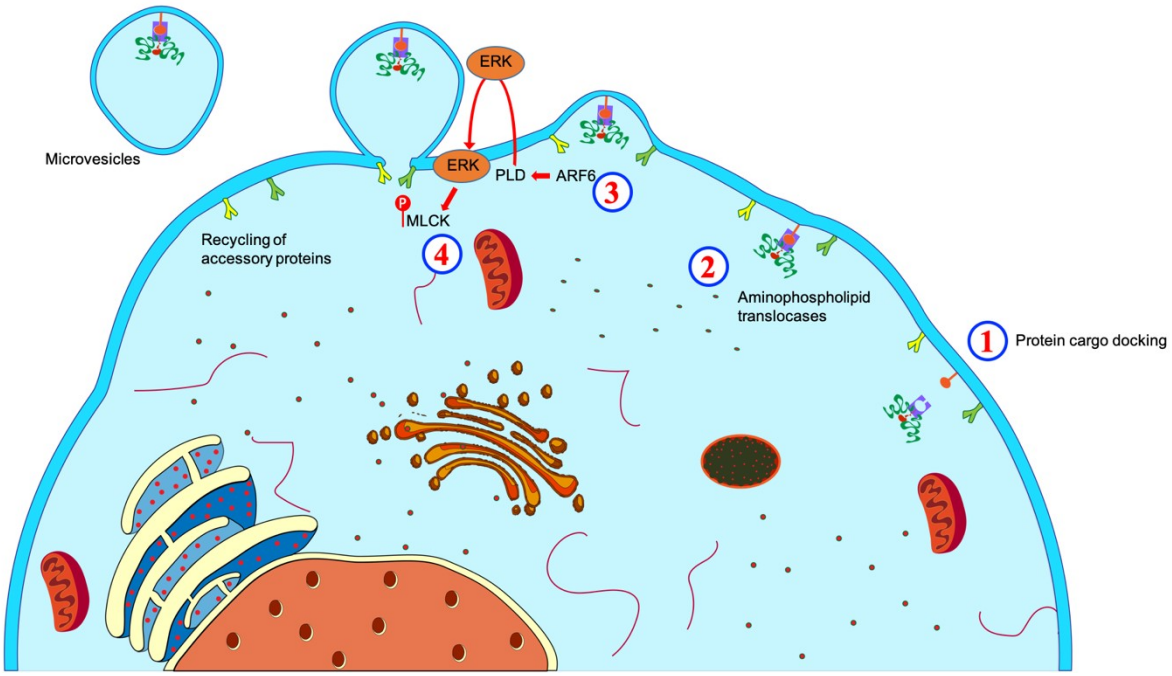

Figure 1. Schematic representation of the microvesicle biogenesis. Microvesicles are formed by the direct budding of the plasma membrane. This is a process that involves the re-arranchement of proteins, phospholipids, and the cytoskeleton. 1) Apparently, the redistribution of cargo has an effect on the initiation of the curvature of the plasma membrane. 2) Membrane curvature toward vesicle formation begins with the translocation of phosphatidylserine to the outside part of the plasma membrane by flippases. 3) Rho family member GTP-binding protein ADP-ribosylation factor 6 (ARF6) initiates a signaling cascade that starts with the activation of phospholipase-D and the subsequent recruits the extracellular signal-regulated kinase (ERK)

to the plasma membrane. 4) ERK phosphorylates and activates myosin light-chain kinase (MLCK) which triggers the release of microvesicles.

1.2.4. Exosomes

The term "exosomes" describes small spheroid particles between 30-150 nm in size. Exosomes have been isolated from many biological fluids including urine, semen, milk, blood, plasma and cerebral spinal fluid [28]. The production of exosomes is complex and starts in the early endosome followed by the formation of intraluminar vesicles (ILVs) and subsequently the formation of multivesicular bodies (MVBs). Either these MVBs fuse with lysosomes for degradation or they fuse with the plasma membrane to release the exosomes extracellularly. The physiological regulation of exosomes formation is a subject of study, and some of the important steps on their biogenesis have been elucidated. For example, the formation of the MVBs orchestrated by the endosomal sorting complexes required for transport (ESCRT) or utilize an alternative pathway independent of ESCRT [29]. These are reviewed below.

1.2.4.1. ESCRT-dependent pathway

The endosomal sorting complex is formed from 5 subunits: ESCRT-0 to -III and the vacuole protein sorting 4 (Vps4) [30]. Each member of the ESCRT machinery links to each other in a scaffold fashion to generate MVBs. First, ESCRT-0 recognizes ubiquitin molecules on the endosomal membrane and binds them. Then ESCRT-0 recruits ESCRT-1 complex and recruits ESCRT-II. ESCRT-II forms two arms that link with ubiquitinated membrane proteins and then retracts from the endosomal membrane to form intraluminal vesicles. ESCRT-II activates ESCRT-III complex, which is assembled on the endosomal membrane. ESCRT-III complex associates with deubiquitinases that remove and recycle the ubiquitin tag from the membrane proteins after vesicle formation. Finally, the Vps4 complex mediates the disassembly ESCRT-III

from the plasma membrane through its ATPase activity. This results in the release of the vesicle into the endosomal lumen forming the MBVs [30]. Recently Wenzel *et al.* proposed a model based on the ESCRT kinetics to describe the formation of the ILVs. On the first phase of the model, hepatocyte growth factor receptor substrate (HRS) and clathrin accumulate on the endosome membrane to facilitate cargo sorting and membrane deformation. In phase two, ESCRT-III recruits VPS4A to constrict the membrane and cut it to release the formed ILVs into the MVB. This study demonstrated that ESCRTs are recruited constantly during the formation of the ILVs and apparently, the lapses of the subunits engagement during this process mark the timing and size of the ILVs. Additionally, the authors demonstrated that clathrin determines the dissociation time of ESCRT-0 [31]. Another important step in the ILVs formation is the recruitment of the Syndecan-syntenin-ALIX complex. This complex supports endosome membrane budding and cleavage by disconnecting the ILVs' cargo after ESCRT-III has been assemble to the neck of the vesicle under formation [32]. The interaction between syntenin and ALIX is regulated by the GTPase, ADP ribosylation factor 6 (ARF6), and its effector, phospholipase D2 (PLD2) [33]. Because PLD2 metabolizes phosphatidylcholine into phosphatidic acid (PA), and since the vesicles are enriched in PA, it is plausible that PLD2 is involved in exosome biogenesis [33]. One important aspect of the ESCRT pathway is how the cargo proteins are transfer between the different subunits of the complex. Recently, flotillin-1, an integral membrane protein, was showed to be involved in the recognition and sorting of the ubiquitinated proteins between ESCRT-0 and-1 or toward the lysosome. After stimulation with epidermal growth factor (EGF), HRS and tumor susceptibility gene 101 (TSG101) protein product are inactivated by ubiquitination, which prevents their interaction with the ubiquitinated cargo. Apparently, the role of flotillin-1 is activate HRS and TSG101 by removing their ubiquitin label [34]. Even though the ESCRT pathway has been extensively studied, it is not the only mechanism to traffic proteins and cargo. Other pathways has been proposed and are summarized below.

1.2.4.2. ESCRT-independent pathway

While the ESCRT-dependent mechanism is involved in exosome biogenesis, as summarized above, the components in that pathway are mostly accessory and integral proteins. Cellular and endosomal membranes, e.g., lipids, also play an important role in exosome synthesis. As their role is summarized below. Studies where the ESCRT pathway was disrupted by depleting the cells of various ESCRT subunits showed that MVBs continued to be formed. For example, the inhibition of the internalization of the epidermal growth factor receptor (EGFR), which uses an ESCRT-dependent mechanism, ESCRT-depleted cells formed different-size vesicles in the MVBs. The conclusion is that different pathways are involved in vesicle formation [35]. It was demonstrated the role of ceramides in the cargo sorting to the MVBs or towards the lysosome for degradation. This pathway does not require ESCRT complexes. In this study the authors track the trafficking of the proteolipid protein (PLP) in naturally PLP-enriched mouse oligodendroglial cells. The disruption of ESCRT machinery did not have an effect in the intraluminal accumulation of PLP. The lipid profile by Nano-Electrospray Ionization Tandem Mass Spectrometry (Nano-ESI MS/MS) of exosomes obtained from oligodendroglial cells revealed the enrichment of lipids in the exosomes, specially, ceramides. In order to determine the role of ceramides on exosomes, the authors treated the cells with a neutral sphyngomyelinase inhibitor (GW4869). There was a significant reduction in the production of exosomes. Additionally, when the sphyngomyelinase inhibitor 2 was truncated by RNAi, there was a reduction of PLP content in exosomes. This result indicates the role of ceramides not only in the production of exosomes but also in cargo sorting [36]. In another study the role of the activation of Gi-couple sphingosine 1-phosphate receptors (S1R) in exosomes biogenesis was shown. In this study the inhibition of Sphingosine kinase 2 (SPHK2), which is a potent activator of S1R, had a remarkable effect on the sorting of CD63 into ILVs, with the subsequent alteration on cargo sorting to the exosomes [37]. Recently, the same group demonstrated that post activation of S1R, its β and γ subunits interact with Rho GTPases, which triggers the formation of F-actin networks required for the MVBs sorting of cargo into exosomes [38].

In summary, there are different mechanisms involved in the production of extracellular vesicles. It is possible that the type of vesicle and its function directly relates to cellular metabolic pathway that participate in the process. In addition, with the extensive involvement of extracellular vesicles in different metabolic process such as cell communication, cell adhesion, molecular interchange and antigen presentation, EVs clearly play an important role in the cellular metabolic homeostasis.

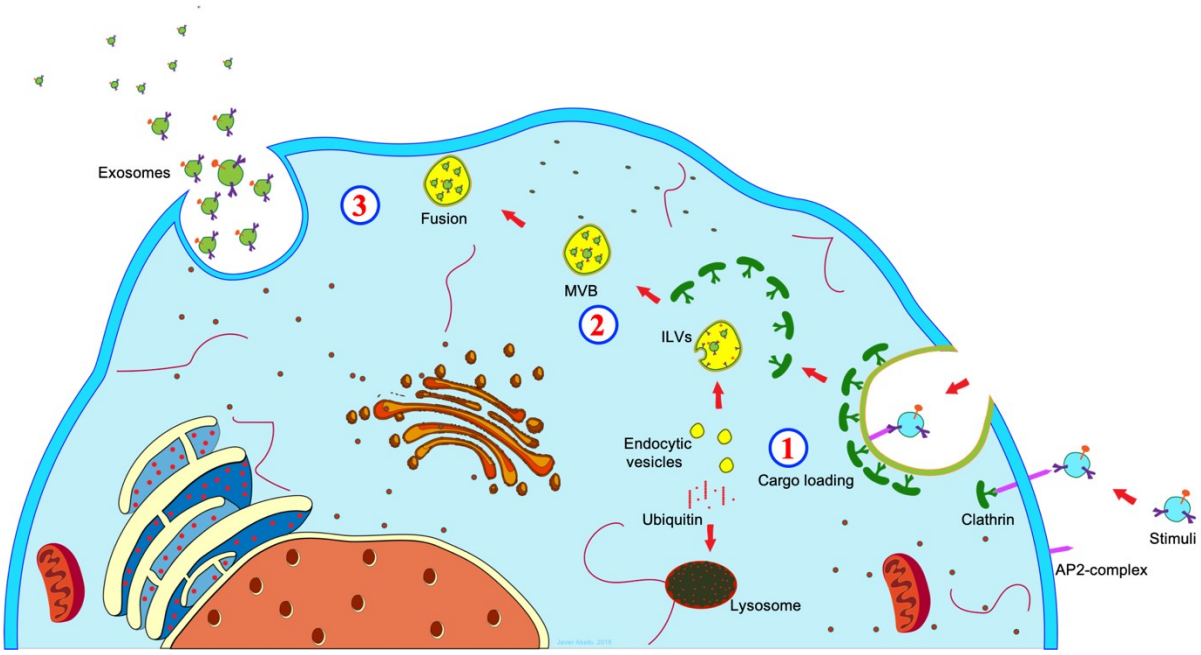

Figure 2. Schematic representation of exosome biogenesis. Exosomes are formed within the endosomal network. 1) The cargo is loaded into the early endosomes by internalization or by fusion with endocytic vesicles. 2) The early endosomes subdivide within small interluminal vesicles (ILVs) forming the multivesicular bodies (MVBs). 3) Exosomes are released from late endosomal compartment through the fusion of MVBs with the plasma membrane. A key step in ILVs formation is the reorganization of endosomal membrane protein CD9- and CD63- enriched microdomains. Next, the endosomal sorting complex required for transport, or ESCRTs, are

recruited to the site of budding in a scaffold fashion to complete the process and release the formed vesicles. This complex is recruited during the ILVs formation and during exosome secretion.

1.3. Mesenchymal Stromal Cells (MSCs)

1.3.1. Definition

Mesenchymal stromal cells (MSCs) were first described by Friedenstein as a subpopulation of cells similar to fibroblasts isolated from bone marrow (reviewed in [39]). The International Society for Cellular Therapy (ISCT) proposed a minimal definition of MSCs. Under their guidelines, MSCs must: 1) adhere to tissue culture treated plastic plates and self-renew, 2) stain positively for certain "mesenchymal" surface markers: endoglin (CD105), ecto-5'nucleotidase (CD73), Thy1 (CD90), and the receptor for hyaluronic acid (CD44), and not stain for surface markers of hematopoietic cells: CD45, CD34, CD14 or CD11b, CD79a or CD19 and HLA class II, and 3) exhibit differentiation capability to adipocytes, chondrocytes and osteocytes [40]. Morphologically, three distinctive cell shapes are noted: 1) triangular or star-like shapes, 2) fibroblastic shaped, e.g., a spindle-shaped, and 3) large, and flat [41]. There is controversy about whether MSCs are stem cells. Some authors refer to this population as stem cells, however, because the stem cells are found at low frequency compared with the remaining population, its more accepted to use the acronym MSCs to refer to the total population of stromal cells [42]. The main function of MSCs is to bring support and maintenance to the tissues. However, these cells also play an important role in the hematopoietic and immune system. For instance, in the bone marrow MSCs work as an important regulator of the hematopoietic progenitor cells by the production and secretion of cytokines [43].

1.3.2. Sources of MSCs.

Because the stroma is a connective tissue, it is natural to find MSCs in different tissues. The first tissue where MSCs were isolated was the bone marrow [39]. However, since that discovery MSCs were isolated from adipose tissue [44], amniotic fluid [45], Wharton's Jelly [46], umbilical cord blood [47], and others. Stromal tissue is located everywhere in the body, it is possible to obtain MSCs from different tissue sources. Compare with other tissue sources, the HUC-MSCs have a higher percentage of proliferating cells that can be maintained for more passages prior to senescence. In respect to their potential application as therapeutic tools, HUCs, similar to other tissue-derived MSCs exhibit immunomodulatory properties[48, 49] and have the potential to control autoimmune diseases, such as Crohn's disease [50], multiple sclerosis [51, 52] and rheumatoid arthritis [53, 54]. The question remains open as to whether MSCs from these different origins are the same or do MSCs from different tissues differ? In this regard, Kim *et al.* compared the immunological characteristics, pluripotency and immunophenotype of MSCs from periodontal ligament (PDLSC), umbilical cord (UC), and adipose tissue (AT). They showed that upon stimulation with IFN-γ, MSCs from PDLSC and AD, but not from UC, upregulated MHC-I and -II. Additionally, after implantation of UC-MSCs in mice, the expression of pro-inflammatory cytokines was slightly upregulated [55]. Another study compared the bone regeneration ability between "stem" cells from human exfoliated deciduous teeth (SHED), human dental pulp stem cells (hDPSCs) and human bone marrow mesenchymal stem cells (hBMSCs) and found no significant differences in bone formation between the sources. However, they found a difference MSCs marker expression between SHED and hDPSCs [56]. Even more interesting are the results obtained by Taneselli *et al*. who compared canine AT-MSC derived from either subcutaneous (Sc) fat or visceral (Vs) fat. They found that MSCs from Sc exhibit better

differentiation to bone, as indicated by superior mineralization *in vitro* [57]. To summarize, the tissue source of the MSCs may determine the characteristics of the cells.

1.3.3. MSCs Function

The use of MSCs as a cell therapy or "regenerative medicine" is not just a matter of convenience or because of the difficulty associated with implementation of embryonic stem cells. The main reason why MSCs are used is their safety and their capacity to adapt to their environment. The functions of MSCs were reviewed by Spees *et al.* as three major mechanisms: 1) paracrine activity, 2) mitochondria transferring by tunneling nanotubes (TNT) and 3) transferring of exosomes and microvesicles [58]. The source of the MSCs may affect the secretion and production of cytokines. In a study that compared the production of VEGF and TGF-β by MSCs from umbilical cord (UC-MSCs), amniotic membrane (AM-MSCs) and adipose tissue (AT-MSCs), UC-MCSs had the lowest production of VEGF compared with the other MSCs. In contrast, TGF-β was expressed at higher levels in AM-MSCs and UC-MSCs. This suggests that the paracrine secretome may vary depending of the MSC tissue source [59].

In addition to their paracrine secretions, MSCs also communicate via direct cell to cell contacts. MSCs can extended nanotubes to exchange metabolic products and organelles with adjacent cells [60]. For instance, bone marrow MSCs (BM-MSCs) can affect the survival of H9c2 cardiomyocytes in an ischemia/reperfusion injury model via TNT supplied mitochondria. TNT are formed by MSCs placed under stressful conditions: When the H9c2 cells were cocultured with BM-MSCs, the formation of TNT was associated with reduction of H9c2 apoptosis. Fluorescent mitochondria from the BM-MSCs migrated into the H9c2 cells via TNT. When the BM-MSCs were treated with latruculin-A, a TNT inhibitor, the H9c2 apoptosis increased. This simple, elegant experiment provided evidence of the TNT mechanism [61]. In another study, MSCs were

shown to induce phagocytic activity in macrophages by mitochondria transfer via TNT in an *in vivo* mouse model of *E. coli* pneumonia. Thus, the protective effect of MSCs may be due in part to their ability to form TNT and exchange mitochondria to stressed or damaged cells [62].

In recent years the advances in EVs research provided new understanding about the mechanisms used by MSCs. Exosomes transport coding and non-coding nucleic acids such as miRNAs, plus proteins, lipids, and others signaling molecules. Recently the role of miRNAs from MSCs-derived exosomes in their osteogenic differentiation was investigated. Exosomes from conditioned media stimulated human MSCs and increased alkaline phosphatase (ALP) activity and extracellular matrix mineralization. The RNA profiling of the exosomes showed downregulation of miR-31 and miR-144, which are inhibitors of osteogenic differentiation, and its promoted when miR-221 is downregulated, which has been identified to attenuate osteogenic differentiation [63]. In another study was demonstrated that BM-MSCs derived exosomes can promoted cardio-protection in mouse model of myocardial infarction, apparently trough mechanisms that involve miR-21a-5p, which target genes of the apoptotic pathway [64]. The protective effect of exosomes through miRNAs was also demonstrated in mouse model of acute liver failure (ALF). RNA analysis revealed that miR-17 was found in naive exosomes isolated from mouse AT-MSCs but not in exosomes obtained from AT-MSCs transfected with miR-17 inhibitor. This finding suggests that exosomal miR-17 may mediate MSC affects on the inflammatory response [65].

1.3.4. Clinical significance immunomodulatory effect of MSCs

The constant and rapid development in the stem cell field provides new tools to advance the areas of regenerative medicine and therapeutics. However, there is a gap in our understanding of the biological process that underlies their beneficial effects, not only at the cellular level but also at

the level of tissues, organs, and systems. To the date there are 7385 registered clinical trials that involve different sources of MSCs according to the ClinicalTrials.gov website. 2516 MSC clinical trials have been completed, of which 7 % were Phase 3 trials (ClinicalTrials.gov). There are several reasons that MSCs are widely used in regenerative medicine. First, MSCs can be isolated from many different tissues, in the majority of the cases by a simple surgical procedure or even through non-invasive methods such as the case of umbilical cord, squamous dental pulp and neonatal foreskin. One of the most important characteristics of MSCs is their interaction with the immune system and their innate anti-inflammatory and immunomodulatory effects. Most of their effects on the immune system are mediated by their secretome which is composed of growth factors, cytokines, nucleic acids and EVs, among others. For example, was demonstrated that monocytes that were cocultured with primed UC-MSCs exhibit upregulation of the genes PD-L1, CD90, IL-1b, IL-6, IL-8, IL-10, and TGF-β. In contrast, the expression of TNF-α was down regulated. When those monocytes were implanted in mice was noted that the monocytes stimulated cells of the adaptive immune system [66]. In a clinical trial was evaluated the effect of HUC-MSCs implantation on patient with liver cirrhosis caused by hepatitis B. The authors indicate that considering that hepatitis virus its not the direct responsible for liver damage and rather that occurs because of the inflammatory effect of lymphocytes and monocytes. In this study was observed that patiencients are characterized by extremely high levels of TGF-β and IL-10 as well as high amount of peripheral Treg cells. However, after treatment with HUC-MSCs the levels of IL-6, TNF-α and T-cells $CD8^+$ were considerable reduced [49]. This clinical trial proved the reliability of the therapeutic effect of MSCs and opened the possibility of implement those in the control of autoimmune diseases. Another advantage of MSCs is their innate capacity to respond and adapt to different stimuli by varying their phenotype. MSCs priming and the shifting between anti- and pro-

inflamatory phenotypes has been ample study [50, 51]. It was demonstrated the effect on equine MSCs (E-MSCs) of cell priming through TLR-3 and -4 receptors. E-MSCs stimulated TLR-4 suppressed the proliferation of lymphocytes *in vitro*. MHC-II^{+} MSCs exhibit high immunomodulatory effect when compared with the MHC-II^{-}. With respect to the genetic expression, there was an upregulation of IL-6, IL-8, CCL2 and CXCL10 genes in both stimulated pathways [52].

Despite the evidence that MSCs provide therapeutic benefits, there are concerns for the potential of adverse effects, such as embolism, disease transmission, or cancer [67-69]. Has been demonstrated that UC-MSCs had anticancer properties [70-72]. Furthermore, after intravenous MSC injection, the cells get trapped in lung and other organs with high capillarity for at least 24 hours after infusion [73, 74]. Recently, the therapeutic effect of MSCs was shown to be, in part, due to the production and secretion of bioactive compounds and extracellular vesicles, rather than for the cellular differentiation and expansion after implantation [75-78]. Exosomes, are part of the MSCs secretome and appear to mediate some of their physiological effects [79, 80]. As was mention before, exosomes are formed in the endosome, and their membrane shares similar attributes with the parental cell membrane including transmembrane (e.g., integrins and tetraspanins) and peripheral proteins (e.g., Lactadherin), lipids (e.g., phosphatidylserines), glycans (e.g., polylactosamine), among others, that play an important role in cell signaling and communication [81-85]. For the last decade, the cargo of exosomes has been an important subject of research because of its involvement in different metabolic process [86, 87], and variation of the cargo correlates to changes in the inter- and external cell environment [88, 89]. It has been demonstrated the important role of EVs, especially exosomes in cell to cell communication [90], antigen presentation [91, 92], cell adhesion [93], gene silencing [94], tissue remodeling [95] and

cancer progression [96]. Furthermore, MSC exosomes have been shown to affect human osteosarcoma cell proliferation *in vitro* [97].

1.4. Cancer

1.4.1. Incidence of cancer worldwide.

Cancer is by definition the uncontrolled growth of cells. Cancer development provokes inflammation in the affected tissue, and the inflammatory response triggers changes in tissue vascularity. Both the inflammatory response and the unchecked cell growth results in tumor formation. Cancer is a progressive disease and its progressive nature is associated with genetic mutations in tumor-suppressor or cell cycle checkpoint regulation genes, and these genes are called "oncogenes" [98]. In most of the cases, cellular hyperplasia is the hallmark sign of cancer, along with atypical or disorganized tissue morphology. As the disease progresses, the abnormal cell growth generates tissue dysplasia and the invasion of secondary interstitial cells, followed by tumor formation [99]. Finally, tumor cells may migrate and colonize other tissues to form secondary disease in a process called "metastasis" [99]. The different types of cancers are parsed based on their tissue of origin. For instance, carcinoma is a cancer of epithelial tissues. This type of cancer can be subdivided in adeno-carcinoma, adeno- referring to glands, and squamous carcinoma, which affect tissues that are protected by squamous epithelium [100]. Sarcoma is a type of cancer that affects sarco- or connective tissues [101]. Lymphomas affect tissues of the lymph system [102]. Leukemia is a type of cancer that originates in bone marrow and affects blood cells [103].

Cancer is a devastating family of diseases. In 2015, 8.8 million deaths were associated with cancer, worldwide [104]. Cancer does not discriminate against gender, race or age. While the incidence of cancer in the United States has declined slightly since the 1990s, it is still the second most common cause of death [104]. It has been estimated that in 2018 in United States, 609,640 people will die from cancer [104], and that cancer will

kill 13 million people in the world by 2030 [105]. The most common cancer in the world is lung cancer, causing more that 1.69 million deaths in 2015 [106]. The next most prevalent types of cancer are: liver cancer 788,000 deaths, colorectal cancer with an estimate of 774,000 deaths and stomach cancer with 754,000 deaths [107].

1.4.2. Mechanisms underlying cancer

To understand the genetic mutations that govern cancer development and progression, it is necessary first to identify the mechanisms occurring at the cellular level. In 2000 Hanahan and Weinberg proposed the "Hallmarks of cancer", which describes the properties that cancer must possess to determine their fate [108, 109]. One of the main characteristics acquired by cancer cells is "hyperplasia" or uncontrolled, excessive cell growth. This process occurs by the mutation of some genes known as pro-oncogenes that in normal conditions regulate the cell cycle. After those genes are mutated, they are called "oncogenes" or cancer-promoting genes. These mutated genes remove the "brakes" or the normal regulation of the cell cycle and their progeny continue proliferating unchecked. The pro-oncogenes may act at different points in the cell cycle regulatory pathway. For instant, mutating the gene inhibiting either growth factor (GF) stimuli or the growth factor receptor (GFR) can produce excess cell growth. These mutations may occur at the level of the signal transduction or at the nuclear transcription level. Normally, growth factors act as a signal to induce cell proliferation in a paracrine fashion. However, in cancer progression the growth factor signaling dependency is lost. For example, the mutation of neurofibromatosis type 1 gene (NF1) in glioblastoma cells induces the secretion of platelet-derived growth factor AA (PDGF-AA) and interleukin-8 (IL-8), which are involved in tumor angiogenesis and inflammatory cell recruitment [110]. In ovarian cancer metastasis, the over-expression of transforming growth factor-alpha (TGF-α) and a feedback loop with stromal fibroblasts promote peritoneal metastasis through epidermal growth factor receptor (EGFR) signaling [111]. Another oncogenic mechanism includes

mutations of the receptor tyrosine kinase (RTK). The mutation causes permanent kinase activity and the subsequent production of the mitogenic signaling. For instance, gastrointestinal stromal tumors (GISTs) are caused by the activity of the mutated KIT Proto-oncogene Receptor Tyrosine Kinase (kit) in the Golgi apparatus [112]. An additional mechanism directly involves the signal-traducing proteins downstream of the RTK. In the case of pancreatic adenocarcinoma, the over-expression of the onco-protein KRAS (Kirsten Rat Sarcoma virus) induces cancer progression and tumor formation. KRAS is over-expressed by establishing a regulatory loop with an isoform of the translation elongation factor (eIF5A) and the tyrosine kinase PEAK1 signaling [113]. Growth suppressors, too, regulate the proliferation of normal cells acting at different phases of the cell cycle. An example of these suppressors is the gene p53, whose function is to induce cell cycle arrest at the G1/S checkpoint (reviewed in [114]). Activation of p53 pauses the cell cycle to permit DNA repair or the induction of apoptosis. Mutation of p53 prevents DNA repair checkpoint regulation and prevent apoptosis of cells with defective DNA. Mutation of p53 is found in more than 50 % of cancers [115].

The immune system plays an important role in initial stages of cancer. The presence of $CD103^+$ $CD39^+$ tumor-infiltrating CD8 T cells (TIL) correlates with a higher survival rate in patients with head and neck squamous cell carcinoma and these immune cells can effectively kill cancer [116]. However, some cancers escape immune surveillance by the secretion of immune inhibiting cytokines that interfere with the PDL-1 or CTLA-4 immune checkpoints. In the case of human acute myeloid leukemia, the cancer cells up-regulate the expression of the soluble immunoglobulin and mucin-domain containing-3 (Tim-3) which inhibits T-cells secretion of IL-2 and thus prevents activation of immune cells [117].

Another mechanism found in cancers is the over-expression of telomerase, which provide the cancer cells with stem cell-like properties and the overexpression of telomerase reverse transcriptase (hTERT) is correlated with aggressiveness of breast cancer cell lines [118].

1.4.3. Cancer metastasis

Metastasis originated from the Greek word "methistanai", which means "to change". In the clinical context metastasis indicates the spread of the disease from a primary tumor to a secondary place of malignancy. The fundamentals of how cancer invade was developed by Stephen Paget under the concept of "seed and soil", which indicates that cancer in order to successfully establish in a different place must be encounter an appropriated terrain of establishment (reviewed in [119]). In general, metastasis can be divided into stages. First, the cancer cells colonize the extracellular matrix (EM). In the initial step, the cancer cells start loosening their connection with adjacent cells such as epithelial or stromal tissue. E-cadherin is an important protein that regulates cell adhesion. For example, carcinomas downregulate the gene CDH1 that codes E-cadherin, promoting the cancer cell motility [120]. The loss of cell adhesion triggers the activation of VEGFA and secondarily angiogenesis [121]. Next, cancer cells degrade the basement membrane by enzymatic activity. One of the most studied enzymes involve cancer progression are the metalloproteinases (MMPs). LASP1 is a focal adhesion protein involve in cell migration and cancer progression. LASP1 is involved in the regulation of the formation of the invadopodia. Down regulation of LASP1 and over-expression of MMPs can limited the invasion of cancer cells, especially in breast cancer [122]. Second, cell enter the vascular system and move to the new metastatic niche. After cancer cells have overcome the vascular endothelium barrier and entered the blood vessels, they must exit the blood and enter the metastatic niche. The tight junction protein 1 (ZO-1) is a 220 kDa peripheral membrane protein, which function as scaffold for other tight junction proteins. Zhou *et al.* demonstrated that cancer-secreted exosomes transport and release miR-105, which disrupts these tight junctions by targeting ZO-1, and thus enables escape of cancer seed cells from the blood vessel. In mouse models, breast cancer MCFDCIS cells overexpress miR-105 and exhibit higher metastasis rate compared with controls [123]. Another mechanism cancer uses to invade new tissues without utilizing the vascular system is called "transcoelomic" metastasis. This form of dissemination uses the peritoneal cavity to invade

other tissues. One cancer that spreads via the transcoelomic mechanism is ovarian cancer and its liver metastasis. This metastatic mechanism is mediated via tumor-associated macrophages (TAMs) that infiltrate the peritoneal cavity and serve as a scaffold to form ovarian cancer spheroids. On the other hand, apoptosis signal-regulating kinase 1 (ASK1) activity is required for macrophage activation and inflammation. The effect of ASK1 on TAMs was shown using a mouse model of ovarian cancer. ASK1 reduces the infiltration of TAMS and the progression of ovarian cancer [124].

Some types of cancer are disseminated through the lymphatic system. This is a particularly nasty, aggressive mechanism because the lymph nodes are interconnected via lymph ducts and ultimately back to the vascular system. The classical example of the lymphatic metastasis is seen in prostate cancer. Prostatic cancer metastasis is associated with TNF-α and the induction of chemokine receptor 7 (CCR7) by phosphorylation of the extracellular signal-regulated kinase (ERK). Additionally, Prostate cancer cell migration is regulated by the phosphorylation of p38 through the interaction between the chemokine (C-C motif) ligand 21 (CCL2) and CCR7 [125].

Cancer is the "emperor of all maladies", e.g., worldwide human disease and one of the most prevalent causes of mortality [107, 126]. The battle against this disease has challenged researchers to find new and more efficient ways of controlling it. Advances in the field of nanotechnology have enhanced the efficacy of the existing drugs by extending their bioactivity through novel formulation. For example, novel synthetic nanoparticles, such as liposomes, have been used as a drug delivery system against cancer [127, 128]. Nevertheless, these approaches have limitations such as bio-incompatibility [129], development of allergic reactions [130] and lack of target specificity [131, 132]. In contrast to synthetic nanoparticles, MSC exosomes are biocompatible and may accumulate within tumors after intravenous injection [133-135]. Recently, exosomes isolated from TRAIL-transduced MSCs were shown to induced apoptosis in cancer cell lines in a

dose-dependent manner [136]. These findings support the notion that MSCs exosomes might accumulate in tumors and have the potential to identify the site of metastases [14, 137].

Here, in a proof of concept study, the biodistribution of HUC-MSCs-derived exosomes in osteosarcoma is explored using two non-invasive tracking methodologies *in vivo*. Specifically, MSCs exosomes were labeled with gadolinium (Exo-GdL) for 14T magnetic resonance imaging (MRI) or with near infrared (NIR) fluorescent dyes for fluorescence imaging. Here, the biodistribution of MSC exosomes in osteosarcoma ectopic tumor-bearing mice was observed, to determine whether labeled exosomes accumulate in tumors at an enhanced rate compared to similarly labeled synthetic nanoparticles (liposomes). These data support the notion that MSC exosomes accumulate in osteosarcoma tumors and may have utility for metastasis detection.

2. Materials and Methods

2.1. Cell Culture Conditions

2.2. Human Umbilical Cord Mesenchymal Stromal Cells isolation

Human subjects committee reviewed our protocols and deemed our research as no involving human subjects. Human umbilical cord mesenchymal stromal cells (HUC-MSCs) were isolated following the protocols described by Smith et al. (2016). In brief, anonymous, discarded human umbilical cords were obtained from Via Christi Hospital, Manhattan, KS, following informed consent. The cords were stored in Povidone Iodine Prep solution (Dynarex Corp., Cat. #: 1416) until processing. All human biological materials were treated as potential biohazardous materials (using universal precautions) and processed under sterile condition following the biosafety regulations. Umbilical cords were rinsed with 1 % antibiotic-antimycotic (Gibco™, Cat. #: 15240062) in Dulbecco's phosphate buffered saline (DPBS, Gibco, Cat. #: 14190144) and then treated 5 minutes with 0.5% Povidone Iodine Prep /DPBS solution (Dynarex Corp., Cat. #: 1416). The cords were divided into multiple 1cm pieces and placed into gentleMACS™ C tubes (Milteny Biotec, Cat #: 130-096-334) for tissue disruption with a mixture of Collagenase Type I (300 U/ml) and Hyaluronidase (1mg/ml) in 3mM $CaCl_2$/DPBS, using an automatic tissue dissociator (GentleMACS™, 130-093-235). The mixture was incubated for 3ours at 37 ˚C. At the end of incubation time, the sample was passed through 100 µm filter (MACS® SmartStrainer, Cat. #: 130-098-463). The collected suspension was centrifuge 5 minutes at 200 g at room temperature and the pellet was resuspended in 500µl of red blood cell lysing buffer) Hybri-Max™, (Sigma-Aldrich, Cat. #: R7775-100). The cell suspension was diluted in 8ml of DPBS and further centrifuged under

the same conditions to collect cell pellets. The cell pellet was resuspended in 1ml Dulbecco's Modified Eagle Medium low glucose (DMEM) supplemented with 10 % pooled Human Platelets Lysate (pHPL). The cell concentration and viability were determined using the acridine orange/propidium iodide (AO/PI) (Nexcelom Bioscience, Cat. #: CS2-0106) assay, with an automated cell counter (Nexcelom Bioscience, Cellometer® 2000). The cells were seeded at 1×10^4 cells/cm^2 and incubated in DMEM containing 10 % pHPL at 37 °C, 90 % humidity and 5 % CO_2.

2.3. HUC-MSCs Characterization

The characterization of the cell lines HUC-255 and HUC-257 were previously described by Smith et al. (2016). In the present work, the cell line HUC-293 was characterized by the cell differentiation assay (adipogenic, chondrogenic and osteogenic) and flow cytometry.

2.3.1. Differentiation assay

The differentiation assay was carried out with the StemPro® kits (Thermo Fisher Scientific, Inc. Cat. #: A10070-01, A10071-01, and A10072-01) following the manufacturer recommendations. In brief, cells were seeded at 1×10^4 cell/cm^2 in 12-well plate (CytoOne, Cat. #: CC7682-7512). After 4 days of incubation, cell media were changed with corresponding differentiation media and incubated for additional 4 days. Differentiation was observed to take place over 14-21 days. Thereafter, the media was removed and the cells were fixed with 4% paraformaldehyde in phosphate buffer (pH = 7.4) for 10 mins at room temperature. After fixation, adipogenic, chondrogenic and osteogenic assays were carried out independently by adding 0.3 % Oil Red solution (500ml), 0.1 % Safranin O solution (500 ml) and 2 % Alizarin Red S solution (500 ml),

respectively. The images of the assay were captured with the EVOS FL cell imaging system (Thermo Fisher Scientific, Inc.)

2.3.2. Flow cytometry

The isolated cells were characterized by flow cytometry with the BD Stemflow™ assay kit Cat. #: 562245), following the manufacturer recommendations. In brief, 1×10^4 cell/cm^2 were seeded in T-25 flasks in DMEM 10 % pHPL at 37 °C, 90 % humidity and 5% CO_2 until the cells reached 80% of confluence. The cells were trypsinized and collected by centrifugation at 1000 g, then the cell viability and concentration was determined by AO/PI staining. The cells were stained with the appropriate antibodies and analyzed in a flow cytometer LSR Fortessa X20 (BD-Bioscience). Before running the samples, the machine was calibrated with the Fluorescence Minus One controls (FMOs) for CD90, CD44, CD105 and CD73. Additionally, isotopes control cocktails were utilized. The hMSC positive isotope control cocktail containing mIgG1, κ FITC (Clone: X40), mIgG1, κ PerCP-Cy5.5 (Clone: X40) and mIgG1, κ APC (Clone: X40). The negative isotype control cocktail containing mIgG1, κ PE (Clone: X40), mIgG2a, κ PE (Clone:G155-178) and CD90 FITC (Clone: 5E10) was utilized. AS compensation controls. As compensation controls were immplemented: unstained hMSCs, FITC Mouse Anti-human CD90 (Clone: 5E10), PE Mouse Anti-Human CD44 (Clone: G44-26), PerCP-Cy™5.5 Mouse Anti-Human CD105 (Clone: 266) and APC Mouse Anti-Human CD73 (Clone:AD2).

2.4. Cancer Cell Lines

The cancer cell lines were obtained from the collection of Dr. Deryl Troyer (Department of Anatomy and Physiology, Kansas State University). 143B (ATCC® CRL8303™) human

osteosarcoma, A-375 [A375] (ATCC® CRL1619™) human malignant melanoma, A549 (ATCC® CCL185™) human lung carcinoma, PC-3 (ATCC® CRL1435™) human prostate grade IV adencarcinoma, MDA-MB-231 (ATCC® CRM HTB26™) human mammary gland adencarcinoma and K7M2 mouse osteosarcoma, were seeded at a standard density of 1×10^4 cells/cm^2 and maintained until 80 % confluency in DMEM 10 % HPL-depleted exosomes (dpHPL). Cells were incubated at 37 °C, 90% humidity and 5% CO_2.

2.5. Cell Passaging

All the cell lines HUC-MSCs and cancer cell lines were maintained in their respective cell culture media otherwise indicated. All the cell lines were passed following the protocol stablished in Weiss laboratory.

In brief, when the cells reached 80 % confluency the media was removed and the cells were washed twice in calcium and magnesium free DPBS. After that, 0.05 %Trypsin-EDTA solution was added to the HUC-MSCs monolayer and then incubated at 37 °C for 3-5 minutes. For cancer cells the trypsinization was carried out with 0.25 % Trypsin/EDTA solution. When the cells unattached, the reaction was stopped by adding 3 volumes of DMEM 10 % dpHPL. Cells were collected by centrifugation at 200 g for 5 minutes at room temperature. Cell concentration and viability were determined as described in section 1.1.

2.6. Pooled Human Platelet Lysate Depleted Exosomes (dpHPL)

HPL depleted of exosomes (dpHPL) was prepared from pooled human platelet lysate following the in-house method described in [138]. To prepare the dpHPL, units of frozen expired human platelets material was obtained from the blood center. The samples were stored at -20 ˚C until

processing. Each batch was prepared from approximately 25 donors that were subjected to two rounds of freezing-thawing at -80 °C /22 °C cycles to break the platelets and release the growth factors. Next, debris was eliminated by centrifugation at 4000 g for 15 minutes at 4 °C. pHPL was aliquoted in 50 ml conical tubes and stored at -20 °C. To deplete exosomes from the pHPL, the samples were centrifuged at 4000 *g* for 30 minutes at 4 °C, filtered (0.22µm) and centrifuged for 10 hours at 120,000 *g* at 4 °C (Beckman Counter, Inc., L-90K) using a SW-41-Ti Swinging-bucket rotor. After the ultracentrifugation step, the dpHPL and the exosomes pellet were collected, aliquoted, and stored at -20 °C.

2.7. Exosomes Isolation by Sequential Ultracentrifugation

Exosomes were isolated from the cell-conditioned medium (CM) by sequential ultracentrifugation using a modified protocol proposed by Momen-Heravi [139]. The CM was collected when the cells reached 80 % of confluence, usually after 2 days of exposure to the cells. Before the media was processed, cell viability was determined by AO/PI assay as was previously described. In order to reduce the possible contamination with other extracellular vesicles (apoptotic bodies), the threshold of cell viability to isolate the exosomes from the CM was set at 95 %; below this point the media was discarded [140]. After collection, the CM was centrifuged for 30 min at 3184 *g* in a benchtop centrifuge (Eppendorf, 5810R) using a swing bucket rotor A-4-62 (Eppendorf, Cat. #: FL08517291) to eliminate cell debris. The CM was filtered (0.22 µm) and transferred to 13-.2ml Ultra-clear tubes (Beckman Counter, Cat. #: 344059). In order to eliminate larger extracellular vesicles, the CM was centrifuged 30 minutes at 20,000 *g* (Beckman Counter, Inc., L-90K) with a

SW-41-Ti swinging-bucket rotor at 4 ˚C. The pellet of this step (S1) was collected and stored at -80 ˚C. Then the CM was transferred into a fresh ultracentrifuge tube and centrifuge at 4 ˚C, 90 minutes at 120,000 *g* (S2). The CM was then discarded and the pellet was resuspended by 30 seconds vortex in 500 µl of DMEM and stored at -80 ˚C for further analysis.

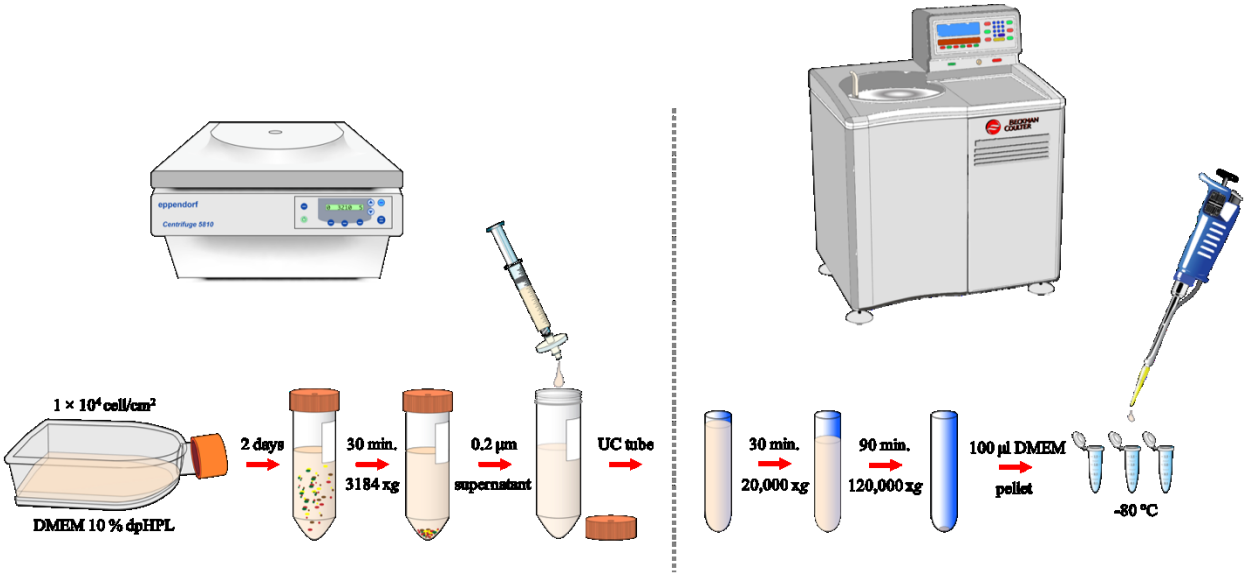

Figure 3. Schematic representation of the exosomes isolation process. Cells were incubated in standard conditions until they reach 80 % confluence, The cells viability was determined by acridine orange, propidium iodide staining (AO/PI), in an automatic cell counter. If the cells had a viability equal or higher of 95 % we continue the process, otherwise the media was discarded The cell debris of the conditioned media obtained from the MSCs cell culture, was removed by centrifugation at 3184 *g* during 30 minutes. The pellet was discarded and the media was filtrated with 0.2 µm filters. After that the conditioned media was transferred to an ultracentrifuge tube and centrifuge at 20,000 *g* during 30 minutes. Then we collected the media and a second round of

centrifugation at 120,000 *g* during 90 minutes was performed. Finally, the obtained pelled was diluted in 100 µl of DMEM, aliquoted and stored at -80 °C for further use.

2.8. Synthesis of Gadolinium Lipid (GdL)

The synthesis of Gadolinium ion chelated DSPE-DOTA was performed using two-step preparation method as previously described with some modifications [141-143]. In brief, 75 mg of DSPE was first dissolved in 10 ml chloroform containing 2 % (v/v) triethylamine (TEA). After that, 86 mg DOTA-NHS ester was added and stirred vigorously until all reagents were completely dissolved. The reaction was allowed to take place for another 3 hours at 40 ºC. At the end of incubation time, the obtained clear reaction mixture was concentrated and dried under vacuum to recover the white powder. To purify the conjugating DSPE-DOTA lipid, 6 ml of deionized water was used to disperse reaction crude, the suspension underwent 5 cycles of freezing and thawing in liquid nitrogen and 60 ºC water bath, respectively and then centrifuged at 4500 *g* for 10 minutes. The resulted DSPE-DOTA suspension was filtered through 0.2 µm membrane to remove insoluble by-product and lyophilized to get dry powder.

To prepare DSPE-DOTA-Gd (Gd-Lipid), 50 mg DSPE-DOTA (0.05 mmole) was hydrated in 10 ml of acetate buffer (pH = 5.5) and further treated with 0.5 mmole of $Gd(OAc)_3$ 50 ºC for 12 hours. After incubation, the Gd-DOTA-DSPE was purified by centrifugation at 4500 g for 10 minutes. The obtained white product was washed 3 times with acetate buffer (pH 5.5) and 3 times with water to remove all non-chelated Gd^{3+} ion. The samples were lyophilized to obtain a dry powder.

2.9. Labeling of exosomes with Gadolinium Lipid (exo-GdL)

Gadolinium labeled exosome was prepared by lipid insertion following membrane extrusion method [142, 144]. In brief, different amount of DSPE-DOTA-Gd (500, 1000, and 2000 μg) were solubilize in 1× DPBS at 65 °C to obtain clear solution. The lipid (Gd-L) suspension was cooled down to room temperature and co-incubated with 1 mg exosome protein for 30 minutes. The protein concentration was determined by BCA assay (G-Biosciences). The exosome and Gd-L mixture was bath sonicated for 2 minute and probe sonicated for 3 minutes with amplitude at 30 %, 30 seconds pulse on, and 30 seconds pulse off. The mixture was extruded trough 100 nm membrane pore size to unify the hydrodynamic size. Finally, Exo-Gd were purified with an Amicon Ultra-4 centrifugal filter (Millipore, MA) with a molecular weight cut-off of 3 kDa and stored at 4 ºC for further use. Rhodamine dye-labeled exosome were also prepared in the same fashion by hydrating 20 μg of L-α-Phosphatidylethanolamine-N-(lissamine rhodamine B sulfonyl) (Ammonium Salt) (Egg Liss Rhod PE) film with 1 mg exosome protein before performing insertion process.

2.10. Exosomes Characterization

2.10.1. Physicochemical Characterization

2.10.2. Dynamic Light Scattering and Z-potential

The size and size distribution of exosomes was determined by dynamic light scattering (DLS) and the zeta potential (ζ-potential) was measured to analyze the integrity and stability of exosomes. To perform the measurements, the exosomes samples were diluted 1:100 in 0.2μm-filtered double distilled water (ddH_2O). 200 μl of each sample was loaded into folded capillary cell DTS1070 (Malvern Instruments, Ltd.) to measure Z-potential and disposable polystyrene cuvettes (Malvern

Instruments, Ltd., Cat. #: ZEN0040) to measure DLS. Both measurements were performed with a Zetasizer Nano ZS (Malvern Instruments, Ltd.). The instrument was programed to perform 11 runs of 10 seconds with 5 repetitions.

2.10.3. Nanoparticle tracking Analysis

The population size of the exosomes and their concentration were determined Nanoparticle Tracking Analysis (NTA) using a NanoSight LM-10 (Malvern Instruments, Ltd.). The samples were diluted between 10 to 1×10^4 times in 0.2 μm-filtered DPBS. Each measurement was performed at constant temperature (25 ˚C ± 1) to ensure the same viscosity of the fluid. The NanoSight software (NTA 3.2) was programed to capture 60 seconds videos and 5 repetitions per sample.

2.10.4. Transmission Electron Microscopy

For transmission electron microscopy (TEM) analyses, the exosomes suspension was probe sonicated 3 minutes with (name the instrument, and power level used) and amplitude of 30 % and 30 seconds pulse cycles to disrupted exosomes aggregates. The exosomes were diluted 1:100 in 0.2 μm-filtered DPBS. The. 10μl of the exosomes dilution were mixed 1:1 ratio with saturated uranyl acetate (Electron Microscopy Science) for negative contrast and 10μl of the mixture were placed on a Formvar-coated 200 mesh copper grid (Electron Microscopy Science, Cat. #: 215-412-8400). The solvent was allowed to evaporate from the grid at room temperature. The images of the exosomes were captured with a Tecnai™ G^2 Spirit BioTWIN (FEI™ Company, USA) TEM at 6.8×10^3 magnification and 80 kV accelerating voltage

2.11. Protein Characterization

2.11.1. Protein Quantification

Protein concentration of exosomes and cell lysate samples were routinely measured using bicinchoninic acid assay (BCA) (G-Bioscience, Cat. #: 786571) following the manufacturer's recommendations. In brief, serial dilutions of bovine serum albumen fraction V (BSA) standards (2mg/ml to 15.62µg/ml) and exosome protein (10 to 100 times dilution) were prepared in DPBS (Gibco, Cat. #: 14190144). The BCA solution and the cooper solution were mixed in 50:1 ratio respectively. Then 200µl of the solution was transferred to 96-wells plates. 25µl of the exosome sample or the standards were added to each well and the solution was mixed by pipetting thoroughly. The plates were incubated for 30 minutes at 37C. After the incubation the absorbance was recorded at 562nm with a SpectraMax®i3 microplate reader (Molecular Devises). The blank is subtracted from the measurements and a standard curve is prepared by plotting the average corrected measurement for each BSA standard vs absorbance. The plate reader has a built in curve fitting algorithm and the best fit curve was used to determine the concentration of the unknown replicates.

2.11.2. Whole Cell lysate preparation

To obtain the cell lysate, cells were trypsinized as was previously described in section 1.4. 1×10^6 cells were resuspended in 100 µl lysis buffer (Thermo Fisher Scientific, Inc. Pierce® RIPA Buffer, Cat. #: 89900) supplemented with 1% (v/v) phosphatase inhibitor (Thermo Fisher Scientific Inc. Cat. #: 1862495) and 1% (V/V) protease inhibitor (Thermo Fisher Scientific, Inc. Cat. #: 1862209). The cell suspension was incubated at room temperature for 15 minutes. Then, the cell debris were removed by centrifugation for 10 minutes at 17933 g at 4 ˚C in a top bench centrifuge (Eppendorf,

Cat. #: 5424R) with a fix angle rotor (Eppendorf, Cat. #: FA-45-24-11) and the supernatant was transfer into a fresh 1.5 ml tube to measure the protein concentration.

2.11.3. Exosomes Lysis

The exosomes aliquots were taken from the -80 ˚C and thawed on ice. The exosome protein was mixed with 4 × LDS Sample Buffer (Thermo Fisher Scientific, Inc. Cat. #: NP0007) in 3:1 ratio respectively. The sample was thoroughly mixed by pipetting and incubated for 10 minutes at 70 ˚C. The protein concentration was determined by BCA assay (see section 6.3.1).

2.11.4. Western Blot

2.11.4.1. SDS-Page

The protein electrophoresis was carried out on a XCell SureLock™ Mini-Cell Electrophoresis System (Thermo Fisher Scientific, Inc, Cat #: EI0001), using 4-12 % Tris-Glycine polyacrylamide gels (PAGE, Thermo Scientific, Inc. Novex™, Cat. #: 10XP04125BOX). The system was filled up with 1× sodium dodecyl sulfate (SDS)-PAGE running buffer (25 mM Tris, 192 mM Glycine, 1 % SDS). 20 µg of each sample was loaded per well. As reference, 8 µl of a pre-stained protein standard (Thermo Fisher Scientific, Inc. Novex®, Cat. #: LC5800) was loaded into the gel. The electrophoresis was performed at 85V for about 2 hours. After the electrophoresis, the gel was stained overnight with Coomassie blue buffer (40 % ddH_2O, 10 % acetic acid, 50 % methanol, 0.1 % Coomassie blue). The gel was rinsed 3ours in destaining solution (40 % ddH_2O, 10 % acetic acid, 50 % methanol) until the protein bands were clear. The SDS-PAGE image was captured with a Gel Doc™ XR+ imaging system (Bio-Rad, Inc.)

2.11.4.2. Protein Transfer

Protein were transferred from the gel to a Polyvinylidene fluoride (PVDF) membrane (Merck Millipore Ltd., Immobilon®-P, Cat. #: IPVH00010) using a semi-dry electrophoretic transfer system (Bio-Rad. Trans-Blot® SD, Cat. #: 170-3940). The PVDF membrane was activated 15 seconds in methanol and then rehydrated 2 minutes with ddH_2O. Before the transferring process, the PVDF membrane, filter papers, and the gel were maintained in transfer buffer for 5 minutes. The transferring buffer was prepared by supplementing the 1× running buffer with 20 % methanol. Transfer was carried out for 40 minutes at 10 V. To determine the protein transferring, the membrane was stained with Ponceau S solution (Sigma, Cat. #: P7170). The membrane was rinsed with 1× washing solution (2.4g Tris-Base, 8 g NaCl, 1 ml Tween 20, ddH_2O up to 1000 ml) until the excess of stain has been removed.

2.11.4.3. Immuno Blotting

The membrane was blocked 1 hour in blocking buffer (1× washing solution, 5 % non-fat dry milk. Bio-Rad, Cat. #: 170-6404). The antibodies were diluted 1:200 in blocking buffer following the recommendation of the manufacturer. All the antibodies were purchased to Santa Cruz Biotechnology, Inc. The primary antibodies used to characterize exosomes were: CD9 (C-4, Cat. #: sc-13118), CD63 (MX-49.129.5, Cat. #: sc-5275), CD81 (5A6, Cat. #: sc-23962), HSP70 (3A3, Cat. #: sc-32239) and Na^+/K^+-ATPase β3 (46, Cat. #: sc-135998). The membranes were incubated with the primary antibodies overnight at 4 ˚C in a rocking shaker. After the incubation time, the membranes were washed 3 times in washing buffer for 15, 5 and 5 minutes, each. The secondary antibody m-IgGκ BP-HRP (Cat. #: sc-516102) was diluted in blocking buffer in a 1:1000 ratio and

the membrane was incubated 1 hour. After the incubation period the membrane was washed 3 times as previously described. The antibodies were detected by chemiluminescence reaction using the SuperSignal® West Femto substrate (Thermo Fisher Scientific, Inc., Cat. #: 34094) following the manufacturer's recommendations. The images were captured using a Kodak Image Station 4000.

2.11.4.4. Dot Blots

Samples of whole cell lysates or exosomes were prepared as described in sections 5.3.2 and 5.3.3, samples were diluted in DPBS to get final concentration of 1000 µg/ml. 2 µl of each sample were spotted in triplicates onto a PVDF membrane, the samples were incubated at room temperature until were completely absorbed by the membrane. Then the membrane was stained with Ponceau S solution to determine if the protein was bound to the membrane, followed by overnight incubation in blocking buffer. The immuno blotting and detection was carried out as was described in section 5.3.4.3

2.12. Analysis of GdL-labelling exosomes (Exo-GdL)

2.12.1. GdL-labelling efficiency

The amount of Gd^{3+} labelling onto exosome was determined using inductively coupled plasma mass spectrometry (ICP-MS, PerkinElmer, NEXion 350X). For ICP-MS, the Exo-GdL with different protein to Gd lipid by weight ratio (2:1, 1:1, and 1:2) samples were digested with 2.0 ml of concentrated HNO_3 for 5 hours. After chemical digestion, 100 µl of the sample was diluted with 10 ml of 2 % HNO_3 and analyzed using ICP-MS.

2.12.2. Gadolinium ion release assay

The cumulative gadolinium release from the Exo-GdL was assessed under physiological condition at 37 °C at pH: 7.4. In brief, 1ml of Exo-GdL [1mg/mL] were placed in a dialysis bag membrane (Mw. Cutoff = 500 Da) and dialyzed against 250 ml of PBS (pH = 7.4). At constant stirring (100 rpm), 200 µl of sample was taken at predetermined time intervals. The amount of released Gd was quantified by ICP-MS. As control experiment, 1 mg/ml of Magnevist® was placed in a dialysis bag and processed under the same condition.

2.12.3. Magnetic Properties of Exo-GdL

The magnetic resonance (MR) imaging were acquired on a Bruker 600 MHz Avance III with microimaging capability. The longitudinal relaxation time of Exo-GdL in an aqueous solution at different Gd^{3+} concentration (0.03, 0.06, 0.14, and 0.28 mM) were obtained using a QTR 30 mm coil at 22 °C with a RARE (Rapid Acquisition with Relaxation Enhancement) pulse sequence with variable repetition time. Scans were performed with the following imaging parameters: repetition time (TR) = 8000, 6000, 5000, 3000, 1500, 900, 700, 500, 300, 100 and 50 ms, echo time (TE) = 10.18 ms, slice thickness = 1 mm, flip angle (FA) = 80°, image size 256 × 256, field of view (FOV) = 30 × 30, total acquisition time of 55 minutes 43 seconds. The representative T1 weighted magnetic resonance phantom images of Exo-GdL were taken at TR = 3000 ms, TE = 10.18 ms, and slice thickness = 1 mm. The longitudinal coefficient relaxivity value r_1 was determined from the slope of the plot of $1/T_1$ versus the sample concentration. The magnetic property of Magnevist® solution with the same Gd^{3+} concentration was conducted under the same experimental condition.

2.13.*In-vitro* assays

2.13.1. 3-(4,5-dimethylthiazol-2-yl)-2,5-diphenyltetrazolium bromide (MTT) cell metabolic assay (proliferation assay)

Cells were seeded in 96 wells plates (CytoOne, Cat. #: CC7682-7596) at a cell concentration of 1 × 10^4 cell/cm^2 per well in 150 µl of phenol free DMEM (Gibco, Cat. #: 11054020) supplemented with 10 % HPL-depleted of exosomes. Cells for the standard curve were seeded in triplicate at densities between 200 to 2 × 10^4 cells/cm^2. The plates were incubated for 24 hours at 37 °C, 90% humidity and 5% CO_2 (NuAire Autoflo, Cat. # NU-4950). After 24 hours of incubation, 10 µl of the different concentrations of exosomes or controls were added to each well. After an additional 24 hours of incubation, 10 µl of 5 µg/ml MTT (3-(4,5-Dimethylthiazol-2-yl)-2,5-Diphenyltetrazolium Bromide) (Thermo Fisher Scientific Inc, Cat. #: M6494) solution in DPBS were added to each plate. The reaction was incubated for additional 4 hours and then the reaction was stopped by adding 100 µl of 10 % SDS solution in 0.01 M HCl. After 16 hours ours, the absorbance was read at 570 nm with a SpectraMax®i3 microplate reader (Molecular Devices).

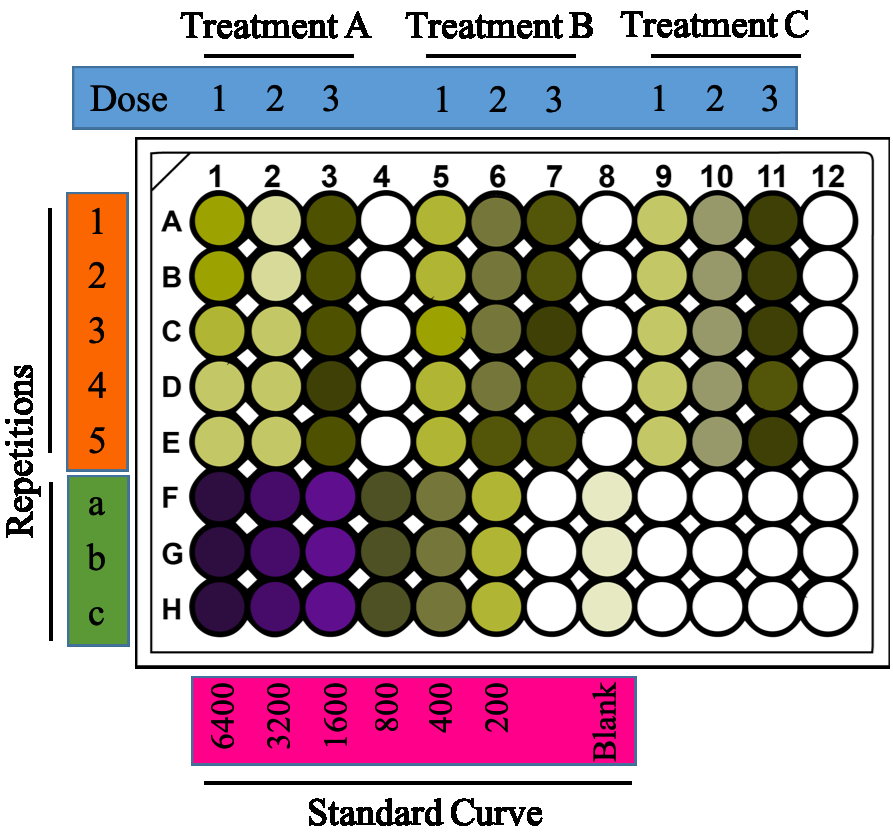

Figure 4. Schematic representation of the MTT assay design. Cells were seeded at 1×10^4 cells per well. after 24 hours of incubation, the treatments of exosomes or controls were added to each columns by concentration. Five technical repetitions (rows A-E) were used for each treatment. A standard curve covering cell concentrations from 6400 to 200 cells were seeded in triplicates (rows F-H). Blank wells were included in the plate to correct the optical density (column 8, F-H).

2.13.2. Cellular Uptake of Exosomes

Mouse K7M2 osteosarcoma cells were seeded to a cell concentration of 1×10^4 cells/cm^2 in 300 µl of DMEM (Gibco, Cat. #: 11054020) supplemented with 10 % pHPL-depleted exosomes per well, in an 8-Well Chambered Cover Glass (Cellvis, Cat. #: C8-1.5-H-N). Cells were incubated for 24 hours at 37 °C, 90 % humidity and 5 % CO_2. the cells were treated with 25 µg of rhodamine B

labeled nanoparticles as positive control (RhB-control), or RhB-labeled exosomes (Exo-RhB) suspended in 10 µl of DPBS, or 10 µl DPBS alone (negative control). The cell culture was incubated for additional 24 hours and then the media was removed and the cell were fixed with 4 % paraformaldehyde buffered with 10 mM phosphate buffer (pH = 7.4) (Sigma-Aldrich, Cat. #: P6148-500) and 0.1 % Glutaraldehyde (Fisher Scientific, Cat. #: 111-30-8) prepared in ddH_2O. After the fixation, the wells were rinsed with DPBS. To stain the cellular nuclei, 100 µl of 10 µg/ml 4',6-diamidino-2-phenylindole (DAPI) (Sigma-Aldrich, Cat. #: D9542-5) solution was added to each well and incubated for 10 minutes in the dark at room temperature. After staining, DAPI was removed by rinsing the cell monolayer with DPBS. To prevent cell from dehydration, 100 µl of Fluoromount™Aqueous Mounting Medium (Sigma-Aldrich, Cat. #: F4680-25) were added to each well before performing the confocal laser scanning microscopy (CLSM) (Carl Zeiss, LSM-700). Images were analyzed with the modular image-processing, analysis software ZEN 2, blue edition (Zeiss) and ImageJ. The cellular uptake was further confirmed by flow cytometry. For flow cytometry, K7M2 cells were treated with Exo-RhB or unlabeled exosomes for 6, 12, 24 and 48 hours ours. The accumulation of exosomes in the cells was determined by the fluorescence emission of RhB. 1×10^4 events were captured using a flow cytometer (LSR Fortessa X20, BD Bioscience).

2.13.3. Apoptosis Assay

K7M2 cells apoptosis was evaluated using the FITC Annexin-V Apoptosis Detection Kit I (BD Pharmingen™), following the manufacturer's instructions. Briefly, K7M2 cells were seeded in T-25 flasks at a cell density of 1×10^4 cells/cm^2. Cells were incubated for 24 hours under standard conditions. At the end of the incubation time, cell cultures were treated with naive exosomes

(94ng/cm^2) or Exo-GdL (94 ng/cm^2, 940 ng/cm^2 or 9400 ng/cm^2) and incubated an additional 24 h. Trea™ent with 500 µM H_2O_2 was used as positive control. After that, cells were collected and rinsed 3 timed in the 1× binding buffer and subsequently stained with FITC-conjugated Annexin-V (Annexin V-FITC) and propidium iodide (PI). The cells were analyzed by flow cytometry using a LSR Fortessa X20 (BD Bioscience) equipped with the FACSDiva v8.0 acquisition software.

2.13.4. HUC-MSC stimulation assay

Cell were seeded at a cell concentration of 1 × 10^4 cell/cm^2 in T-75 flasks CellBIND® (Corning®, Cat. #: CLS3290) in DMEM supplemented with 10 % dpHPL at 37 °C, 90 % humidity and 5% CO_2 until the cells reached 80 % of confluence. After 24 hours of incubation, the cells were treated with 1 µg/ml of polynosinic-polycytidic acid (Poly (I:C) (Sigma-Aldridge®, Cat. #: P9582-5MG) or 10 ng/ml of lipopolysaccharides of *Escherichia coli* (LPS) (Sigma-Aldridge®, Cat. #: L31129-25MG) or 10 ng/ml of recombinant human IFN−γ (FN−γ) (ThermoFisher Scientific, Cat. #: PHC4031) and incubated under the same conditions for additional 24 hours. The media with the stimuli was retrieved and changed with fresh DMEM 10 % dpHPL-free of stimulants. After additional 24 hours, the CM was collected for exosomes extraction. The treated cells were also collected following standard protocol. The cells were aliquoted at concentration of 2 × 10^6 cell in 500 µl of RNA*later*™ Stabilization Solution (ThermoFisher Scientific, Cat. #: AM7021) and stored at -80 °C until RNA extraction was conducted.

2.13.4.1. HUC-MSCs RNA extraction

The RNA extraction was performed with the RNeasy Mini Kit (Qiagen, Cat. #: 74106) following the instructions of the manufacturer. In brief, the vials with cells were taken from the -80 °C and centrifuged 5 minutes at 300 *g* at 4 °C to eliminate the RNAlater. The cell pellet was disrupted with 350 µl of lysis buffer. The cell lysate was diluted in 350 µl of 70 % ethanol. The mix was transfer to a RNeasy spin column and centrifuge for 15 seconds at 8000 *g*. The membrane was rinsed twice with 700 µl of washing solution and centrifuged for 15 seconds at 8000 *g*. The RNA was eluted from the membrane with 50 µl RNase-free water and centrifuged for 1 minute at 8000 *g*. The RNA was quantified with a spectrophotometer NanoDrop™ 2000 (ThermoFisher Scientific), aliquoted and stored at -80 °C until further experiments.

2.13.4.2. Synthesis of HUC-MSC complementary DNA (cDNA)

The HUC-MSC complementary DNA (cDNA) was synthesized with the SuperScript™ IV First-Strand Synthesis System (ThermoFisher Scientific, Cat. #: 18091200) following the instruction of the manufacturer. In brief, The primers were annealed in a cocktail containing 50 µM Oligo $d(T)_{20}$ primer mixed with 2 µg of HUC-MSCs RNA and diethyl pyrocarbonate (DEPC) treated water. The mix was incubated at 65 °C for 5 minutes, and then placed on ice for 1 minute. The retronscription (RT) mix was prepared in a separated tube containing: 4 µl of 5 × SSIV buffer, 1 µl of DTT (100 mM), 1 µl of ribonuclease inhibitor and 1 µl SuperScript™ IV Reverse Transcriptase (200 U/µl) per sample. The reaction was carried out by incubation at 50 °C for 10 minutes and then inhibited at 80 °C for 10 minutes. Finally the RNA was eliminated with 1 µl *E. coli* RNase-H at 37 °C for 20 minutes. The cDNA was aliquoted and stored at -80 °C. The components and concentration of the cocktail are summarized in table 1.

Table 1. Components and concentrations for the Reverse transcription (RT) reaction.

Reactive	[Initial]	[Final]	Volume 1X (µl)	Volume X (µl)
Samples amount				**10**
DEPC-Water (µl)			12.40	124.00
SSIV Buffer [5✕]	5	1	4.00	40.00
dNTPs [mM]	10	0.2	0.40	4.00
Oligo d(T)$_{20}$ [50 µM]	50	2.5	1.00	10.00
Ribonuclease Inhibitor (U)	40	0.4	0.20	2.00
DTT [mM]	100	5	1.00	10.00
SuperScript IV (U)	200	10	1.00	10.00
Subtotal			18.00	180.00
DNA [µl]			2	
Total			20.00	

2.13.4.3. Endpoint polymerase chain reaction (PCR)

The genetic expression of stimulated cells was first evaluated by endpoint polymerase chain reaction (PCR) with the Phusion High-Fidelity PCR Master Mix (ThermoFisher Scientific, Cat. #: F531L). The primers utilized here were designed with the online software of the National Center for Biotechnology Information (NCBI). First, the quality of the cDNA was evaluated with the

primers, sense HUPBGD-1F 5'-TCG CCT CCC TCT AGT CTC TG-3', HUPBGD-1R anticance HUPBGD-1R 5'-TAC TGA GGA GGC AAG GCA GT-3' (1166 bp). The genetic expression of stimulated cells was evaluated using the following primers: The concentrations and components for this PCR are summarized in table 2.

Table 2. Components and concentrations for HUC-MSC RT-PCR.

Reactive	[Initial]	[Final]	Volume 1X (µl)	Volume X (µl)
Samples amount				**10**
Water			32.72	104.70
10X Long PCR Buffer [X]	10	2	12.40	39.68
dNTPs [mM]	2.5	0.3	7.44	23.81
F [µM]	10	0.5	3.10	9.92
R [µM]	10	0.5	3.10	9.92
Super Taq [u/µl]	5	0.1	1.24	3.97
Subtotal			60.00	192.00
DNA [µl]			2	
Total			62.00	
Total			20.00	

To evaluate the genes TLR3, TLR4, CXCL9 and TRAIL, the endpoint PCR was conducted under the same conditions as mentioned above. The primers utilized for the toll like regents receptor genes were: TLR3 sense TLR3-2F 5'-AAG GCT AGC AGT CAT CCA ACA-3', antisense TLR3-2R 5'-GCA CAA TTC TGG CTC CAG TT-3' (311 bp); TLR4 sense HTLR4-4F 5'-CGC TTT CAC TTC CTC TCA CC-3', antisense HTLR4-4R 5'-TCC CAG CTT TCT GGT CT CAC-3' (258 bb). The chemokine CXCL9 gene was evaluated with the primers, sense HCXCL9-1F 5'-CTTT CCT GGC TAC TCC ATG-3', antisense HCXCL9-1R 5'-GTT GGT CAC TGG CTG ATC TAT AA-3' (257 bp). One of the members of the tumor necrosis factor superfamily (TNF) TRAIL gene was evaluated with the primers, sense TRAIL-4F 5'-GCC TGG CTG ACT TAC AGC A-3', antisense TRAIL-4R5'-ACG GAG TTG CCA CTT GAC TT-3'.(293 bp). The annealing temperature for the genes TLR4 and CXCL9 was 53 °C. The annealing temperature for TLR3 was 54 °C, and for TRAIL was 55 °C. The thermocycler conditions are summarized in table 3.

Table 3. General thermocycler conditions for PCR

Process	Temperature (C°)	Time (min)	Cycles
	98	0.5	
Denaturation	98	0.25	
Annealing	54	0.5	35
Extension	72	1	
Final Extension	72	10	
Finish	Forever	4	

2.13.4.4. Reverse transcription polymerase chain reaction (RT-PCR)

To evaluate the genes TLR3, TLR4, CXCL9 and TRAIL, the reverse transcription polymerase chain reaction (RT-PCR) was conducted with the RT^2 SYBR® Green qPCR Mastermixes (Qiagen, Cat. #: 330500). The cycling conditions for cDNA evaluation were: initial denaturation at 95 °C for 15 minutes, follow by 45 cycles of 95°C for 15 seconds, 54 °C for 15 seconds and 60 °C for 30 seconds (data collection). The primers utilized for the toll like regents receptor genes were: TLR3 sense TLR3-5F 5'-AGC CTT CAA CGA CTG ATG CT-3', TLR3-5R: 5'-TTT CCA GAG CCG TGC TAA GT-3' (201 bp). TLR4 sense HTLR4-5F 5'- AAC TCT GGA TGG GGT TTC CT -3', (311BP) antisense HTLR4-5R 5'- AAC TCT GGA TGG GGT TTC CT-3' (201 bp). The chemokine CXCL9 gene was evaluated with the primers, sense HCXCL9-2F 5'- ACC AAC CAA

GGG ACT ATC CA -3', antisense HCXCL9-2R 5'- TTT GGC TGA CCT GTT TCT CC -3' (181 bp) and the TNF superfamily gene TRAIL was evaluated with sense TRAIL-5F 5'-AGC CTT CAA CGA CTG ATG CT-3', antisense TRAIL-5R 5'- TTT CCA GAG CCG TGC TAA GT-3' (201 bp). The variations on gene expression between unstimulated and stimulated HUC-MSC were evaluated by semiquantitative RT-PCR The C_t values were normalized (ΔC_t) with the housekeeping genes Porphobilinogen deaminase (PGBD) HPGBD-4F 5'- AGC CGT GCA TAC AGC TAT GA-3', HPGBD-4R 5'-AGG ATG GTT TTG GCT CCT TT-3' (258 bp) and 5'-aminolevulinate synthase (ALAS 1) HALAS-1F 5'-CAA AAC TGC TAA GGC CAA GG-3', HALAS-1R 5'- CAT TTC CTG CAC ATC CTC CT-3' (208 bp).

2.13.*In vivo* assay

Following the approved animal protocol from the IACUC at KSU, in vivo studies were conducted using the laboratory mouse model (immunodeficient nu/nu mouse with tumor). To develop the subcutaneous mouse model, 1×10^6 mouse osteosarcoma cells suspended in 1 × PBS (100 µl) were injected subcutaneously at the lower flank of the mouse. After 10 days of cancer cells injection (tumor size approximately, 6mm), the biodistribution of Exo-GdL in major organs and its time dependent in-vivo MRI imaging were evaluated.

2.13.1. Bio-distribution

Biodistribution study was conducted in a tumor-bearing NU/NU mice model. For the study, the calculated amount of Exo-GdL with known concentration of Gd^{3+} (0.015 mmol/kg, measured by ICP-MS) was injected via lateral tail vein injection. After 24 hours post injection, mice were euthanized and the major organs (heart, liver, kidney, spleen, and tumor) were collected to

determine the accumulated Exo-GdL content by measuring the elemental Gd^{3+} concentration using ICP-MS. For ICP-MS experiment, the collected organs were digested in 30 % H_2O_2 and 70 % HNO_3 alternatively for three successive digestion to ensure complete tissue digestion. Digested content were dissolved in 2 % HNO_3, filtered through a 200 nm syringe filter, and subjected to ICP-MS analysis for Gd.

2.13.2. Bio-imaging

A pilot MRI studies were conducted in a mouse bearing subcutaneous osteosarcoma. In brief, Exo-GdL with Gd^{3+} equivalent to 0.015 mmol/kg was injected via the lateral tail vein. MR images were acquired before, 30 and 90 minutes after the contrast administration using the Bruker WB 600 MHz NMR-MRI (14.1 tesla). The images were obtained using a QTR 30 mm coil at 37 °C with a FLASH (Fast slow angle shot) prot°Col. The T_1 weighted imaging with fat suppression parameters were TE/TR = 1.6/600 ms, slice thickness = 0.5 mm, flip angle = 80°, image size 256 × 256, FOV = 30 × 30, total acquisition time of 5 min and 10 seconds. To further confirm the tumor homing property of MSC exosomes, fluorescent bioimaging and biodistribution of profile of fluorescent probe-labeled exosomes was investigated using six-week-old immunodeficient female NU/NU nude mice (n = 3). Briefly, 1 mg of HUC-MSC exosomes or PEGylated nanoparticles (PEGNP) were labeled with 10 µg of DiIC18(7) (1,1'-Di°Ctadecyl-3,3,3',3'-Tetramethylindotricarb°Cyanine Iodide (DiR) (Thermo Fisher Scientific, Inc.) to obtain Exo-DiR exosomes or PEGNP-DiR nanoparticles, respectively. Then 5 mg/kg DiR-labelled exosomes or PEGylated nanoparticles were administered via lateral tail vein injections (volume 100 µl). To non-invasively image the exosomes or control particles, mice were anesthetized (2-3 % isoflurane in 100 % oxygen) and

placed within a Pearl® Trilogy imaging system (LI-COR®). The 750 nm channel was used to excite DiR, and emission was observed at 800 nm. Fluorescent background images were acquired prior to exosome or particle administration. When imaging animals, a fluorescent phantom was included in the image for calibration of the fluorescent intensity. After 48 hours ours post-injection, animals were euthanized, and their liver, kidney, spleen, lung, heart and tumor were collected and imaged. The organs were weighed and imaged under the same imaging system to quantify the amount of DiR dye using the Image Studio™ Software.

2.14.Statistics

When the assumptions were met analysis of variance was used to evaluate main effects and interactions. Following finding significant main effects or interactions, post-h˚C pre-planned comparisons were made using Bonferroni test using SAS studio university edition. Significance was set at $p < 0.05$. In graphs, mean and standard deviations are presented. Graphics were prepared using Sigma Plot v12.5 and saved as EMF files. The graphic files were edited using ACD Canvas v15 and saved as Tif.

3. Results

3.1. Physicochemical characterization of exosomes.

Exosomes were isolated from CM by sequential ultracentrifugation using previously described methods [139]. This technique has some advantages compared to others because it is simple and inexpensive, and it separates exosomes from other microvesicles and soluble proteins. As shown in figure 1, the exosomes were characterized by dynamic light scattering (DLS), Nanoparticles Tracking Analysis (NTA), surface charge (Z-potential) and Transmission Electron Microscopy (TEM). To begin to estimate biological variation, exosomes obtained from two different cell lines were independently processed and compared. As shown in figure 1A, naive exosomes exhibit a hydrodynamic size of 171 nm ± 42 with a relatively large polydispersity index (PDI) of 0.43 ± 0.03. Similarly, in figure 1B, NTA revealed a mode diameter of 66 nm ± 2. Both DLS and NTA data showed a multimodal distribution, indicating heterogeneity in the size of the particles, which is in accordance with previous publications [145, 146]. In figure 1C, the Z-potential of the isolated exosomes was found to be -16.03 mV ± 0.72, which was similar to Z-potential of exosomes obtained from HEK293T [147]. In order to confirm the quality of the exosomes, TEM was used to evaluate exosomes, with uranyl acetate staining to improve the contrast. As shown in figure 1D, the exosomes present a spherical entities with an average diameter of 50 nm. The physicochemical properties of the control PEGlyated nanoparticle is provided in supplemental figure 1.

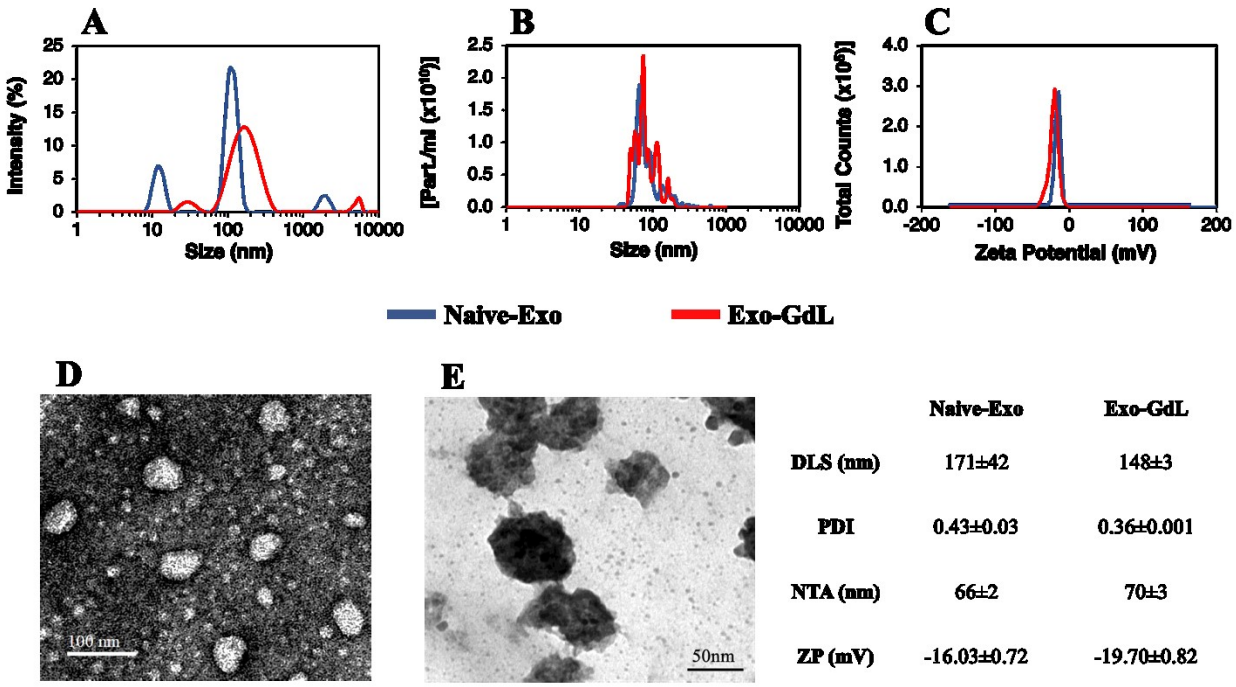

	Naive-Exo	Exo-GdL
DLS (nm)	171±42	148±3
PDI	0.43±0.03	0.36±0.001
NTA (nm)	66±2	70±3
ZP (mV)	-16.03±0.72	-19.70±0.82

Figure 5. Physicochemical characterization of exosomes. (A) Dynamic light scattering (DLS) of naive exosomes (blue line) and gadolinium labeled exosomes (red line). Notice there was a trend for the particles to increase in size after gadolinium labeling. (B) Nanoparticle tracking analysis (NTA) of naive exosomes (blue line) and gadolinium labeled exosomes (red line). No changes were observed using this method after gadolinium labeling, (C) Z-potential (ZP) of naive exosomes (blue line) and gadolinium labeled exosomes (red line). No changes were observed using this method after gadolinium labeling, (D) Negative staining of naive exosomes (naive-Exo) visualized with transmission electron microscopy (TEM), and (E) Positive staining of gadolinium labeled exosomes (Exo-GdL) visualized with TEM.

After characterizing naive exosomes, they were labeled with GdL using the lipid insertion technique followed by extrusion through the 200 nm membrane. The resulting Exo-GdL exhibit unimodal distribution as demonstrated in figure 1A with the hydrodynamic size of 148 nm ± 3,

NTA mode of 70 ± 3 and a PDI of 0.36 ± 0.001. These differences are most likely do to the unifying effect of extrusion. In addition, the measurement of Exo-GdL Z-potential revealed a net charge of -19.70 mV ± 0.82. The reduction in charge properties of Exo-GdL indicates the successful insertion of GdL into the membrane lipid bilayer. Nevertheless, as shown in figure 2E, the morphology and size of Exo-GdL remains grossly unchanged in TEM micrograph.

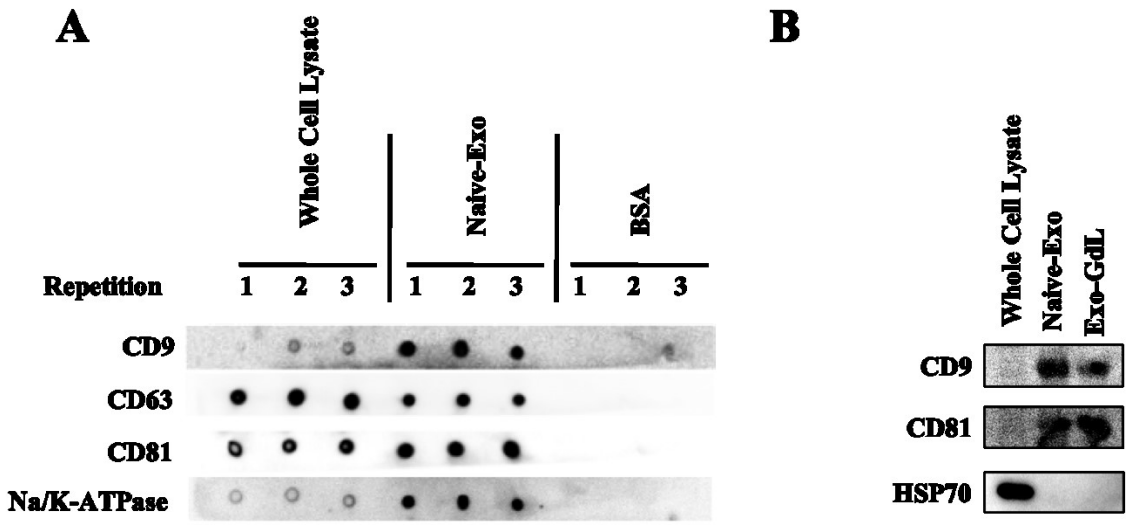

Figure 6. Dot blots and western blots of mesenchymal stromal cell (MSC) exosomes. A) Dot blots showing the expression of tetraspanins: clusters of differentiation (CD)9, CD63 and CD81, and sodium/ potassium ATPase (Na/K-ATPase) in naive-exosome samples obtained by ultracentrifugation of MSC (line HUC-257) conditioned media compared with whole cell lysate and bovine serum albumen (BSA). 2 µl of each sample [1 mg/ml] was loaded in triplicates on a PVDF membrane. B) western blots showing the expression of CD9 and CD81 in naive exosomes (Naive-Exo) and exosomes labeled with gadolinium (Exo-GdL). Notice that labeling the exosomes did not affect tetraspanin staining.

Exosomes are considering to be a product of cell membrane internalization and compartmentalization. Therefore, besides its unique membrane properties, exosomes also preserve the lipid and protein composition of the parent cells. Among the different protein markers present in exosomes, CD9, CD63, and CD81 are considered as exosome-specific proteins [148, 149]. Thus, to confirm the presence of these exosome markers, Dot and Western blot analysis was conducted. As depicted in figure 3B, the tetraspanins CD9 and CD81 were detected in exosomes but not in the whole cell lysate. This observation can be explained by the enrichment of these proteins in the exosomes samples rather than its absence on the cell membrane, which was confirmed by dot blots (figure 3A). Similarly, in the case of the HSP70, the protein was detected in the cell lysate by Western blot, but apparently, the concentration of this protein was relatively low in the naive exosomes causing the absence of protein band in Western blot analysis. After the insertion of GdL into exosome membrane, there were no differences in the expression of CD9 and CD81 between the naive exosomes and the Exo-GdL (figure 3B), implying that the labeling process does not alter its composition.

3.2. Preliminary studies

3.2.1. Human Umbilical Cord Mesenchymal Stroma Cell (HUC-MSC) Characterization.

Here, three lines of HUC-MSCs were used here. The characterization of HUC line 255 (HUC-255) and HUC-257 were previously reported in Smith *et al.* HUC-293 was isolated and characterized using established laboratory protocols [150]. The cells were characterized by flow cytometry, plastic adherences and expansion, and the tri-lineaage differentiation: adipogenic, chondrogenic and osteogenic differentiation assays.

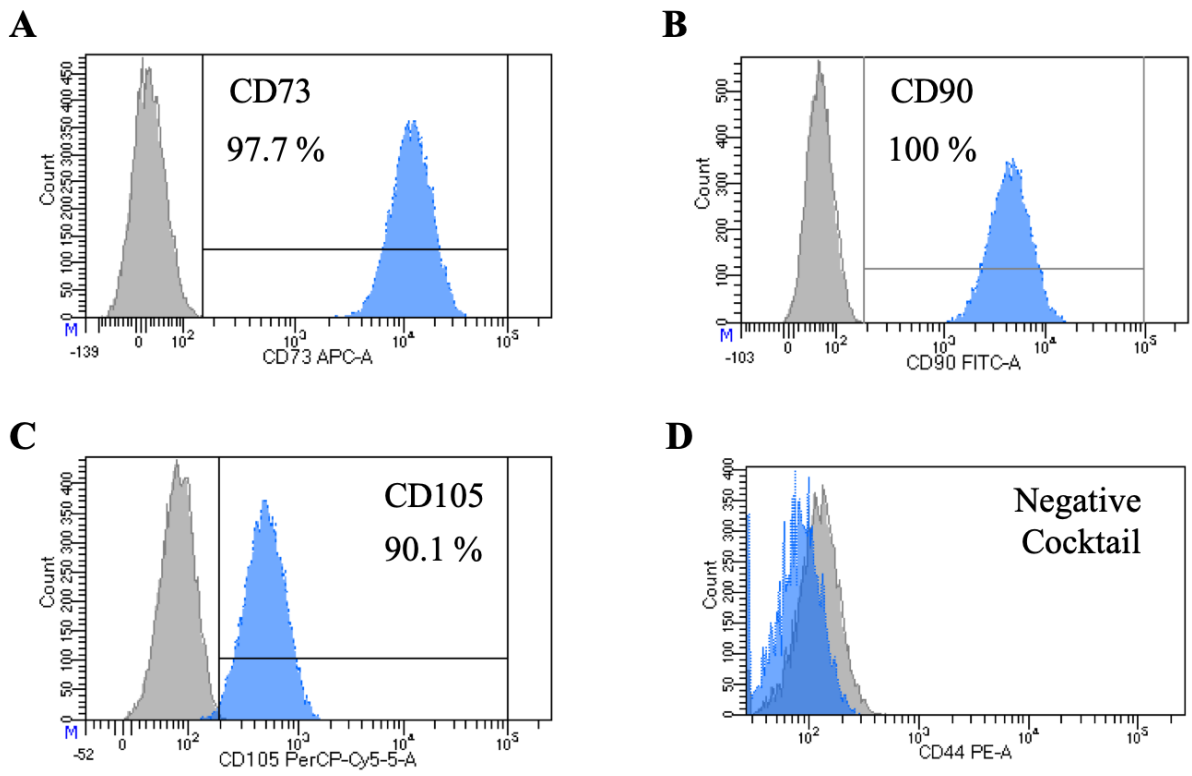

Figure 7. Flow cytometric analysis of human umbilical cord mesenchymal stromal cells (HUC-MSCs, line HUC-293). After growing to 80 % confluence, the HUC-293 cells were analyzed using the human MSC analysis assay (BD Stemflow™). Cells were positive to the antibodies to clusters of differentiation marker 73 (CD73, shown in A, 97.7 %), B) CD90 (100%) and C) CD105 (90.1 %). The cells stained negative for antibodies to D) CD34, CD45, CD11b, CD19, and Human Leukocyte Antigen- DR (HLA-DR) that were used as negative control in a cocktail. Gray histogram is the isotype control, the blue histogram is the indicated antibody staining.

3.2.1.1. Flow Cytometry of HUC-293

The analysis of HUC-293 by flow cytometry shows that these cells stain positive for surface marker CD73 (97.7%) (Figure 4A), CD90 (100%) (Figure 4B) and CD105 (90.1%) markers (Figure 4C). The MSCs stained negative for CD34, CD45, CD11b, CD19, and HLA-DR markers (Figure 4D). An average of 5000 events were analyzed per sample. These results agree with the recommendations of the ISCT and indicate that HUC-293 meets the definition of MSCs, as expected.

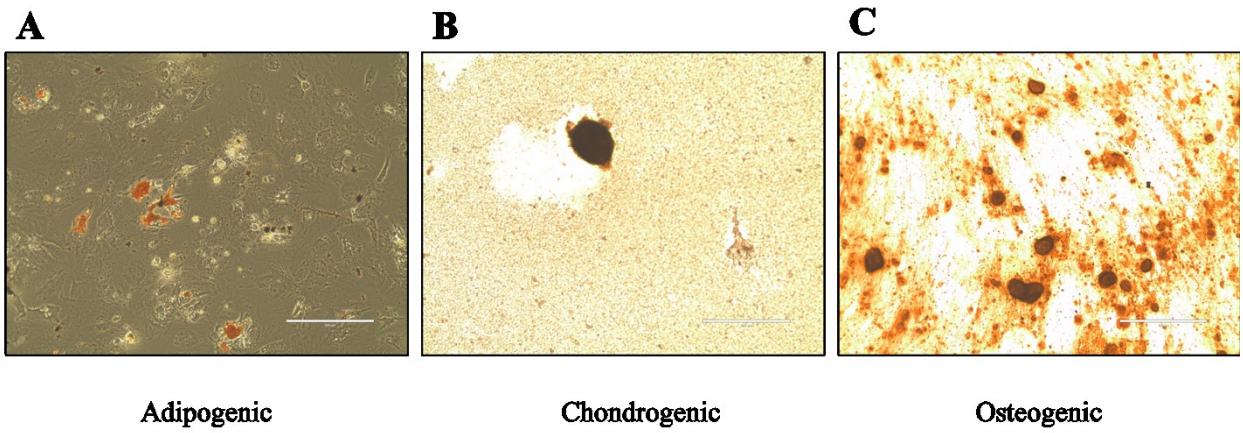

Figure 8. Differentiation assay of human umbilical cord mesenchymal stromal cells (HUC-MSCs, line HUC-293). The tri-lineage differentiation was induced by growing the cells in adipogenic, chondrogenic and osteogenic specific media (StemPro®, Thermo Fisher Scientific, Inc.). A) Adipogenic differentiation indicated by Oil Red staining of lipid droplets. B) Chondrogenic differentiation was indicated by Safranin O staining of proteoglycans in cartilage and C) Osteogenic differentiation was indicated by Alizarin Red S staining of calcium phosphate salts in bone. After 14-21 days of incubation on the specific media the cells culture was stained with 0.3% Oil Red solution (adipocytes), 0.1 % Safranin O solution (chondrocytes) and 2%

Alizarin Red S solution (osteocytes). Brightfield microscopy images collected at 20 × objective magnification. Calibration bars equal 200 μm.

3.2.1.2. HUC-MSC Differentiation assay

The tri-lineage differentiation assay demonstrated that HUC-293 fulfills the ISCT MSC minimal criteria. The accumulation lipid vacuoles in the cells was detected by Oil-red staining, indicating that the cells differentiated into adipocytes (Figure 5A). To determine the ability of the cells to form cartilage-like tissue, the chondrogenic differentiation culture was stained with Safranin O solution. The assay shows that the cell clusters were positive to the staining with Safranin O, indicating the presence of proteoglycans found in chondrocytes (Figure 5B). The staining with Alizarin Red S solution indicated the formation of calcium phosphate salts in the cell culture grown under the osteogenic media, indicating the cell differentiation into osteocytes (Figure 5C).

3.2.2. In-vitro assays

3.2.2.1. 3-(4,5-dimethylthiazol-2-yl)-2,5-diphenyltetrazolium bromide (MTT) cell metabolic assay (proliferation assay)

3.2.2.1.1.Effect of Exosomes on Cell Proliferation

The effect of exosomes on cell proliferation was evaluated with the 3-(4,5-dimethylthiazol-2-yl)-2,5-diphenyltetrazolium bromide (MTT) cell metabolic assay. This colorimetric assay is based on the principle that mitochondrias that are actively expressing succinate dehydrogenase in healthy cells can reduce the yellow color of the×× MTT reagent to formazan yielding a dark purple color. The difference in the color intensity obtained with this method can be quantified by spectrometric analysis and correlated to cell concentration. Thus, the MTT assay can determine the effect of

different exosome treatments on cell proliferation [151]. Here, the *in vitro* assay was designed in a 96-well plate format using the cancer cell lines: adenocarcinomic human alveolar basal epithelia cell line A549, adenocarcinoma human breast epithelia cell line MDA-MB-231, adenocarcinoma human prostate epithelia cell line PC-3, osteosarcoma mouse osteoblast cell line K7M2 and human mesenchymal stromal cell line HUC-MSCs 255. The data was analyzed as a Randomized Complete Block Design (RCBD) and least square means comparisons of orthogonal means using SAS.

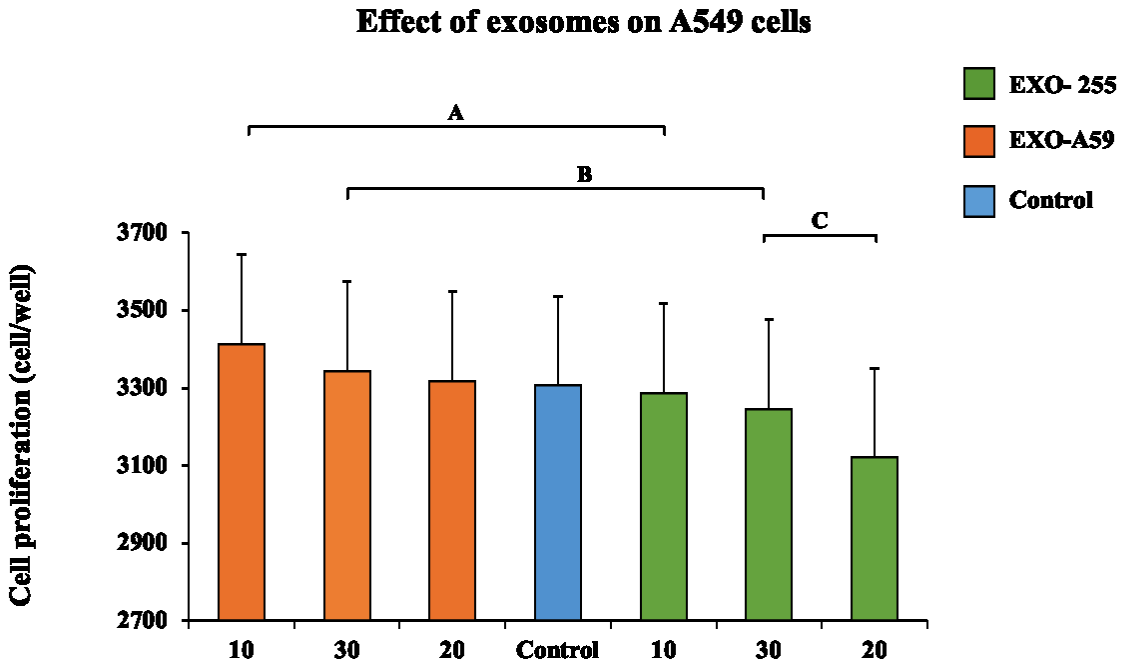

Figure 9. Dose- and source- dependent effects of exosomes on human cancer cell proliferation *in vitro*. Cell proliferation was evaluated by MTT assay in a 96-well plate format. Human lung carcinoma cells A549 were treated with 10 µg, 20 µg and 30 µg of human umbilical cord-derived mesenchymal stromal cells line 255 (HUC-255)-derived exosomes (Exo-255) or human lung

carcinoma A549-derived exosomes (Exo-A549) in a final volume of 10 µl. As a control, cells were treated with 10 µl of medium enriched with 10 % pooled human platelet lysate depleted of exosomes (Control). The data is expressed as estimated least squares means (LSM) plus or minus one standard deviation. The groups labeled with the same letter are not significantly different ($p < 0.05$).

First, an initial screening of exosomes' activity on cell proliferation was conducted using A549 cancer cells as the respondent cells. For this assay, 10, 20 and 30 µg of HUC-255 derived exosomes (Exo-255) or A549 adenocarcinoma-derived exosomes (Exo-A549) were added in a final volume of 10 µl to each 96-well cell culture. For control samples, 10 µl of Dulbecco's modified eagle medium (DMEM) were added to each control well. The exosome treatments affect A549 cell proliferation ($F = 4.31$, $P = 0.0044$). When compared with the control (3305.54 cell/well), there were significant differences of the Exo-255 at dose 20 µg (3120.05 cell/well), which inhibit the A549 cell proliferation ($t = 3.00$, $P = 0.0063$). Exo-255 at dose 10 µg (3287.05 cell/well) was significant different ($t = 2.7$, $P = 0.0126$) to Exo-225 dose 20 µg (3120.05 cell/well) but not dose 30 µg. The highest proliferation was obtained with Exo-A549 at a dose of 10 µg (3411.71 cell/well) exhibiting significant differences when compare with Exo-255 20 µg ($t = -4.71$, $P < 0.0001$) (Figure 6). Next, the effect of the same treatments was tested on human prostate cancer (PC-3) cells. Similar results were observed on the effect of exosomes on PC-3 cell proliferation (F value = 81.46, $P < 0.0001$). The highest proliferation was obtained with the Exo-A549 treatment at a dose of 10 µg (549.26 cell/well). The highest reduction was obtained with the Exo-255 treatments at 10 µg (446.34 cell/well) and 20 µg (442.62 cell/well). There were significant differences of all treatments compared with the Control. Even though there was not a dose effect between the

treatments with Exo-255, there were significant differences when the dose of HUC exosomes were compared to Exo-A549 at different doses (Figure 7). A summary of the differences of treatments LSM is shown in table 3.

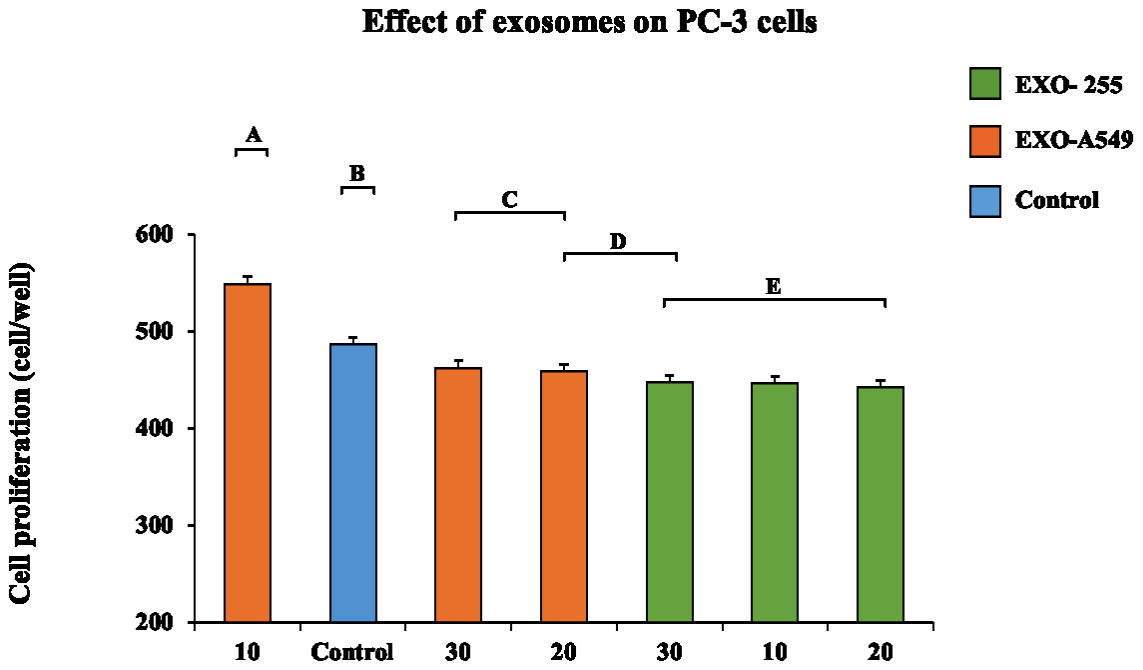

Figure 10. Dose- and source- dependent effect of human mesenchymal cell derived exosomes on human prostate adenocarcinoma PC-3 cell proliferation. Cell proliferation was evaluated by MTT assay in a 96-well plate format. PC-3uman prostate adenocarcinoma cells were treated with 10 µg, 20 µg and 30 µg of HUC-255-derived exosomes (Exo-255) or A549 human lung carcinoma derived exosomes (Exo-A549) in a final volume of 10 µl. As a control, the cells were treated with 10 µl of Dulbecco's modified eagle medium DMEM supplemented with 10% pooled human platelet lysate depleted of exosomes (Control). The data is expressed as estimated least

squares mean (LSM) plus or minus one standard deviation. The groups indicated with the same letter are not significantly different ($P < 0.05$).

To further explore the impact of HUC-MSC exosomes on other cell lines, their effects on HUC-255 cell proliferation was conducted (Figure 8). For this experiment, 2.5, 5 and 10 µg of exosomes were tested. Interestingly, there was a dose-response effect with the Exo-A549, where 2.5 µg (2004.03 cell/well) exhibit the highest cell proliferation, followed by 5 µg (1859 cell/well) and 10 µg (1821 cell/well). In the case of Exo-255, even though there was not a dose response effect, the inhibition in proliferation was significantly different when compared with the Exo-A549 at 2.5 ng (3287.05 cell/well) (t = -5.56, $P < 0.0001$), 5 ng (3245.08 cell/well) (t = -4.13, $P = 0.0004$) and 10 ng (3120.05 cell/well) (t = -3.72, $P = 0.0011$) (Figure 8). This data suggest that exosomes have an effect on cell proliferation *in vitro* and that could vary depending upon the source of the exosomes and the dose. This evidence indicates that HUC-MSCs-derived exosomes inhibit the proliferation HUC-MSCs (F value = 10.79, $P < 0.0001$) it is still unknown whether HUC-MSCs exosomes will inhibit cancer cell lines other than those tested here. A summary of the differences of treatments LSM is shown in table 4.

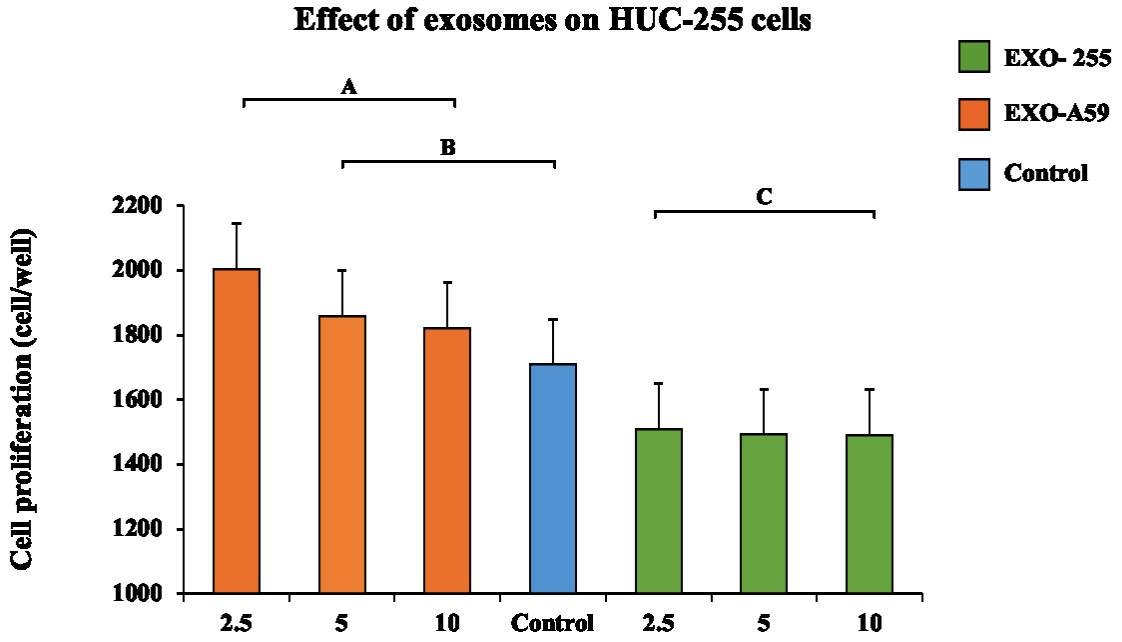

Figure 11. Dose- and Source-dependent effects of exosomes on cell proliferation. Cell proliferation was evaluated by MTT assay in a 96-well plate format. Human mesenchymal stromal cells (HUC-MSCs, line 255, HUC-255) was treated with 2.5 µg, 5 µg and 10 µg of HUC-255-derived exosomes (Exo-255) or A549 human lung carcinoma derived exosomes (Exo-A549) in a final volume of 10 µl. As control the cells were treated with 10 µl of Dulbecco's modified eagle medium supplemented with 10% human pooled platelet lysate (HPL) depleted of exosomes. The data is expressed as estimated least squares mean (LSM) plus one standard deviation. The groups with the same letter are not significantly different ($p < 0.05$).

3.2.2.1.2. Effect of Gadolinium-Labeled Exosomes on K7M2 Adenocarcinoma Cells.

Next, we determined if human mesenchymal stromal cell-derived exosomes that had been labeled using the magnetic resonance contrast agent, gadolinium, affect mouse osteosarcoma cell line K7M2 proliferation. A preliminary experiment was conducted where exosomes from HUC-257 were labeled with gadolinium lipid (Exo-257-GdL) and their effect on cell proliferation was determined using MTT assay. Here, doses 10, 20 and 30 ng of gadolinium labeled exosomes were provided to K7M2 osteosarcoma cells for 24 hours. Exosome treatment significantly affected K7M2 cells proliferation (F value = 5.32, P = 0.0013). When compared with the control (2630.06 cell/well), there was no significant differences between doses of Exo-257-GdL at 10 ng (2516.47cell/well), 20 ng (2510.86 cell/well) and 30 ng (2493.30 cell well). When compared with dose 10 ng of Exo-257 (2810.58 cell/well), there were significant decreased proliferation at dose 10 ng (t = -4.27, P = 0.0003) (2516.47 cell/well), 20 ng (t = -4.36, P = 0.0002) (2523.98 cell/well) and 30 ng (t = -4.61, P = 0.0001)(2558.91 cell/well). However, at the lowest dose, 10 ng, Exo-255 stimulated proliferation of the K7M2 cells (3046.25 cell/well) (Figure 9). A summary of the differences of treatments LSM is shown in table 5.

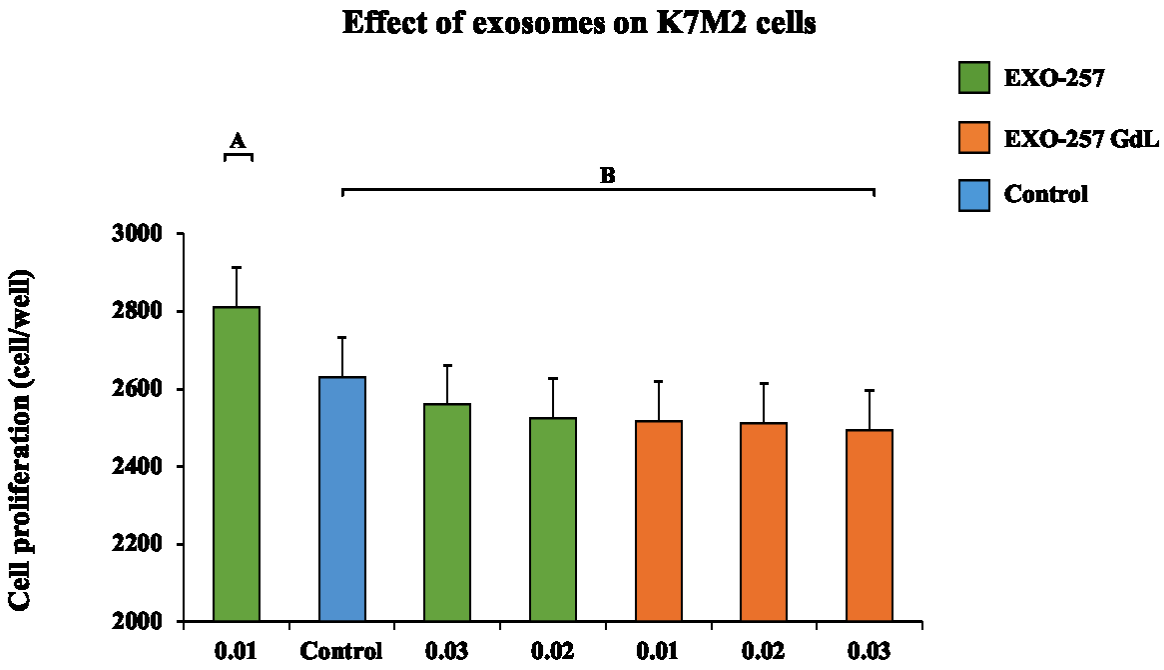

Figure 12. Effect of Gadolium labeled human mesenchymal stromal cell derived exosomes on mouse osteosarcoma cell proliferation. Cell proliferation was evaluated by MTT assay in a 96-well plate format. K7M2 mouse osteosarcoma cells were treated with 10 ng, 20 ng and 30 ng of human mesenchymal stromal cell derived exosomes (HUC-MSCs, line 257)-derived exosomes (Exo-257) or Exo-257 labeled with gadolinium (Exo-257-GdL) in a final volume of 10 µl. As a control, the cells were treated with 10 µl of Dulbecco's modified eagle medium supplemented with 10% human pooled platelet lysate depleted of exosomes. The data is expressed as estimated least squares mean (LSM) plus one standard deviation. The groups with the same letter are not significantly different ($p < 0.05$).

Then, to evaluate whether the effects of exosomes from the same cell type were reproducible between different MSC lines, the same experiment was repeated with exosomes isolated from HUC-MSC line 293 (Exo-293). The result were consistent with the ones obtained with the Exo-

255. There was evidence of the effect of exosomes on K7M2 osteosarcoma cells (F value = 4.59, P = 0.0031). Compare with the control (3378.6 cell/well), the highest proliferation was obtained with the lowest dose 10 ng of Exo-293 (3783.28 cell/well) (t = -3.62, P = 0.0014) and greater inhibition was observed with the 30 ng dose of Exo-293-GdL (3237.42 cell/well). There were significant differences between Exo-293-GdL at dose 30 ng and Exo-293 at doses 10 ng (t = -4.88, P < 0.0001) and 20 ng (t = -2.09, P = 0.0478). Comparing the two sources of exosomes at dose 10 ng, there was a significant difference (t = -3.57, P=0.0015). However, there was no differences between the Exo-293 and EXo-293-GdL at doses 20 and 30 ng (Figure 10). This result suggested that there is no anti-proliferative effect of the Exo-GdL compare with the naive exosomes and the control *in vitro*. A summary of the differences of treatments LSM is shown in table 6.

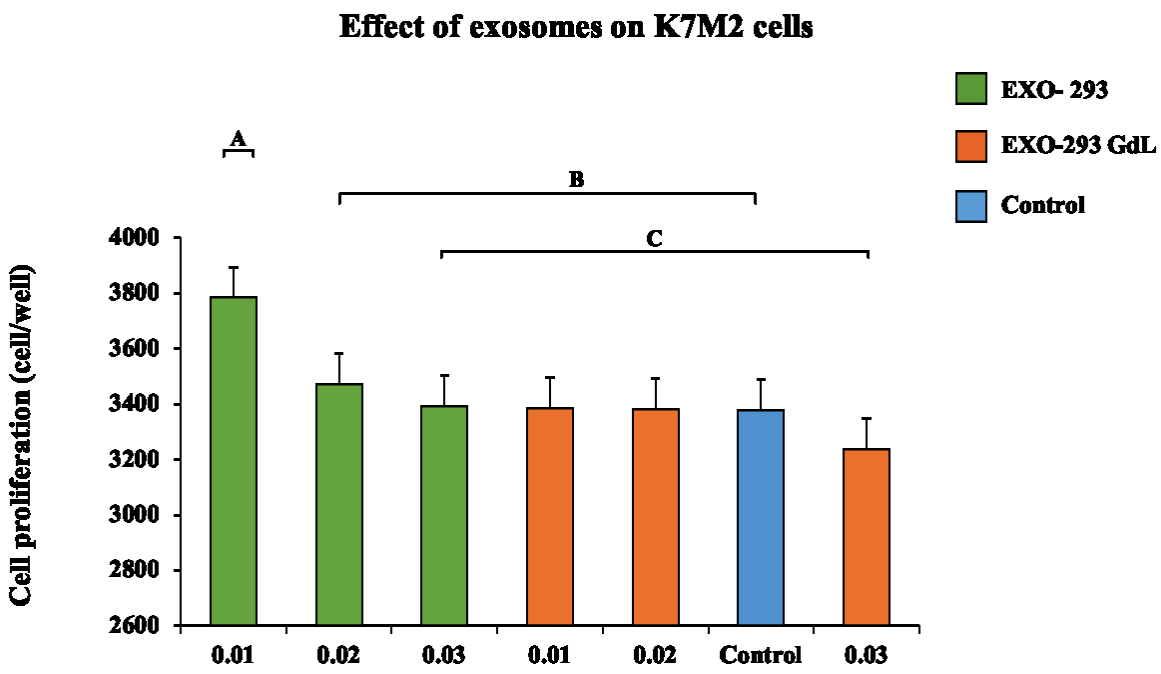

Figure 13. Effect of human mesenchymal stromal cell-derived (HUC-MSC) exosomes on osteosarcoma cell proliferation. Cell proliferation was evaluated by MTT assay in a 96-well plate format. K7M2 mouse osteosarcoma cells were treated with 10 ng, 20 ng and 30 ng exosomes derived from HUC-MSCs line 293 (Exo-293) or gadolinium-labeled exosomes (Exo-293-GdL) in a final volume of 10 µl. As control the cells were treated with 10 µl of Dulbecco's modified eagle medium supplemented with 10% human pooled platelet lysate depleted of exosomes. The data is expressed as estimated least squares mean (LSM) plus or minus one standard deviation. The groups with the same letter are not significantly different ($p < 0.05$).

3.2.2.1.3. Effect of Exosomes derived from stimulated human mesenchymal stromal cells on Cancer Cell proliferation.

MSCs have a great potential as therapeutics in regenerative medicine. One of their most important characteristics is the ability to change from pro- to anti-inflammatory phenotype depending on chemical stimuli; theoretically, the MSCs' exosomes would change, too. This preliminary study evaluated the effect exosomes obtained from stimulated MSCs compared with exosomes isolated from naive MSCs on cancer cell proliferation.

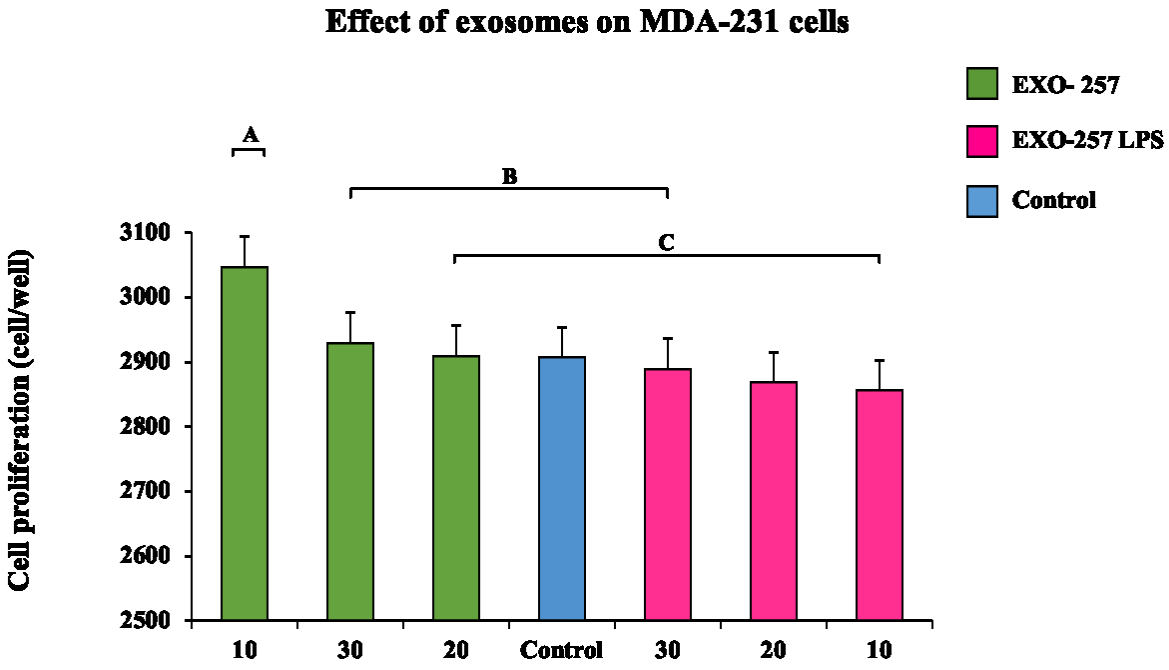

Figure 14. Effect of exosomes derived from lipopolysaccharide (LPS) stimulated human mesenchymal stromal cell (HUC-MSCs) on breast cancer cell proliferation. Cell proliferation was evaluated by MTT assay in a 96-well plate format. MDA-231 human breast adenocarcinoma cells were treated with 10 µg, 20 µg and 30 µg of HUC-MSC-derived exosomes (derived from cell

line 257, Exo-257) or LPS-stimulated HUC-257-derived exosomes (Exo-257-LPS) in a final volume of 10 µl. As control the cells were treated with 10 µl of Dulbecco's modified eagle medium supplemented with 10% human pooled platelet lysate depleted of exosomes. The data is expressed as estimated least squares mean (LSM) plus or minus one standard deviation. The groups with the same letter are not significantly different ($P < 0.05$).

The first assay evaluated the effect of exosomes derived from HUC-MSCs that had been stimulated by exposure to the Toll-like receptor 4 (TLR4) agonist lipopolysaccharide (Exo-LPS) using the protocol described in [152]. MDA-231 breast adenocarcinoma cells were exposed to Exo-LPS at three different doses10, 20 and 30 µg overnight and the next day proliferation was assessed by MTT. Exposure of MDA-231 adenocarcinoma cells to Exo-LPS treatments has a significant effect on proliferation (F value = 7.21, $P = 0.0002$). In compared with the control (2907 cell/well), only Exo-257 inhibit MDA-231 cell proliferation at 10 µg (2855.53 cell/well) ($t = -4.19$, $P = 0.0003$). There were significant differences between Exo-257 at dose 10 ng compared with Exo-257-LPS at doses 10 ng ($t = 5.73$, $P < 0.0001$), 20 µg ($t = -5.36$, $P < 0.0001$) and 30 µg ($t = -4.73$, $P < 0.0001$). The cells treated with Exo-257 grew faster than control and Exo-257-LPS. (Figure 11). A summary of the differences of treatments LSM is shown in table 7.

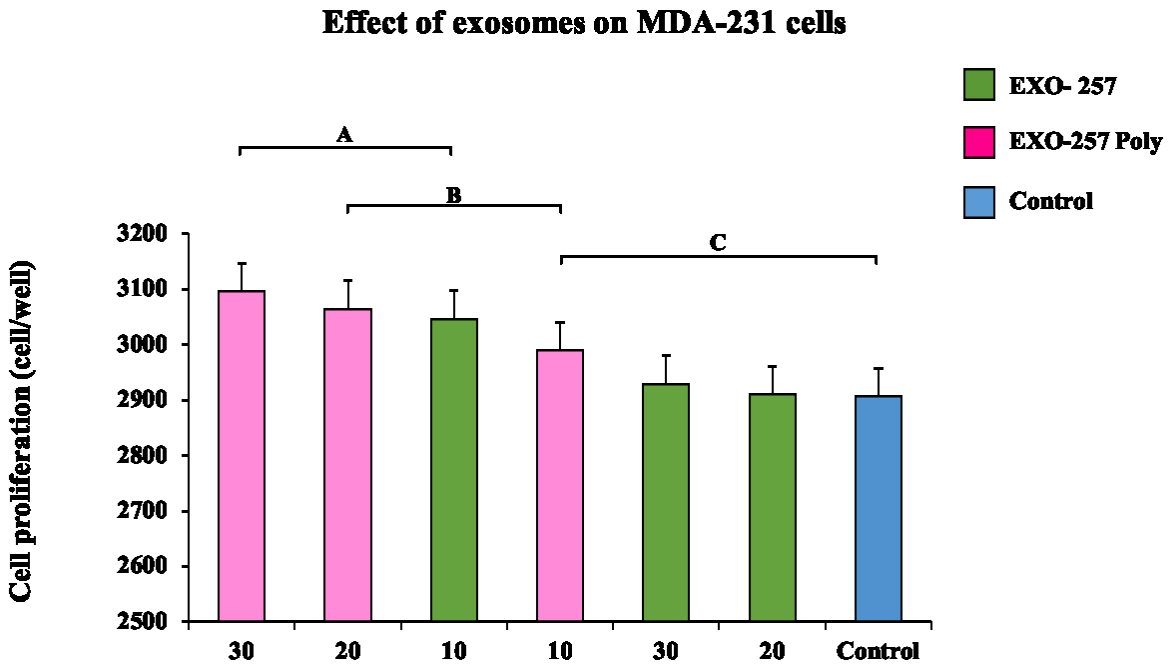

Figure 15. Effect of poly (I:C) stimulated human mesenchymal stromal cell (HUC-MSC)-derived exosomes on cancer cell proliferation. Cell proliferation was evaluated by MTT assay in a 96-well plate format. MDA-231 human breast adenocarcinoma cells were treated with 10 µg, 20 µg and 30 µg of HUC-MSCs derived from line 257 exosomes (Exo-257) or poly I:C stimulated HUC-MSC, line 257-derived exosomes (Exo-257-Poly) in a final volume of 10 µl. As control the cells were treated with 10 µl of Dulbecco's modified eagle medium supplemented with 10% human pooled platelet lysate depleted of exosomes. The data is expressed as estimated least squares mean (LSM) plus or minus one standard deviation. The groups labeled with the same letter are not significantly different ($p < 0.05$).

Next, the exosomes were derived from HUC-MSCs stimulated with Toll-like receptor-3 agonist (TLR3) poly inosinic: cytidylic acid (Exo-Poly), Poly I:C stimulation, also called TLR3

stimulation was performed following the protocol of [152]. Previous work showed that poly I:C stimulation of HUC-MSCs enhances their immune modulatory effects [153]. Here, we queried whether TLR3 stimulation modifies MSC exosomes by testing them on cancer cell proliferation. Exo-Poly treatments significantly affected MDA-231 cell proliferation (F value = 5.61, P = 0.0009). Compared with the control (2907 cells/well), there was an increase in cell proliferation by Exo-Poly at doses 20 μg (3064.03 cell/well) (t = -4.03, P = 0.0005) and 30 μg (3096 cell/well) (t = -4.03, P = 0.0005). The lowest cell proliferation was observed with the Exo-257 treatments at dose 20 μg (2910 cell/well) and 30 μg (2930 cell/ well) (Figure 12). A summary of the differences of treatments LSM is shown in table 8.

Finally, the effect of interferon gamma (IFN-γ) stimulation of human mesenchymal stromal cell exosomes (Exo-IFN) was evaluated. Here, a IFN stimulation protocol that was previously shown to increase the expression of the immune modulatory substance indoleamine 2,3-dioxygenase (IDO) by human mesenchymal stromal cells was used [154]. Exo-IFN treatment found to significantly affect mouse osteosarcoma cell proliferation (F value = 11.33, P < 0.0001). There was a reduction on mouse osteosarcoma cell proliferation by exposure to Exo-IFN at doses 10 ng (2516 cell/well) (t = 3.57, P = 0.0017) and the 20 ng (2510 cell/well) (t = 4.67, P < 0.0001) and 30 ng (2493 cell/ well) (t = 3.61, P = 0.0014) compared with the control (2630 cell/well). The highest proliferation was observed with Exo-257 at dose 10 ng (2811 cell/well). There were significant differences between both treatments at dose 10 ng (t = -5.55, P < 0.0001). At dose 20 ng Exo-IFN were significant different when compared with Exo-257 at doses 10 ng (t = -6.69, P < 0.0001) and 20 ng (t = -2.93, P = 0.0074). Exo-IFN at dose 30 ng was also significant different to Exo-257 at dose 10 ng (t = -5.63, P < 0.0001) (Figure 13). These data suggest that HUC-MSCs exposure to

IFN alters HUC-MSC exosome contents. This preliminary evaluation requires further work to confirm. A summary of the differences of treatments LSM is shown in table 9.

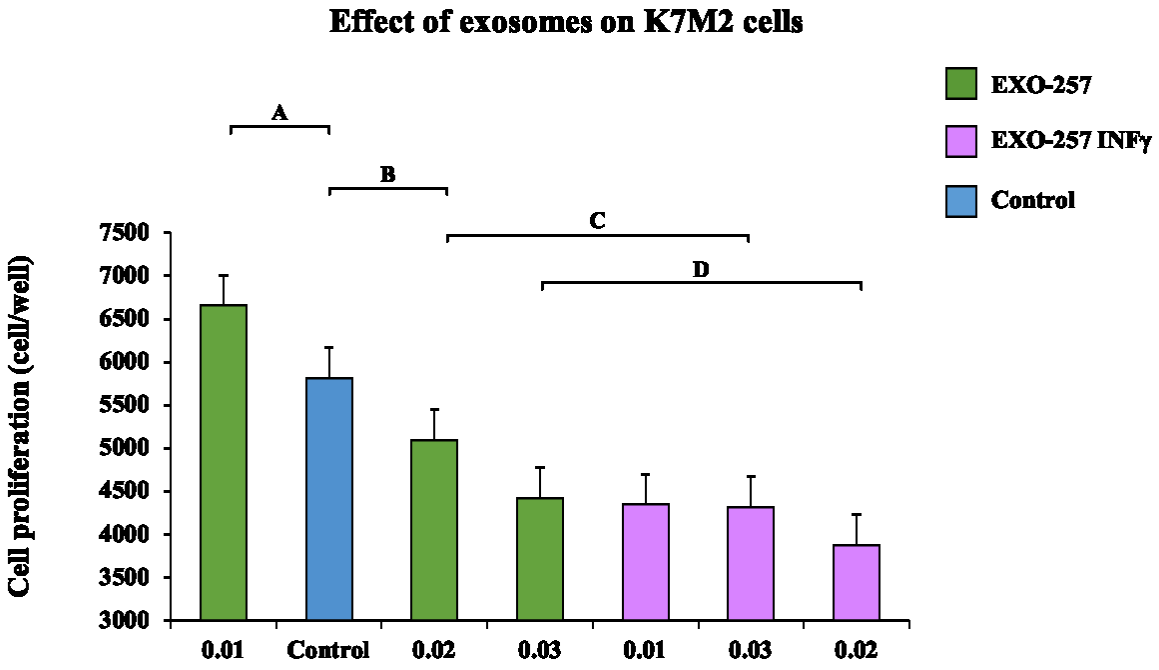

Figure 16. Effect of interferon gamma (IFN-γ) stimulated human mesenchymal stromal cell-derived (HUC-MSC) exosomes on cancer cell proliferation. The proliferation of mouse K7M2 osteosarcoma cells was evaluated by MTT assay in a 96-well plate format. Osteosarcoma cells were treated with 10 ng, 20 ng and 30 ng of HUC-MSC (line 257)-derived exosomes (Exo-257) or IFN-γ stimulated HUC-MSC-257-derived exosomes (Exo-257-IFN) in a final volume of 10 µl. As control the cells were treated with 10 µl of Dulbecco's modified eagle medium supplemented with 10% human pooled platelet lysate depleted of exosomes. The data are expressed as estimated least squares mean (LSM) plus or minus one standard deviation. The groups with the same letter are not significantly different ($p < 0.05$).

3.2.2.1.4.Evaluation of the genetic expression of stimulated HUC-MSCs.

In order to better understand the effect of LPS, IFN, or poly I:C stimulation of HUC-MSCs on the production of exosomes, the gene expression was assessed using reverse transcriptase polymerase chain reaction (RT-PCR) of TRAIL, TLR3, TLR4 and CXCL9, since previous work had indicated that the expression of these genes could be modified in MSCs [152]. HUC-MSC lines 255, 257 and 293 were stimulated with 10 ng/ml of LPS, 1µg/ml of Poly (I:C) or 10 ng/ml of IFN-γ, diluted to a final volume of 10 µl, for 24 hours. As negative control, 10 µl. of DPBS was added to the control cell cultures. RNA from the treated cells was isolated, reverse-transcribed to cDNA and evaluated by PCR. All three HUC-MSCs cell lines responded similarly to the stimulation (Figure 14). There were no differences between the control treatment and LPS and Poly (I:C) treatments. However, in the case of IFN-γ treatment, there was increased expression of TRAIL and CXCL9 genes. Based on these results, LPS and Poly (I:C) stimulation of MSCs did not change their expression of TLR3 and TLR4. However, the expression of TLR3 was higher compared with TLR4 (Figure 14).

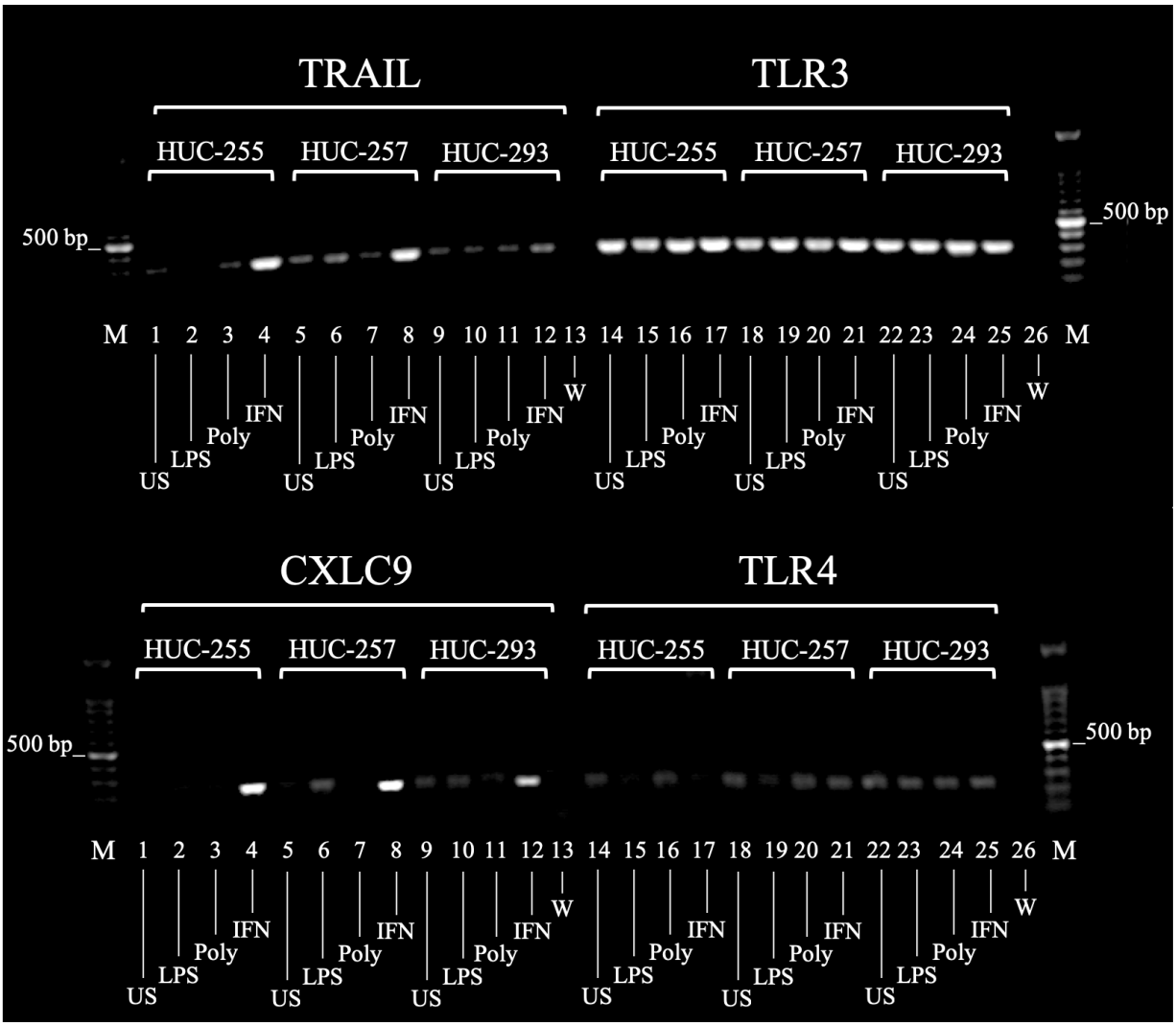

Figure 17. Effect of the stimulation by lipopolysaccharide (LPS), Interferon γ (IFN), or poly I:C (Poly) on human mesenchymal stromal cell (HUC-MSC) gene expression. Results of the genetic screening of TRAIL, CXCL9, TLR3 and TLR4 by reverse transcriptase polymerase chain reaction (RT-PCR) on HUC-MSC lines 255, 275 and 293 after stimulation. HUC-MSCs were exposed overnight to LPS (10 ng/ml), Poly (I:C) (1µg/ml) or IFN-γ (10 ng/ml). IFN-γ stimulation enhanced the expression of TRAIL and CXCL9 genes in all the HUC-MSC lines. There were no

differences in the expression of TLR3 and TLR4 genes in the stimulated or unstimulated cells. US: Unstimulated, W: water. M: 100 bp molecular marker.

To corroborate the results obtained with IFN-γ in the initial screening, a new assay was conducted under the same experimental conditions. The results indicate that HUC-257 IFN-γ stimulated cells, exhibit higher expression the TRAIL and CXCL9 genes, compared with the unstimulated control. However, there were no differences in expression of TLR3 and TLR4 genes (Figure 15).

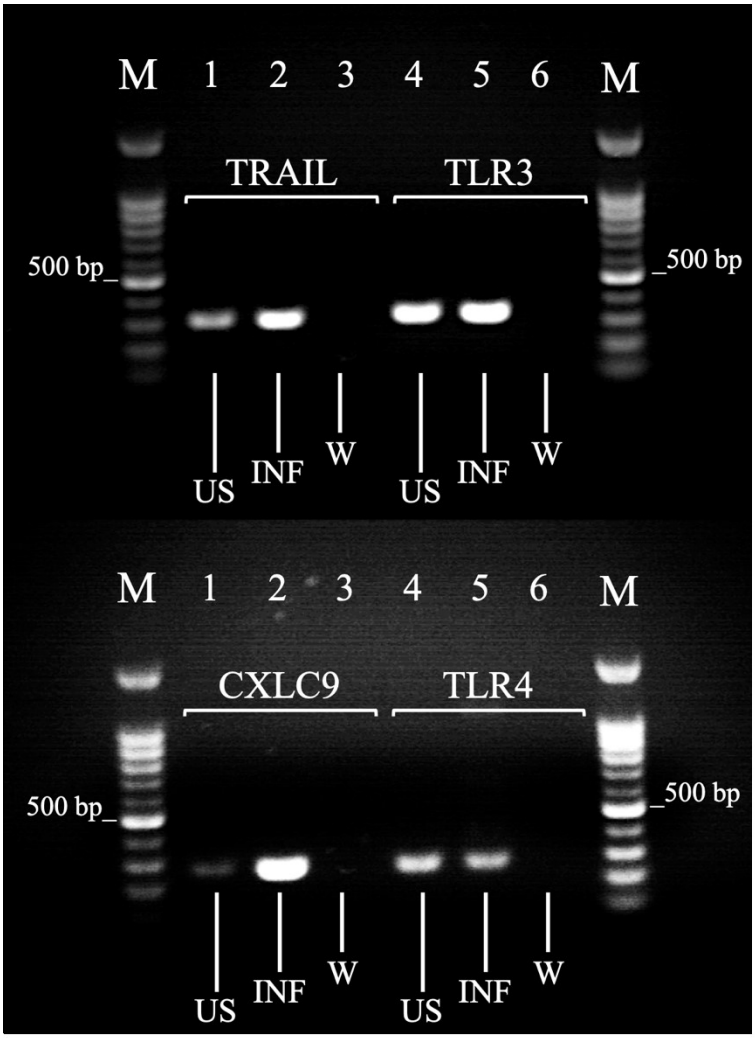

Figure 18. Effect of the stimulation by Interferon gamma (IFN-γ) on human mesenchymal stromal cell (HUC-MSC) gene expression. Results of the genetic screening of TRAIL, CXCL9, TLR3 and TLR4 by reverse transcriptase polymerase chain reaction (RT-PCR) in HUC-257 cell line. HUC-MSCs were exposed to IFN-γ (10 ng/ml) overnight before the cells were collected for genetic analysis. 10 µl of DPBS was the unstimulated control. IFN-γ stimulated cells enhanced the expression of TRAIL and CXCL9 genes. There were no differences in the expression of TLR3 and TLR4 genes in the stimulated or unstimulated cells. US: Unstimulated, W: water. M: 100 bp molecular marker.

3.2.2.1.5.Evaluation of the genetic expression of HUC-MSC cells stimulated with IFN-γ by semiquantitative RT-PCR.

To further investigate the effect of IFN-γ on HUC-257 cells, a semiquantitative RT-PCR trial was conducted. There was an up-regulation of expression of CXCL9, TRAIL and TLR3 in the IFN-γ stimulated MSCs compared with the unstimulated control. There were no differences in the expression of TLR4. These results indicated that MSCs exposure overnight to IFN-γ affects immune cytokines expression (Figure 16).

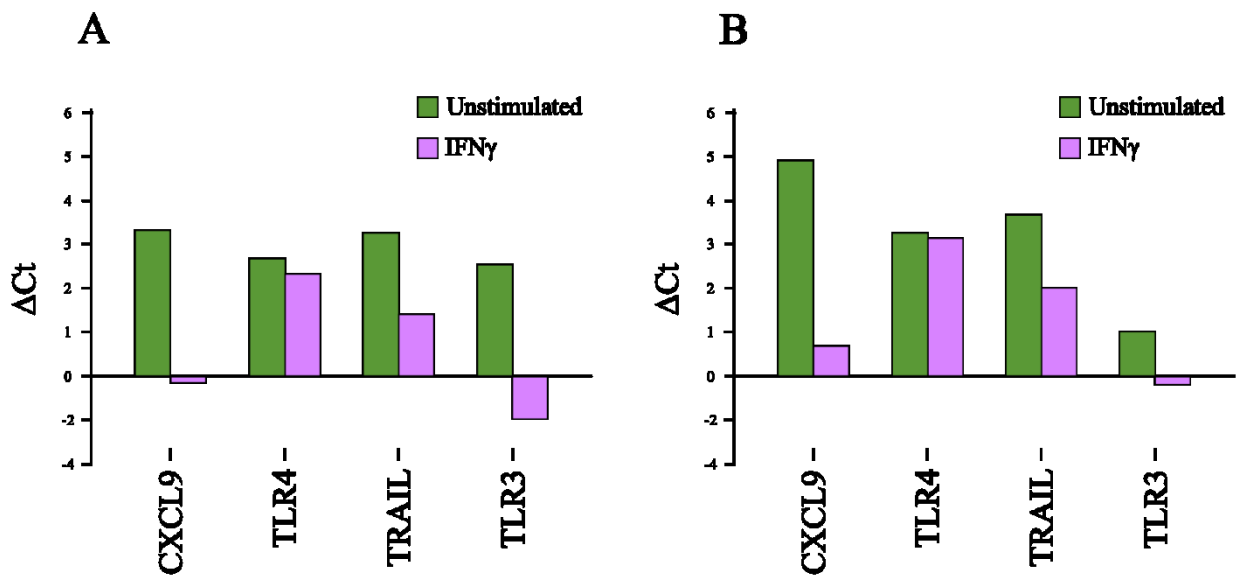

Figure 19. Effect of interferon gamma (IFN-γ) stimulation of human mesenchymal stromal cells on gene expression. Results of the genetic screening of TRAIL, CXCL9, TLR3 and TLR4 by semiquantitative reverse transcriptase polymerase chain reaction (RT-PCR) of IFN-γ stimulated human mesenchymal stromal cells or control. A) 4 ng of HUC-257 cDNA. B) 40 ng of HUC-257 cDNA. Genetic expression was normalized by the threshold count (C_t) difference of the geometric mean of the housekeeping genes Porphobilinogen deaminase (PGBD) and 5'-aminolevulinate synthase (ALAS 1) (ΔC_t). IFN-γ stimulated MSCs show upregulation of CXCL9, TRAIL and TLR3 genes in comparison with unstimulated control.

Table 4. Differences of Treatments Least Squares Means (LSM) on A549 cells.

Treatment	Treatment	Estimate	Standard Error	DF	*t* Value	Pr > |t|
Control	Eexo-255D10	18.4878	61.9143	24	0.30	0.7678
Control	Eexo-255D20	185.50	61.9143	24	3.00	0.0063*
Control	Eexo-255D30	60.4610	61.9143	24	0.98	0.3385
Control	Eexo-A549D10	-106.17	61.9143	24	-1.71	0.0993
Control	Eexo-A549D20	-11.4348	61.9143	24	-0.18	0.8550
Control	Eexo-A549D30	-37.6576	61.9143	24	-0.61	0.5488
Eexo-255D10	Eexo-255D20	167.01	61.9143	24	2.70	0.0126*
Eexo-255D10	Eexo-255D30	41.9732	61.9143	24	0.68	0.5043
Eexo-255D10	Eexo-A549D10	-124.66	61.9143	24	-2.01	0.0554
Eexo-255D10	Eexo-A549D20	-29.9226	61.9143	24	-0.48	0.6333
Eexo-255D10	Eexo-A549D30	-56.1454	61.9143	24	-0.91	0.3735
Eexo-255D20	Eexo-255D30	-125.04	61.9143	24	-2.02	0.0547
Eexo-255D20	Eexo-A549D10	-291.67	61.9143	24	-4.71	<.0001*
Eexo-255D20	Eexo-A549D20	-196.93	61.9143	24	-3.18	0.0040*
Eexo-255D20	Eexo-A549D30	-223.15	61.9143	24	-3.60	0.0014*
Eexo-255D30	Eexo-A549D10	-166.63	61.9143	24	-2.69	0.0128*
Eexo-255D30	Eexo-A549D20	-71.8958	61.9143	24	-1.16	0.2570
Eexo-255D30	Eexo-A549D30	-98.1186	61.9143	24	-1.58	0.1261
Eexo-A549D10	Eexo-A549D20	94.7346	61.9143	24	1.53	0.1391
Eexo-A549D10	Eexo-A549D30	68.5118	61.9143	24	1.11	0.2795
Eexo-A549D20	Eexo-A549D30	-26.2228	61.9143	24	-0.42	0.6757

Table 5. Differences of Treatments Least Squares Means (LSM) on PC-3 cells.

Treatment	Treatment	Estimate	Standard Error	DF	*t* Value	Pr > |t|
Control	Eexo-255D10	40.5716	5.9070	24	6.87	<.0001*
Control	Eexo-255D20	44.2944	5.9070	24	7.50	<.0001*
Control	Eexo-255D30	38.7956	5.9070	24	6.57	<.0001*
Control	Eexo-A549D10	-62.3470	5.9070	24	-10.55	<.0001*
Control	Eexo-A549D20	27.8570	5.9070	24	4.72	<.0001*
Control	Eexo-A549D30	24.2608	5.9070	24	4.11	0.0004*
Eexo-255D10	Eexo-255D20	3.7228	5.9070	24	0.63	0.5345
Eexo-255D10	Eexo-255D30	-1.7760	5.9070	24	-0.30	0.7663
Eexo-255D10	Eexo-A549D10	-102.92	5.9070	24	-17.42	<.0001*
Eexo-255D10	Eexo-A549D20	-12.7146	5.9070	24	-2.15	0.0416*
Eexo-255D10	Eexo-A549D30	-16.3108	5.9070	24	-2.76	0.0109*
Eexo-255D20	Eexo-255D30	-5.4988	5.9070	24	-0.93	0.3612
Eexo-255D20	Eexo-A549D10	-106.64	5.9070	24	-18.05	<.0001*
Eexo-255D20	Eexo-A549D20	-16.4374	5.9070	24	-2.78	0.0103*
Eexo-255D20	Eexo-A549D30	-20.0336	5.9070	24	-3.39	0.0024*
Eexo-255D30	Eexo-A549D10	-101.14	5.9070	24	-17.12	<.0001*
Eexo-255D30	Eexo-A549D20	-10.9386	5.9070	24	-1.85	0.0764*
Eexo-255D30	Eexo-A549D30	-14.5348	5.9070	24	-2.46	0.0215*
Eexo-A549D10	Eexo-A549D20	90.2040	5.9070	24	15.27	<.0001*
Eexo-A549D10	Eexo-A549D30	86.6078	5.9070	24	14.66	<.0001*
Eexo-A549D20	Eexo-A549D30	-3.5962	5.9070	24	-0.61	0.5484

Table 6. Differences of Treatments Least Squares Means (LSM) on HUC-255 cells.

Treatment	Treatment	Estimate	Standard Error	DF	*t* Value	Pr > |t|
Control	Eexo-255D10	218.68	89.0060	24	2.46	0.0216*
Control	Eexo-255D2.5	199.82	89.0060	24	2.24	0.0343*
Control	Eexo-255D5	216.98	89.0060	24	2.44	0.0226*
Control	Eexo-A549D10	-112.38	89.0060	24	-1.26	0.2189
Control	Eexo-A549D2.5	-295.47	89.0060	24	-3.32	0.0029*
Control	Eexo-A549D5	-150.33	89.0060	24	-1.69	0.1042
Eexo-255D10	Eexo-255D2.5	-18.8608	89.0060	24	-0.21	0.8340
Eexo-255D10	Eexo-255D5	-1.6982	89.0060	24	-0.02	0.9849
Eexo-255D10	Eexo-A549D10	-331.06	89.0060	24	-3.72	0.0011*
Eexo-255D10	Eexo-A549D2.5	-514.15	89.0060	24	-5.78	<.0001*
Eexo-255D10	Eexo-A549D5	-369.01	89.0060	24	-4.15	0.0004*
Eexo-255D2.5	Eexo-255D5	17.1626	89.0060	24	0.19	0.8487
Eexo-255D2.5	Eexo-A549D10	-312.20	89.0060	24	-3.51	0.0018*
Eexo-255D2.5	Eexo-A549D2.5	-495.29	89.0060	24	-5.56	<.0001*
Eexo-255D2.5	Eexo-A549D5	-350.15	89.0060	24	-3.93	0.0006*
Eexo-255D5	Eexo-A549D10	-329.36	89.0060	24	-3.70	0.0011*
Eexo-255D5	Eexo-A549D2.5	-512.45	89.0060	24	-5.76	<.0001*
Eexo-255D5	Eexo-A549D5	-367.31	89.0060	24	-4.13	0.0004*
Eexo-A549D10	Eexo-A549D2.5	-183.09	89.0060	24	-2.06	0.0507
Eexo-A549D10	Eexo-A549D5	-37.9494	89.0060	24	-0.43	0.6736
Eexo-A549D2.5	Eexo-A549D5	145.14	89.0060	24	1.63	0.1160

Table 7. Differences of Treatments Least Squares Means (LSM) on K7M2 cells.

Treatment	Treatment	Estimate	Standard Error	DF	*t* Value	Pr > |t|
Control	Eexo-257-GdLD0.01	113.60	68.8146	24	1.65	0.1118
Control	Eexo-257-GdLD0.02	119.20	68.8146	24	1.73	0.0961
Control	Eexo-257-GdLD0.03	136.77	68.8146	24	1.99	0.0584
Control	Eexo-257D0.01	-180.51	68.8146	24	-2.62	0.0149*
Control	Eexo-257D0.02	106.08	68.8146	24	1.54	0.1363
Control	Eexo-257D0.03	71.1566	68.8146	24	1.03	0.3114
Eexo-257-GdLD0.01	Eexo-257-GdLD0.02	5.6066	68.8146	24	0.08	0.9357
Eexo-257-GdLD0.01	Eexo-257-GdLD0.03	23.1698	68.8146	24	0.34	0.7393
Eexo-257-GdLD0.01	Eexo-257D0.01	-294.11	68.8146	24	-4.27	0.0003*
Eexo-257-GdLD0.01	Eexo-257D0.02	-7.5136	68.8146	24	-0.11	0.9140
Eexo-257-GdLD0.01	Eexo-257D0.03	-42.4392	68.8146	24	-0.62	0.5432
Eexo-257-GdLD0.02	Eexo-257-GdLD0.03	17.5632	68.8146	24	0.26	0.8007
Eexo-257-GdLD0.02	Eexo-257D0.01	-299.72	68.8146	24	-4.36	0.0002*
Eexo-257-GdLD0.02	Eexo-257D0.02	-13.1202	68.8146	24	-0.19	0.8504
Eexo-257-GdLD0.02	Eexo-257D0.03	-48.0458	68.8146	24	-0.70	0.4918
Eexo-257-GdLD0.03	Eexo-257D0.01	-317.28	68.8146	24	-4.61	0.0001*
Eexo-257-GdLD0.03	Eexo-257D0.02	-30.6834	68.8146	24	-0.45	0.6597
Eexo-257-GdLD0.03	Eexo-257D0.03	-65.6090	68.8146	24	-0.95	0.3499
Eexo-257D0.01	Eexo-257D0.02	286.60	68.8146	24	4.16	0.0003*
Eexo-257D0.01	Eexo-257D0.03	251.67	68.8146	24	3.66	0.0012*
Eexo-257D0.02	Eexo-257D0.03	-34.9256	68.8146	24	-0.51	0.6164

Table 8. Differences of Treatments Least Squares Means (LSM) on K7M2 cells.

Treatment	Treatment	Estimate	Standard Error	DF	*t* Value	Pr > |t|
Control	Eexo-293-GdLD0.01	-5.1030	111.86	24	-0.05	0.9640
Control	Eexo-293-GdLD0.02	-2.7540	111.86	24	-0.02	0.9806
Control	Eexo-293-GdLD0.03	141.18	111.86	24	1.26	0.2190
Control	Eexo-293-S2D0.01	-404.67	111.86	24	-3.62	0.0014*
Control	Eexo-293-S2D0.02	-92.1222	111.86	24	-0.82	0.4183
Control	Eexo-293-S2D0.03	-12.6126	111.86	24	-0.11	0.9112
Eexo-293-GdLD0.01	Eexo-293-GdLD0.02	2.3490	111.86	24	0.02	0.9834
Eexo-293-GdLD0.01	Eexo-293-GdLD0.03	146.29	111.86	24	1.31	0.2033
Eexo-293-GdLD0.01	Eexo-293-S2D0.01	-399.57	111.86	24	-3.57	0.0015*
Eexo-293-GdLD0.01	Eexo-293-S2D0.02	-87.0192	111.86	24	-0.78	0.4442
Eexo-293-GdLD0.01	Eexo-293-S2D0.03	-7.5096	111.86	24	-0.07	0.9470
Eexo-293-GdLD0.02	Eexo-293-GdLD0.03	143.94	111.86	24	1.29	0.2105
Eexo-293-GdLD0.02	Eexo-293-S2D0.01	-401.92	111.86	24	-3.59	0.0015*
Eexo-293-GdLD0.02	Eexo-293-S2D0.02	-89.3682	111.86	24	-0.80	0.4322
Eexo-293-GdLD0.02	Eexo-293-S2D0.03	-9.8586	111.86	24	-0.09	0.9305
Eexo-293-GdLD0.03	Eexo-293-S2D0.01	-545.86	111.86	24	-4.88	<.0001*
Eexo-293-GdLD0.03	Eexo-293-S2D0.02	-233.31	111.86	24	-2.09	0.0478*
Eexo-293-GdLD0.03	Eexo-293-S2D0.03	-153.80	111.86	24	-1.37	0.1819
Eexo-293-S2D0.01	Eexo-293-S2D0.02	312.55	111.86	24	2.79	0.0101*
Eexo-293-S2D0.01	Eexo-293-S2D0.03	392.06	111.86	24	3.50	0.0018*
Eexo-293-S2D0.02	Eexo-293-S2D0.03	79.5096	111.86	24	0.71	0.4841

Table 9. Differences of Treatments Least Squares Means (LSM) on MDA-231 cells.

Treatment	Treatment	Estimate	Standard Error	DF	*t* Value	Pr > |t|
Control	Eexo-257 LPSD10	51.3182	33.2716	24	1.54	0.1361
Control	Eexo-257 LPSD20	38.8702	33.2716	24	1.17	0.2542
Control	Eexo-257 LPSD30	17.9786	33.2716	24	0.54	0.5939
Control	Eexo-257 S2D10	-139.40	33.2716	24	-4.19	0.0003*
Control	Eexo-257 S2D20	-2.6782	33.2716	24	-0.08	0.9365
Control	Eexo-257 S2D30	-22.1372	33.2716	24	-0.67	0.5122
Eexo-257 LPSD10	Eexo-257 LPSD20	-12.4480	33.2716	24	-0.37	0.7116
Eexo-257 LPSD10	Eexo-257 LPSD30	-33.3396	33.2716	24	-1.00	0.3263
Eexo-257 LPSD10	Eexo-257 S2D10	-190.72	33.2716	24	-5.73	<.0001*
Eexo-257 LPSD10	Eexo-257 S2D20	-53.9964	33.2716	24	-1.62	0.1177
Eexo-257 LPSD10	Eexo-257 S2D30	-73.4554	33.2716	24	-2.21	0.0371*
Eexo-257 LPSD20	Eexo-257 LPSD30	-20.8916	33.2716	24	-0.63	0.5360
Eexo-257 LPSD20	Eexo-257 S2D10	-178.27	33.2716	24	-5.36	<.0001*
Eexo-257 LPSD20	Eexo-257 S2D20	-41.5484	33.2716	24	-1.25	0.2238
Eexo-257 LPSD20	Eexo-257 S2D30	-61.0074	33.2716	24	-1.83	0.0791
Eexo-257 LPSD30	Eexo-257 S2D10	-157.38	33.2716	24	-4.73	<.0001*
Eexo-257 LPSD30	Eexo-257 S2D20	-20.6568	33.2716	24	-0.62	0.5405
Eexo-257 LPSD30	Eexo-257 S2D30	-40.1158	33.2716	24	-1.21	0.2397
Eexo-257 S2D10	Eexo-257 S2D20	136.72	33.2716	24	4.11	0.0004*
Eexo-257 S2D10	Eexo-257 S2D30	117.26	33.2716	24	3.52	0.0017*
Eexo-257 S2D20	Eexo-257 S2D30	-19.4590	33.2716	24	-0.58	0.5641

Table 10. Differences of Treatments Least Squares Means (LSM) on MDA-231 cells.

Treatment	Treatment	Estimate	Standard Error	DF	*t* Value	Pr > |t|
Control	Eexo-257 PolyD10	-82.4590	46.8418	24	-1.76	0.0911
Control	Eexo-257 PolyD20	-157.18	46.8418	24	-3.36	0.0026*
Control	Eexo-257 PolyD30	-188.80	46.8418	24	-4.03	0.0005*
Control	Eexo-257 S2D10	-139.40	46.8418	24	-2.98	0.0066*
Control	Eexo-257 S2D20	-2.6782	46.8418	24	-0.06	0.9549
Control	Eexo-257 S2D30	-22.1372	46.8418	24	-0.47	0.6408
Eexo-257 PolyD10	Eexo-257 PolyD20	-74.7204	46.8418	24	-1.60	0.1238
Eexo-257 PolyD10	Eexo-257 PolyD30	-106.34	46.8418	24	-2.27	0.0325*
Eexo-257 PolyD10	Eexo-257 S2D10	-56.9426	46.8418	24	-1.22	0.2359
Eexo-257 PolyD10	Eexo-257 S2D20	79.7808	46.8418	24	1.70	0.1014
Eexo-257 PolyD10	Eexo-257 S2D30	60.3218	46.8418	24	1.29	0.2101
Eexo-257 PolyD20	Eexo-257 PolyD30	-31.6176	46.8418	24	-0.67	0.5061
Eexo-257 PolyD20	Eexo-257 S2D10	17.7778	46.8418	24	0.38	0.7076
Eexo-257 PolyD20	Eexo-257 S2D20	154.50	46.8418	24	3.30	0.0030*
Eexo-257 PolyD20	Eexo-257 S2D30	135.04	46.8418	24	2.88	0.0082*
Eexo-257 PolyD30	Eexo-257 S2D10	49.3954	46.8418	24	1.05	0.3021
Eexo-257 PolyD30	Eexo-257 S2D20	186.12	46.8418	24	3.97	0.0006*
Eexo-257 PolyD30	Eexo-257 S2D30	166.66	46.8418	24	3.56	0.0016*
Eexo-257 S2D10	Eexo-257 S2D20	136.72	46.8418	24	2.92	0.0075*
Eexo-257 S2D10	Eexo-257 S2D30	117.26	46.8418	24	2.50	0.0195*
Eexo-257 S2D20	Eexo-257 S2D30	-19.4590	46.8418	24	-0.42	0.6815

Table 11. Differences of Treatments Least Squares Means (LSM) on K7M2 cells.

Treatment	Treatment	Estimate	Standard Error	DF	*t* Value	Pr > |t|
Control	Eexo-257-INFgD0.01	1467.71	415.73	24	3.53	0.0017*
Control	Eexo-257-INFgD0.02	1939.87	415.73	24	4.67	<.0001*
Control	Eexo-257-INFgD0.03	1500.03	415.73	24	3.61	0.0014*
Control	Eexo-257-S2D0.01	-841.39	415.73	24	-2.02	0.0543
Control	Eexo-257-S2D0.02	722.47	415.73	24	1.74	0.0951*
Control	Eexo-257-S2D0.03	1390.12	415.73	24	3.34	0.0027*
Eexo-257-INFgD0.01	Eexo-257-INFgD0.02	472.16	415.73	24	1.14	0.2673
Eexo-257-INFgD0.01	Eexo-257-INFgD0.03	32.3204	415.73	24	0.08	0.9387
Eexo-257-INFgD0.01	Eexo-257-S2D0.01	-2309.10	415.73	24	-5.55	<.0001*
Eexo-257-INFgD0.01	Eexo-257-S2D0.02	-745.24	415.73	24	-1.79	0.0856
Eexo-257-INFgD0.01	Eexo-257-S2D0.03	-77.5920	415.73	24	-0.19	0.8535
Eexo-257-INFgD0.02	Eexo-257-INFgD0.03	-439.84	415.73	24	-1.06	0.3006
Eexo-257-INFgD0.02	Eexo-257-S2D0.01	-2781.26	415.73	24	-6.69	<.0001*
Eexo-257-INFgD0.02	Eexo-257-S2D0.02	-1217.40	415.73	24	-2.93	0.0074*
Eexo-257-INFgD0.02	Eexo-257-S2D0.03	-549.75	415.73	24	-1.32	0.1985
Eexo-257-INFgD0.03	Eexo-257-S2D0.01	-2341.42	415.73	24	-5.63	<.0001*
Eexo-257-INFgD0.03	Eexo-257-S2D0.02	-777.56	415.73	24	-1.87	0.0737
Eexo-257-INFgD0.03	Eexo-257-S2D0.03	-109.91	415.73	24	-0.26	0.7937
Eexo-257-S2D0.01	Eexo-257-S2D0.02	1563.86	415.73	24	3.76	0.0010*
Eexo-257-S2D0.01	Eexo-257-S2D0.03	2231.51	415.73	24	5.37	<.0001*
Eexo-257-S2D0.02	Eexo-257-S2D0.03	667.65	415.73	24	1.61	0.1214

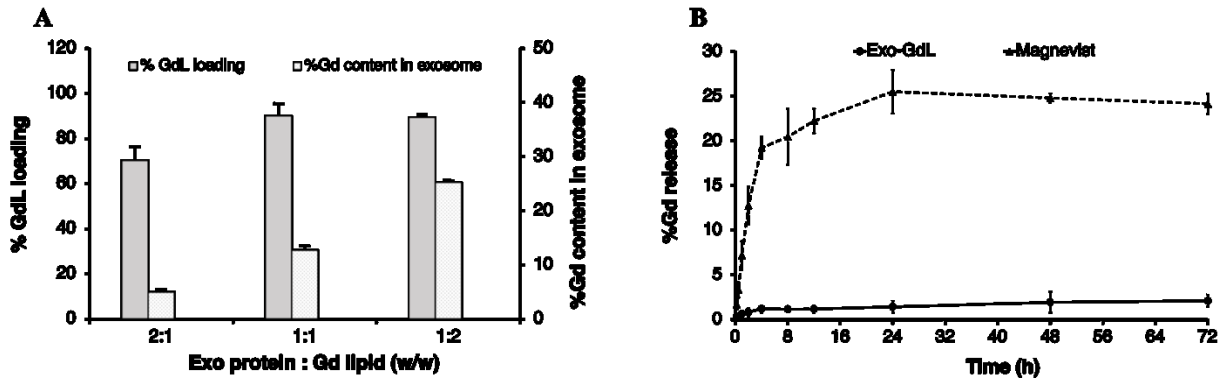

Figure 20. Gadolinium loading and release studies. (A) Gadolinium (Gd^{3+}) loading efficiency with different initial input concentrations of Gadolinium lipid (GdL, 500, 1000 and 2000 μg/ml). (B) The cumulative Gd^{3+} release profile of Magnevist® and gadolinium labeled exosomes (Exo-GdL) at physiological conditions (pH: 7.4 at 37 ºC). All Gd^{3+} concentration was quantified by inductively couple plasma mass spectrometry (ICP-MS). Notice that gadolinium labeled exosomes showed less than 3% loss of Gd^{3+} over 72 hours. In contrast, the MRI contrast agent, Magnevist, was less stable and lost about 20 % of the labeling in 4 hours. Data represented as mean ± 1 standard deviation. (n = 3).

3.2.2.2. Gadolinium loading and release studies.

To optimize the gadolinium labelling capability onto exosome membrane, the GdL insertion of several w/w ratios of Exo protein and GdL were evaluated (figure 17A). The labelling efficiency peaked at 25 % GdL per 1 mg exosome protein, and 90 % GdL inserted into exosome lipid bilayer compared to the initial GdL input. Even though formulation with Exo protein/GdL ratio of 1:2 showed the highest labelling efficiency, the formulation became unstable and aggregated owing to

the disruption in the structural integrity of exosome during GdL insertion. Therefore, the Exo/GdL ratio of 1:1 was used in the remaining experiments.

To confirm the stability of the contrast agent after labeling exosomes, a GdL release study was conducted (figure 17B). The selected formulation of Exo-GdL released less than 2 % in a period of 72 hours under dialysis conditions, whereas Magnevist® display a burst release in the first 4 hours. The gadolinium ion released from Magnevist® was 5 times higher than that of Exo-GdL at the end of experimental time.

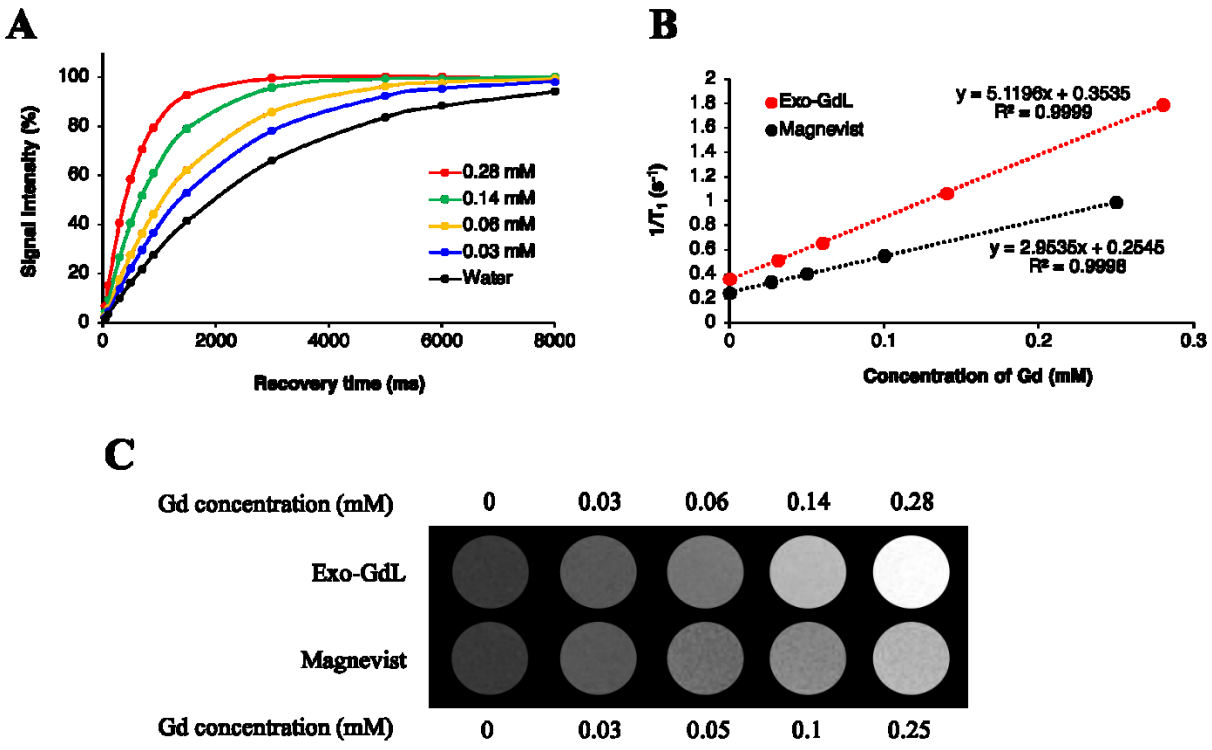

Figure 21. Magnetic property studies. (A) T1 recovery curve of gadolinium labeled exosomes (Exo-GdL) at different concentrations of gadolinium (Gd). (B) The plot of 1/T1 vs. the concentration of the contrast agent in aqueous solution measured in a 14.1T magnetic resonance

imaging (MRI) system at 37 ºC. Longitudinal relaxivity (r1) of Exo-GdL and Magnevist® is 5.1 and 2.9 mM-1s-1, respectively. (C) T1-weight imaging Exo-GdL and Magnevist® at different concentration in aqueous solution measured in a 14.1T MRI system.

3.2.2.3. Magnetic property studies.

To further investigate the effect of GdL-Exo on MR relaxivity, a serial dilution of Exo-GdL was carried out to obtain different Gd concentration and Magnevist® with similar Gd concentration was used as control (figure 18). The resulting diluted samples were subjected to T_1 measurement using a Bruker 600 MHz (14.1 T) Advance III with microimaging capability. The magnetic properties of Exo-GdL and Magnevist were first investigated by measuring the signal intensity of water protons with recovery time (TR) varying from 0 to 8000 ms at a constant echo time (TE) of 6.5 ms to obtain T_1 relaxation time (Figure 18A). These T_1 relaxation times were converted to s^{-1} ($1/T_1$) and plotted against Gd concentration in mM. The longitudinal relaxation rates of both Exo-GdL and Magnevist® exhibited a linear relationship with respect to gadolinium concentration with the coefficient factor (R^2) greater than 0.999. The slope of obtained linear equation depicted the r_1 relaxivity ($s^{-1}mM^{-1}$) of gadolinium in each formulation. These results show that the Exo-GdL exhibit a r_1 of 5.1 s^{-1} mM^{-1} while the Magnevist® control show a r_1 of 2.9 s^{-1} mM^{-1}. The higher r_1 relaxivity of Exo-GdL is probably due to the reduction in tumbling rate upon GdL insertion into exosomal membrane leading to the increasing of relaxivity [155]. The brighter effect in MRI contrast was also depicted by T_1-weighted images of different Exo-GdL and Magnevist® concentration; water was used as a control. These results demonstrated that Exo-GdL always showed a brighter contrast than Magnevist® samples at the same gadolinium concentration as presented in figure 18C.

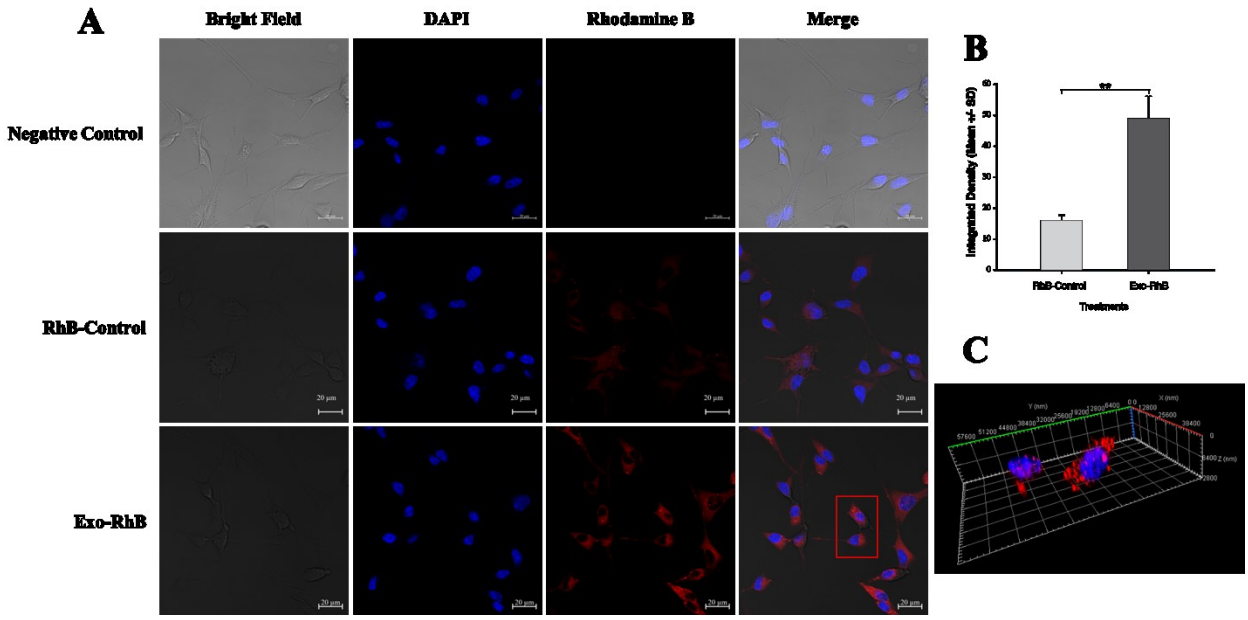

Figure 22. Exosomes are taken into osteosarcoma cells in vitro confocal microscopy. Mesenchymal stroma cell (MSC)-derived exosomes that were labeled with Rhodamine-B were visualized by confocal microscopy entering murine osteosarcoma cells (line K7M2). K7M2 cells were seeded at 104/cm2 in 8-well chambered coverglass and incubated for 24 hours at 37 ºC and 5 % CO2. Rhodamine B-labeled MSC-exosomes (Exo-RhB) were made by mixing exosomes with Rhodamine-B at a 50:1 ratio (Exo:RhB). The cells were exposed to 25 µg of Exo-RhB and incubated for an additional 24 h. RhB-lipid or DPBS were used as controls. The cells were fixed with paraformaldehyde /glutaraldehyde solution and stained with 4',6-diamino-2-phenylindole (DAPI) prior to visualization. (A) Confocal microscopy images show exosomes enter cell cytoplasm, not the nucleus. (B) Integrated density of Exo-RhB and RhB-control shows significantly higher fluorescent signal in the Exo-RhB exposed cells compared to the RhB-lipid control. (C) 3D visualization of exosome uptake shows that Exo-RhB were within the cytoplasm

and not on the surface of the osteosarcoma cells. The red rectangle in figure 5A indicates the cells on figure 5C. Data showing mean ± 1 SD, n = 3. ** $p < 0.01$.

3.2.2.4. Exosomes are taken into osteosarcoma cells *in vitro*

Exosomes derived from HUC-MSCs have been studied as a therapeutic agent due to their anti-proliferative and pro-apoptotic effect [156]. Lee *et al*. reported that MSC-derived exosomes reduce the expression of vascular endothelial growth factor (VEGF) through the release of miR-16, leading to the reduction of angiogenesis in breast cancer model *in vivo* and *in vitro* [157]. To investigate the interaction of HUC-MSC exosomes with cancer cells, the cellular uptake of exosomes in osteosarcoma cells (K7M2) was investigated using exosomes labeled with rhodamine B (Exo-RhB) using lipid insertion protocol. Thereafter, the Exo-RhB was incubated with cells for 24 h, and the internalization of exosomes was analyzed by confocal microscopy (figure 19). The RhB-labeled liposomes were used as a control particle (control-RhB). As shown in figure 19B, the fluorescence intensity of the Exo-RhB (48.85 ± 6.97) was significantly higher than that of control-RhB nanoparticle (16.05 ± 1.48, $p < 0.05$). The 3D image of the cells revealed that the exosomes were internalized into the cell and located in the cytoplasm and not non-specifically distributed on the cell surface or within the nucleus. This observation indicates that Exo-RhB were taken up by K7M2 cells (figure 19C). To further evaluate the effect of time on the exosomes uptake, flow cytometry was used to assess their uptake in K7M2 cells at 6, 12, 24 and 48 hours ours of incubation with Exo-RhB under standard conditions. After the incubation time, cells were rinsed three times in DPBS and then evaluated by flow cytometry (figure 20A). The result show that exosome uptake by K7M2 cells is time-dependent over the 6 to 24 hours observation period (data

summarized in figure 20B). The maximum uptake (40 %) was reached after 24 hours of incubation; there were not additional labeling after 24 hours.

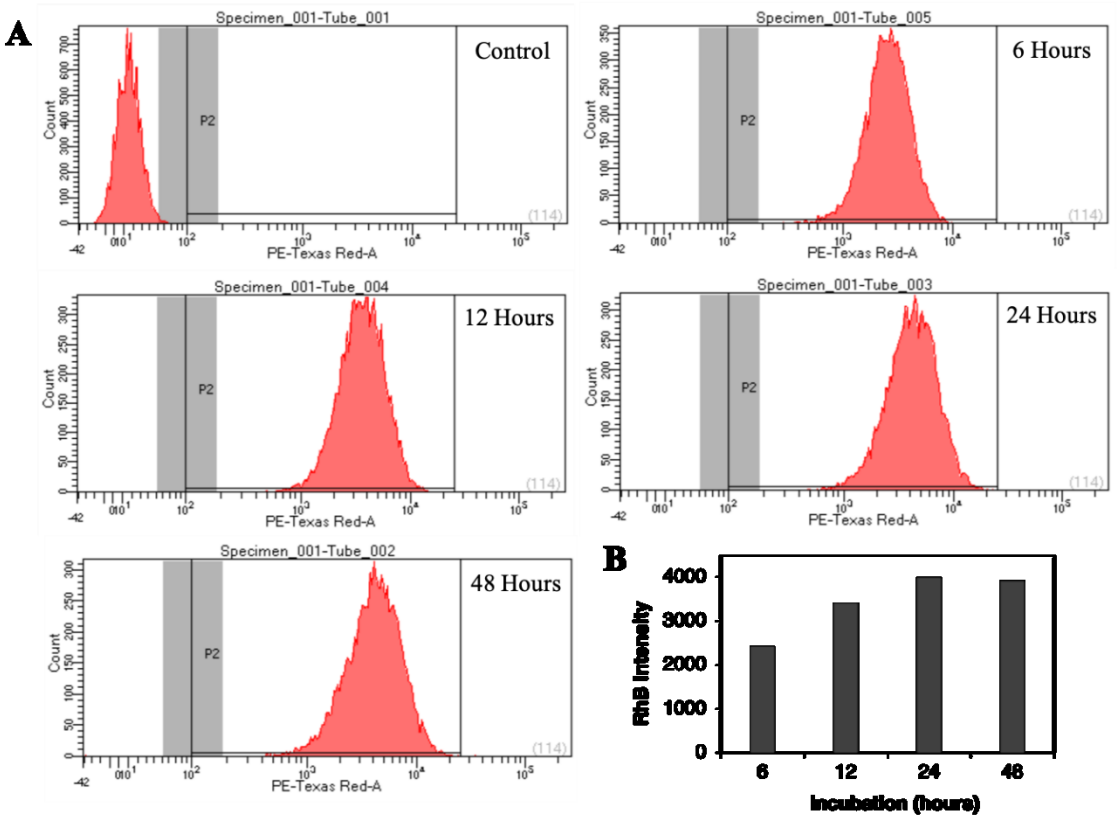

Figure 23. Cell uptake by flow cytometry. Mouse osteosarcoma cells (line K7M2) were incubated with Rhodamine-B labeled exosomes (Exo-RhB) to examine the time-dependent exosome uptake. (A) Representative flow cytometry histograms demonstrating fluorescence in K7M2 cells incubated with naive mesenchymal stromal cell- (MSC) derived exosomes (unlabeled control, derived from MSC line HUC 257), or with Exo-RhB for 6, 12, 24, and 48 hours . (B) Fluorescence intensity of Exo-RhB after 6, 12, 24 and 48 hours of incubation. Notice that about 2/3rds of the fluorescence is taken up in the first 6 hours ours, but fluorescence intensity increases for the first 24 hours.

3.2.2.5. Effect of exosomes on osteosarcoma cell proliferation *in vitro*.

The effect of exosomes and of Exo-GdL on cancer cell proliferation was evaluated using the MTT assay. As was mention before, there is a concern about the implementation of GdL as contrast medium because of its potential toxicity, even if the metal is chelated. For that reason, in this assay, the effect of GdL or RhB labeling into exosomes on cell proliferation was investigated. K7M2 and 143B cells were seeded in 96-well plate format in five independent replicates. The cells culture were treated for 24 hours with 10, 20 and 30 ng per well of naive exosomes, Exo-GdL or exosomes double-labeled with both GdL and RhB (Exo-GdL-RhB). As shown in figure 21, both K7M2 and 143B cell lines exhibit higher proliferation when exposed to naive exosomes at 10 ng, compared with the controls. As the concentration of naive exosome increases, a dose-dependent reduction on the proliferation was observed for both cancer cell lines.

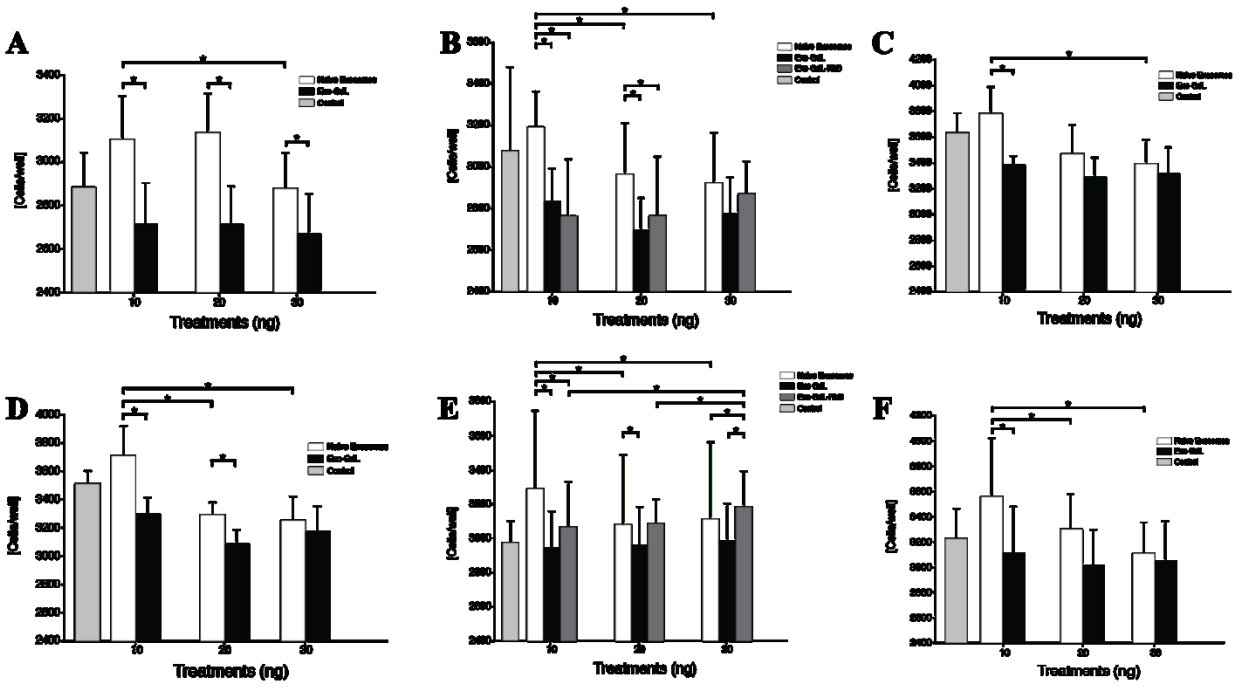

Figure 24. Effect of exosomes on osteosarcoma cell proliferation *in vitro*.A, B and C. Mouse osteosarcoma cells (line K7M2) treated with 10, 20 and 30 ng of naive-exosomes or gadolinium-labeled exosomes (Exo-GdL) per well. Note in A, B, and C, that naive exosomes enhanced K7M2 growth compared to control at the lowest dose (not indicated on graph), and Exo-GdL inhibited K7M2 growth more than naive exosomes. Note in B, exosomes labeled with both GdL and Rhodamine-B (Exo-GdL-RhB) were included for comparison. Both Exo-GdL and Exo-GdL-RhB inhibited K7M2 growth in a dose-dependent fashion. D, E and F. Human osteosarcoma cells (line 143B) treated with 10, 20 and 30 ng of exosomes per well. Note in D, E and F, that naive exosomes enhanced 143B growth at the lowest dose (not indicated on graph), and Exo-GdL inhibited 143B growth compared to naive exosomes. Note in E, exosomes labeled with both GdL and Rhodamine-B (Exo-GdL-RhB) were included for comparison. Both Exo-GdL and Exo-GdL-RhB showed a dose-dependent effect on 143B growth. There were subtle differences in the 143B growth effects between Exo-GdL and Exo-GdL-RhB. (C) Exosomes isolated from mesenchymal stromal cell

(MSC) line 1 (HUC-257). (F) Exosomes isolated from MSC line 2 (HUC-293). Note in C and F, exosomes batches MSC line 1 or line 2 produced similar, dose-dependent effects on osteosarcoma proliferation. 10 µl of DMEM was used as control. Cell proliferation was measured using an 3-(4,5-dimethylthiazol-2-yl)-2,5-diphenyltetrazolium bromide (MTT) assay. Data are presented as mean ± 1 standard deviation, * = $p < 0.05$, n = 5.

Specifically, in K7M2 cells, naive exosomes showed a significantly enhanced proliferative effect at 10ng (3103.90 ± 175.41 cell/well) and 20 ng (3136.27 ± 168.18). However, when the concentration of exosome increased up to 30 ng, the number of cells dropped from 3136.27 ± 175.41 to 2879.64 ± 93.75 cells/well. Similar results were found in 143B cells, where the number for naive exosomes at 10 ng (3710.93 ± 212.72 cells/well) was higher than the control (3513.36 ± 89.75), but the number of cells significantly fell and became lower than the number of control cells as the treatment concentration reached to 20 ng (3294.92 ± 113.74) and 30 ng (3254.60 ± 176.95), showing the dose-dependent inhibition of proliferation. On the other hand, cells treated with Exo-GdL exhibited an inhibitory effect on proliferation (2967.9 8± 213.46 cells/well) compared with the control, regardless of the Exo-GdL concentration (Figure 21A). In addition, the effect of double-labeled (GdL and RhB) exosomes was investigated on both cell lines. These results showed that K7M2 exhibited the same response obtained from the single labeling (Exo-GdL). However, in the case of 143B, there was a proliferative effect at 10 ng (3071.16 ± 260.58 cells/well), 20 ng (3086.97 ± 138.48), and 30ng (3184.30 ± 206.02) compared with the control (2975.41 ± 121.42). Interestedly, the double-labeled exosomes show a proliferative effect in a dose-dependent manner (figure 21E). Finally, the effects of exosomes prepared from different HUC lines mediated similar responses in both human and mouse osteosarcoma cells. For this purpose, exosomes from HUC-

257 and HUC-293 were isolated under the identical experimental conditions. As expected, the proliferation of cancer cell lines exhibit the same trend in response to Exos derived two different HUC cell lines (figure 21C, F). Similar results were found by Alarifi *et al*. in SH-SY5Y human neuroblastoma cells with gadolinium oxide nanoparticles (GNPs) where the cell viability was significantly reduced in a time and dose dependent manner after 24 and 48 hours ours [158].

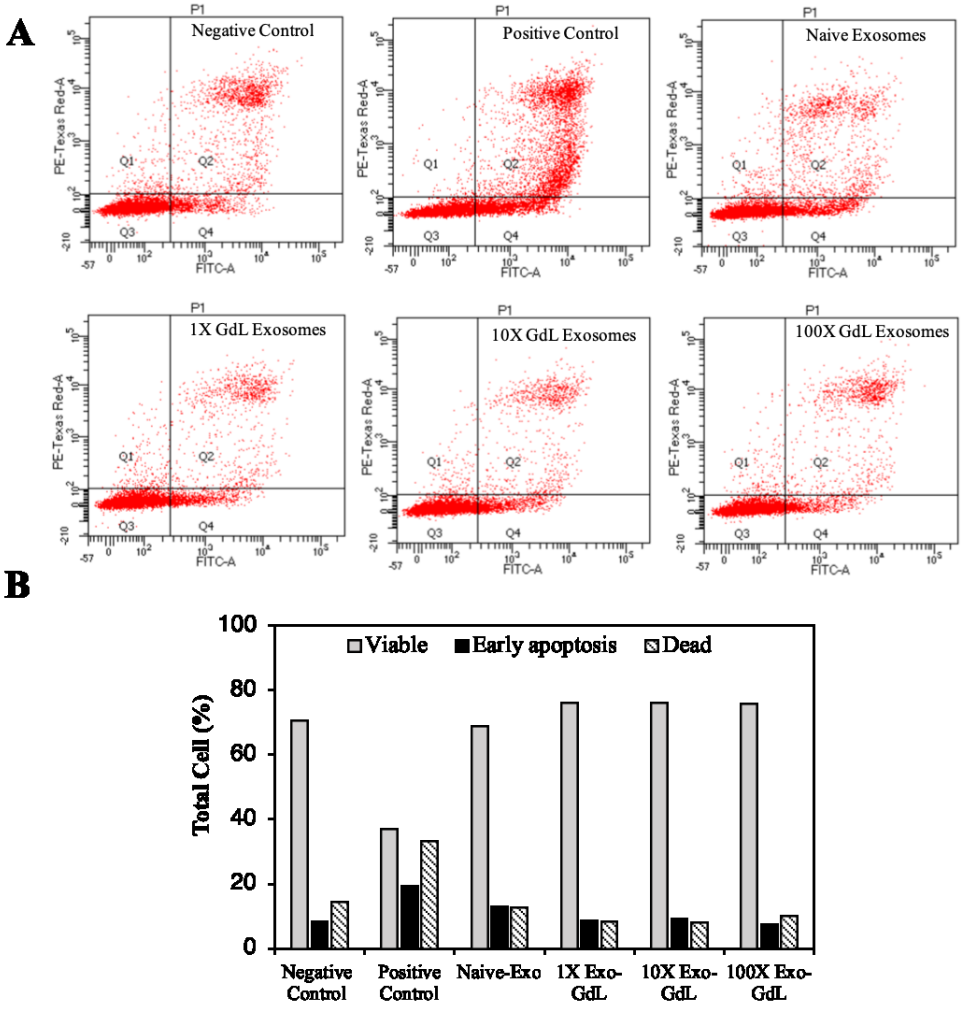

Figure 25. Effect of gadolinium labeled exosomes (Exo-GdL) on apoptosis in mouse osteosarcoma cells (line K7M2). Mouse osteosarcoma cells were treated with 30 ng/cm2 (1X) of

naive exosomes (Naive-Exo) or different concentrations of gadolinium-labeled exosomes (Exo-GdL, 1 ×, 10 × and 100 ×) suspended in 1 ml of DMEM supplemented with 10% human platelet lysate (HPL) depleted of exosomes. 1ml of the same culture media was used as negative control (Negative Control) and 500 μM of hydrogen peroxide (H2O2) was used as a positive control (Positive Control). Osteosarcoma cells were stained with Annexin-V FITC and propidium iodide (PI) and analyzed by flow cytometry. (A) Representative dot plots of Annexin-V (x-axis) vs. PI (y axis) stained cells: quadrant 2 (Q2) corresponds to dead cells, Q3 Viable cells and Q4 cells in early apoptosis. (B) Percentage of viable (gray bar), early apoptosis (black bar) or dead cells (hash line) under different treatments after 24 hours of incubation under standard conditions. Note that the positive control (peroxide treatment) increased cell death and early apoptosis in K7M2 cells, as expected. In contrast, cell death and early apoptosis were not affected by either naive-Exo and Exo-GdL exposed K7M2 cells, even when the exosome "dose" was 100 ×.

3.2.2.6. Effect of gadolinium labeled exosomes (Exo-GdL) on apoptosis in mouse K7M2 osteosarcoma cells.

Since exosome exposure decreased the proliferation of cancer cells, we investigated whether that reduction was accompanied by activation of apoptosis, as indicated by Annexin V staining. To assess apoptosis, K7M2 osteosarcoma cells were treated with 30 ng/cm^2 (1 ×) of naive-Ex or 10 × and 100 × of Exo-GdL. The cells were incubated for 24 hours with the treatments and then stained with Annexin V and PI. The results of this assay can be interpreted depending on the intensity of the Annexin V and PI. Cells with the negative signal of Annexin V and PI are healthy "normal" cells. Cells with positive signal of Annexin V are considered to be in early apoptosis. Cells that are positive for both markers Annexin V and PI are considered to be necrotic. The kit

implemented in this experiment does not discriminate cells that are only positive for PI. Figure 8A shows the representative dot plot of the forward and side scatter for K7M2 cells after 24 hours of incubation with the treatments. There were no appreciable differences in the percentage of apoptotic cells between the 1 × naive exosomes (12.8 %), 10 × Exo-GdL (9.3 %), 100X Exo-GdL and the negative control (8.2 %), whereas the 500 μM H_2O_2 positive control treatment reaches a maximum of 19.4 % of apoptotic cells (and more necrotic cells, too) (figure 22).

Additionally, apoptosis was investigated using confocal microscopy to gain a better understanding of the cell's status. Cells were seeded under the same conditions in 1cm^2 8-well chambered cover glass and underwent the same treatment protocol. After the incubation time, cells were fixed with paraformaldehyde /glutaraldehyde solution and observed. Annexin V/FITC was excited with a wavelength of 530 nm and PI with 630 nm. As shown in figure 23, Annexin V signal (depicted by the green fluorescence) in the cell membrane and PI signal exhibits (bright red fluorescence) in the nucleus. In principle, this assay relies on the binding ability of Annexin V to Phosphatidylinositol and intercalation of PI into DNA molecules. When cells become apoptotic, the cell membrane become destablized, thereby, exposing the phosphatidylinositol to the outer leaflet of the cell membrane, which in normal conditions is facing the cytoplasm.

On the other hand, PI is a fluorescent dye that intercalates into DNA, but it's not permeable to the plasma membrane [159]. This method of apoptosis detection responds more to the mechanic properties of the membrane rather than determine the activation of apoptotic pathways. In summary of our observations, exosomes reduce cell proliferation in human and mouse osteosarcoma cell lines without an effect on apoptosis. Experiments targeting the metabolic pathways of apoptosis such as caspases should be considered in the future to better delineate the mechanism of exosome's action on cancer cells.

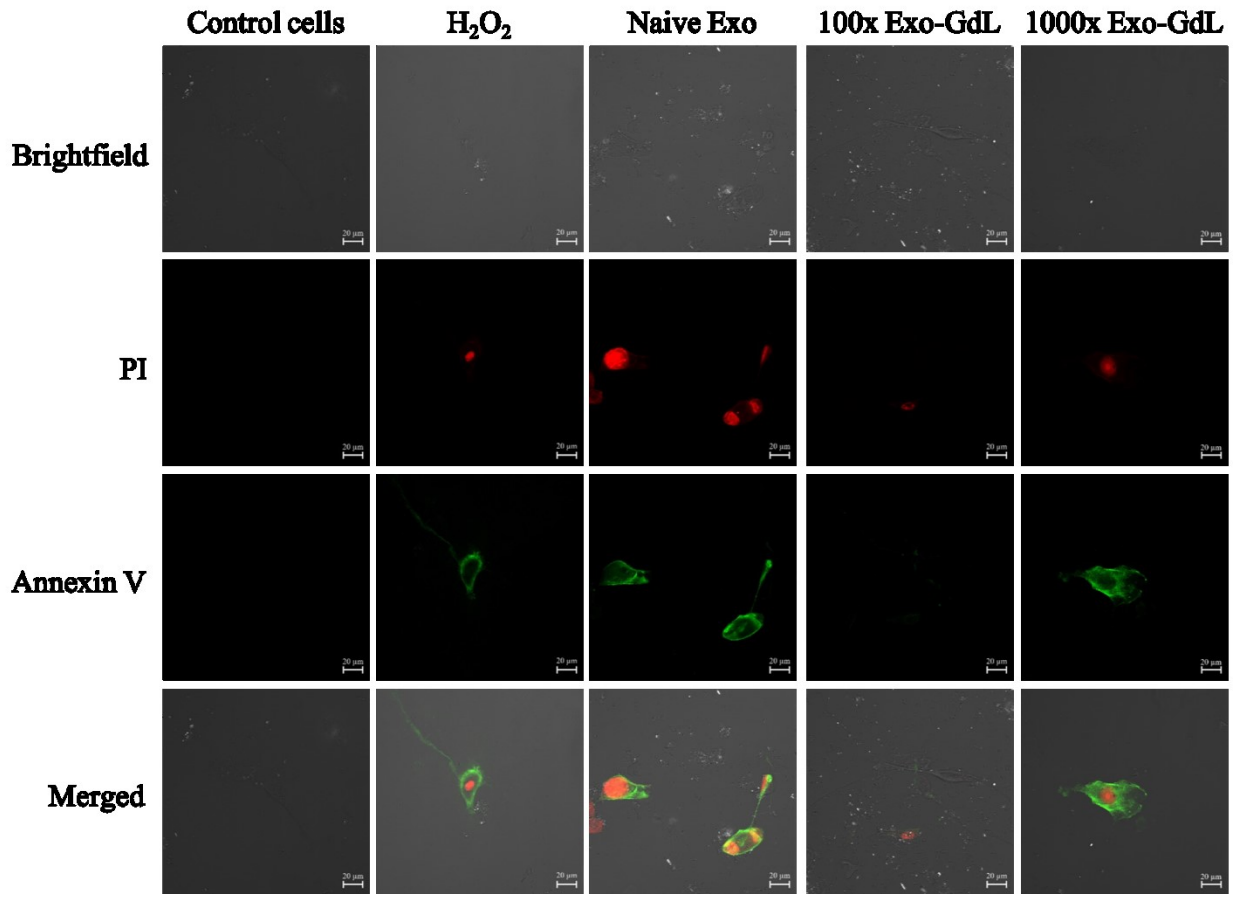

Figure 26. Effect of exosomes on mouse osteosarcoma cells (line K7M2) apoptosis.The osteosarcoma cultures were exposed to 30 ng/cm2 (1×) of naive exosomes (Naive Exo) or 100 × and 1000 × gadolinium labeled exosomes (Exo-GdL), suspended in 1 ml of DMEM 10% human platelet lysate depleted of exosomes. The cells were incubated for 24 hours and observed under confocal microscopy for early apoptosis as indicated by Annexin V staining. 1ml of the same culture media was used as negative control and 500 µM of hydrogen peroxide (H_2O_2) was used as a positive control. Cells were stained with Annexin-V FITC (green) and propidium iodide (PI, red). Double-negative = healthy cells (no staining), Annexin V-positive early apoptosis (green), double-positive = necrotic cells (green/red). Note that in the naive Exo-panels, one K7M2 cell in

the lower right part of the panel is undergoing cytokinesis and is staining with Annexin V. Calibration bar is 20 micrometers.

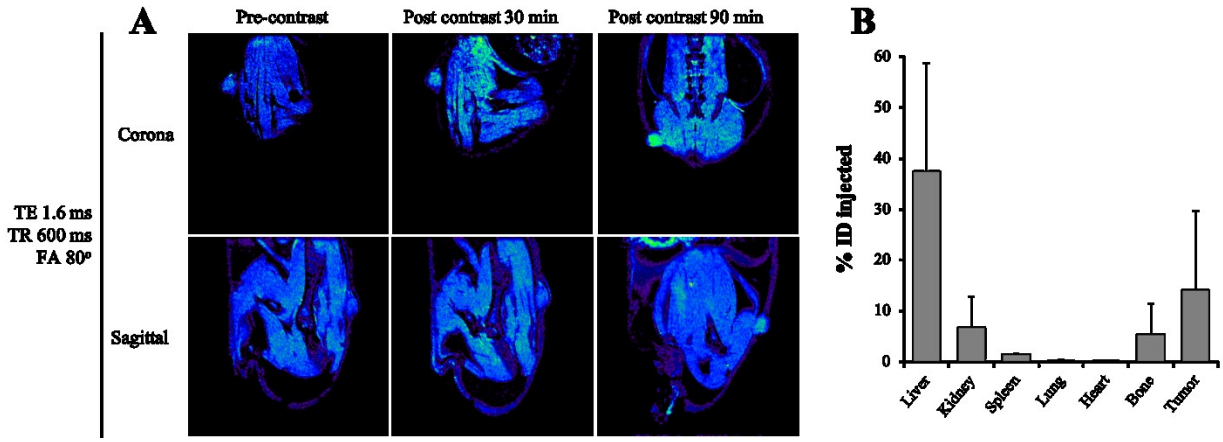

Figure 27. Biodistribution of gadolinium labeled exosomes (Exo-GdL) in an ectopic mouse osteosarcoma tumor model.(A) Representative 14.1 tesla magnetic resonance (MR) images of mouse osteosarcoma tumor (line K7M2) bearing mice demonstrating enhancement of positive contrast at tumor site after 30 min and 90 min post injection. The images were taken at echo time (TE) of 1.6 ms, repetition time (TR) of 600 ms, and flip angle (FA) of 80º. (B) Biodistribution of Exo-GdL in the major organs of K7M2 tumor bearing mice 24 hours after injection. Exo-GdL was injected intravenously via the tail vein. After 24 hours, the mouse was humanely sacrificed and the major organs were collected, digested with concentrated HNO_3, and GdL content was measured using inductively coupled plasma mass spectrometry (ICP-MS) analysis. Note that 38% of the GdL was within the liver and 18% was in the tumor. Data showing mean ± 1 standard deviation, n=3.

3.2.3. *In vivo* detection of Exo-GdL by MRI.

To prove the applicability of the Exo-GdL for imaging purposes, K7M2 cells were implanted into NU/NU nude mice. After 15 days to permit tumor development, Exo-GdL were intravenously injected into the mice. Images were acquired under the established protocol with pre- and post-contrast at 30 and 90 min. Figure 24A shows representative sagittal and coronal views taken through the tumor level at TE = 1.6ms, TR = 600 ms and FA = 80º. The signal intensity in the tumor increased in a time-dependent manner. After 90 min post-injection, the tumor became brighter and clearly distinguishable from the surrounding tissue due to the accumulation of Exo-GdL. To further evaluate *in vivo* behavior of Exo-GdL, the biodistribution of Exo-GdL was evaluated 24 hours after injection. For this experiment, liver, kidney, spleen, lung, heart, bone and tumor were individually collected, digested and subjected to Inductively Coupled Plasma Mass Spectrometry (ICP-MS) to quantify their Gd content. As shown in figure 24B, Exo-GdL accumulated in liver (38 %), kidney (8 %) and spleen (2 %), the main excretion organs responsible for elimination of small molecules and nanosized material [160, 161]. Interestingly, the accumulation of Exo-GdL was high in tumor, reaching 18 %. It is noteworthy that Magnevist® is small molecule magnet whereas Exo-GdL is a nanoparticulate system [162, 163].

To further examine the versatility in surface modification and confirm the accumulation in tumor exhibited by exosomes labeled with GdL, we compared exosomes labeled with a near infra-red dye (DiR), or PEGylated NPs labeled with DiR, (PEGNP-DiR) and tracked their distribution in 3 NU/NU K7M2-tumor bearing mice following intravenous injection. As shown in figure 25A, Exo-DiR and PEGNP-DiR predominantly accumulated in liver, which is similar to the observation obtained following Exo-GdL distribution. However, the distributed signal intensity of Exo-DiR in

liver and spleen was two-fold higher than that of PEGNP-DiR even after 48 hours ours of injection, presumably due to the longer circulation time of exosome (figure 24B).

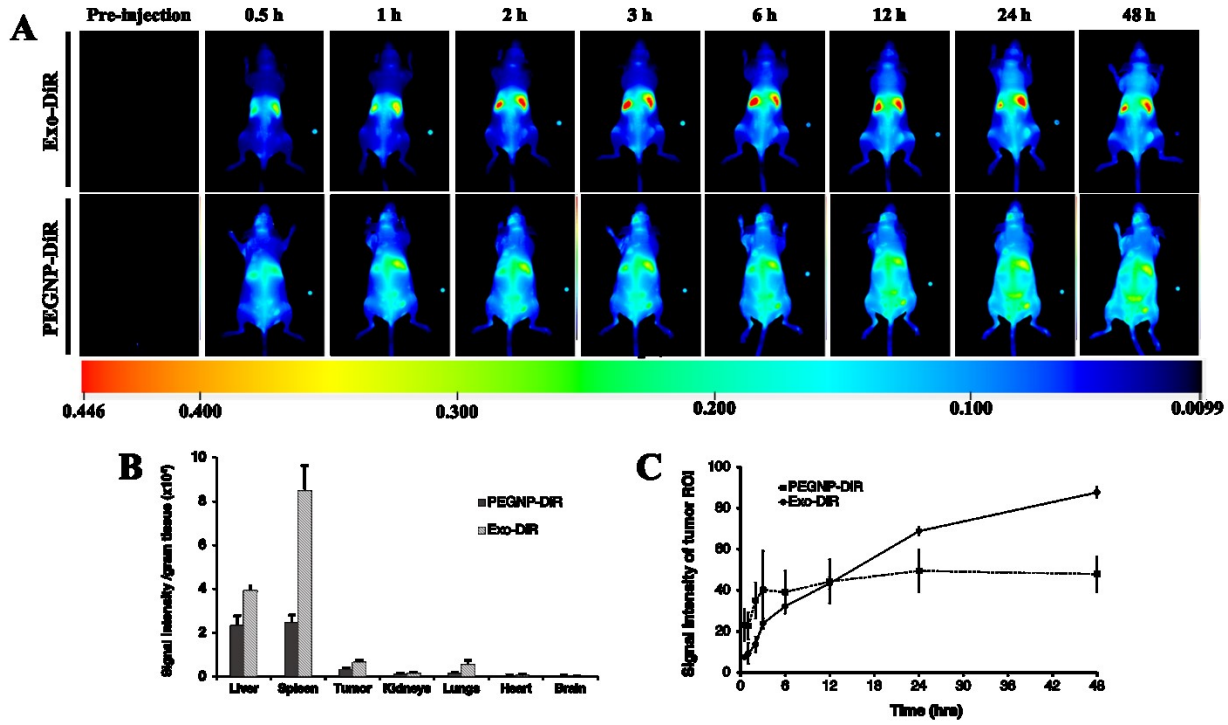

Figure 28. Biodistribution of near infrared dye (DiR) labeled exosomes in an ectopic mouse osteosarcoma tumor model.(A) Time-dependent biodistribution of fluorescence in mice pre- and post-intravenous injection with near infrared dye labeled exosomes (Exo-DiR, Exosome) or polyethylene glycol nanoparticle labeled with near infrared dye (PEGNP-DiR, Control nanoparticle) visualized with fluorescent bioimaging. (B) Forty-eight h after injection, the mice were humanely sacrificed and the major organs were dissected. The fluorescent signal intensity per gram of tissue in mouse organs and tumor was measured. Note that the highest signal intensity was found in liver and spleen. The label in spleen was roughly double that of liver. The next most intense signal was in tumor. (C) Signal intensity of Exo-DiR or PEGNP-DiR in mouse tumors 48

hours after intravenous injection. Note that the signal intensity in tumor accumulates over 48 hours for Exo-DiR, in comparison to the control (PEGNP-DiR), the signal intensity peaks about 3 after injection. Note that in A, each image contains a small fluorescent phantom for calibration on the lower right. Data are presented as the mean ± 1 standard deviation. n = 3.

We further evaluated the accumulation of particles in the tumor over the time by extracting signal intensity from a region of interest (ROI) in the tumor. The result shows that even though the fluorescence intensity in the tumors of the Exo-DiR mice increases slower than PEGNP-DiR mice in the first 3-12 hours post injection, the accumulation of exosomes dramatically increased over the next 12 hours after injection. In the case of PEGNP-DiR injected mice, the signal intensity did not increase after 3 following injection, implying the excretion process of PEGNP-DiR had been taken placed. On the other hand, signal intensity in tumors of Exo-DiR treated mice continued to increase throughout the 48 hours observation period (figure 25C), indicating the accumulation of exosomes. At 48 hours following injection, signal intensity in the tumor of Exo-DiR mice reached twice the accumulation of the PEGNP-DiR-treated mice. In contrast to the accumulation of 18% of the GdL labeled exosomes in the tumor in 24 hours and the second highest concentration next to that of liver, the exosomes labeled with DiR had less accumulated signal in the tumor. The signal intensity of tumors from both treatments (Exo-DiR and PEGNP-DiR) were also compared. The signal intensity of tumors treated with the Exo-DiR (1185.84 ± 247) was twice that obtained with PEGNP-DiR (576.70 ± 146), which strongly supports the dynamic signal intensity data (figure 26). This result confirms that HUC-MSC exosomes remain effective and biologically active and continue to accumulate in mouse tumors for at least 48 hours after injection.

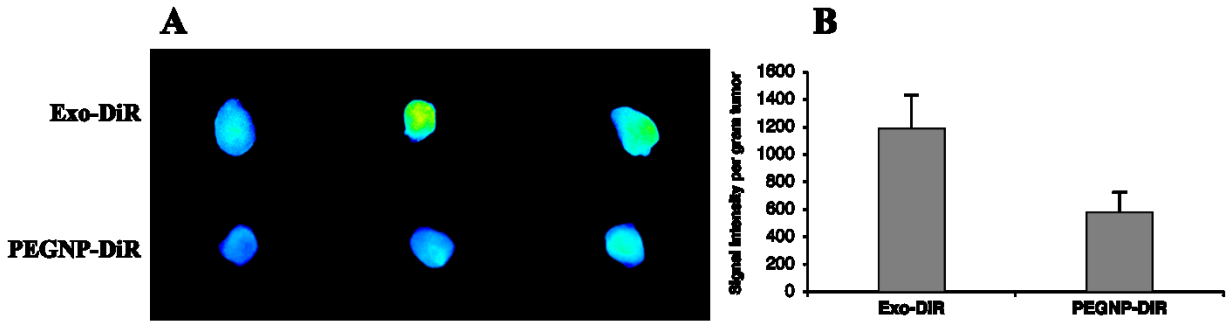

Figure 29. DiR fluorescence of the K7M2 tumors.(A) Fluorescent bioimaging of mouse osteosarcoma tumors by Exo-DiR (Exosome) or PEGNP-DiR (Control NPs) 48 hours after intravenous injection. (B) Quantitative signal intensity per gram tumor demonstrates the efficient tumor targeting properties of exosomes over control nanoparticles. Data is shown as mean ± SD, n = 3.

4. Discussion

We adapted an efficient protocol for exosomes from HUC-MSCs isolation by sequential ultracentrifugation, obtaining high-quality exosomes that exhibit the characteristic tetraspanin membrane markers, while retaining high isolation yields. The isolated exosomes were further labeled with GdL or DiR, singly, or double-labeled with both GdL and DiR, using the newly developed lipid insertion technique. Similar to other heavy metals, one of the major limitations of using gadolinium as a contrast agent in the clinic is the toxicity associated with its free ion form. In fact, there are reported cases of nephrogenic systemic fibrosis (NSF) related to the use of gadolinium in patients with renal dysfunction [164]. In order to avoid potential toxic effects, gadolinium was stabilized with a cyclic macromolecule DOTA, which has been demonstrated to be more stable than other linear macromolecules such as DTPA [165]. This result suggested that the selected Exo-GdL formulation was safe for use *in vitro* and *in vivo* studies (figure 3B). These labeled exosomes accumulated both in vitro in human and mouse osteosarcoma cells and in the tumors of an osteosarcoma mouse model over a 48 hours period compared with PEGylated nanoparticles which accumulated over a 3 period.

The outstanding performance of exosome in biological environment can be explained by its biological origin. When the synthetic material is introduced into a biological environment, it has to overcome multiple barriers in order to produce a response [132]. As a consequence, the majority of the synthetic nanoparticles will be eliminated before reaching the site of action, thereby the nanoparticle accumulation in tumors is low. In the case of exosomes, owing to their biological origin, they can circulate throughout the system without signs of adverse effects and then traffic to the tumor [166]. In addition, the accumulation of exosomes in tumors, as occurs with other nanomaterials, can be explained by the enhanced permeability and retention (EPR) effect where

the lack of lymphatic drainage as well as the disorganized architecture of the tumor vascular system, which promote the accumulation of macromolecules and nanosize material at the tumor [167]. All of these factors presumably are contributing to the extensive accumulation of exosomes in this present study.

Qi *et al*. showed that exosomes isolated from blood accumulate in the tumors of H22-tumor bearing mice [74]. Similar results were reported in a C57Bl/6 mice model of metastatic lung cancer, where paclitaxel-loaded exosomes from RAW 264.7 macrophages not only promote the accumulation of the drug at the tumor site but also increase the particles uptake by the cancer cells compared with liposomes or polystyrene nanoparticles [168]. In recent studies, extracellular membrane isolated from natural killer cells fused with liposomes were used to deliver doxorubicin to MCF-7 tumor bearing mice; this demonstrated more effective tumor inhibition compared to the free doxorubicin injection [128]. In another study, exosomes derived from transfected siRNA/HEK-293T cells reduced the tumor weight and size of a SGC-7901-tumor mouse model [169], indicating that exosomes, in addition of their targeting properties, also conserve the characteristics of the parental cell, which opens the possibility of engineering exosomes with potential therapeutic applications. The results here indicate that HUC-MSCs exosomes can accumulate at the tumor site *in vivo* and may reduce proliferation of cancer cells in vitro in a dose-dependent fashion.

The mechanisms involved in the uptake or proliferation effects were not evaluated here. However, there is evidence that the osteosarcoma tumor niche contains a population of non-malignant MSCs with normal karyotype and without tumor-related abnormalities [170], which could explain the affinity of HUC-MSC exosomes for this particular kind of tumor. Additionally, the bidirectional interaction between osteosarcoma cells and MSCs in metabolic reprograming, has been suggested [171, 172]. Hoshino *et al.* demonstrated the involvement of exosomal integrins in the targeting of

metastatic niches by exosomes derived from breast and pancreatic cancer [14]. This evidence suggests that the cell membrane composition of exosomes maybe provide them with specific targeting properties.

We cannot claim that MSC exosomes "home" to tumors because certain key elements are missing. Our *in vivo* studies support the notion that MSC exosomes accumulate within tumor for 48 hours after intravenous infusion. Conditioned medium from umbilical cord-derived MSCs was used to isolated exosomes. These exosomes were characterized by TEM, western blot, and size and charge characterization standard to the field. The exosomes expressed tetraspanins CD9, CD63, and CD81, and Na/K ATPase and Hsp70, showed a size of 50-100 nm (DLS, NTA and TEM) and a ZP of -16 to -19 mV, suggesting that they have similar physicochemical characteristics to MSC exosomes previously reported [173-182]. We prepared several batches of exosomes from MSC condition medium derived from two independent MSC lines and those exosomes shared similar physicochemical and physiological properties. Based upon this data, we conclude that MSC exosomes were employed here. We note that new methods isolate subsets of extracellular vesicles (EVs) [28, 183-186], and using different subsets may produce different distribution within tissues. Second, the MSC exosomes were labeled using several methods: fusion with Rhodamine-B labeled liposomes, gadolinium incorporation, and NIR dye incorporation, or labeled with both Rhodamine-B and GdL. Of these methods, GdL labeling was characterized more fully than the other methods, and demonstrated good stability. The exosomes are apparent unchanged in terms of their physicochemical properties, protein markers and functional properties such as accumulation in osteosarcoma cells in vitro by the labeling process. For example, the exosome size by dynamic light scattering, nanoparticle tracking analysis, zeta potential and transmission

electron microscopy indicated similar properties to naive exosomes (figure 2). Similarly, dot blot for CD9 and CD81, results were similar between naive exosomes and GdL exosomes (figure 3b). Here, labeled exosomes were added to cancer cell lines *in vitro*, and their incorporation was found to be time-dependent in two ways: confocal microscopy and flow cytometry. Confocal microscopy showed that exosomes were located in the cytoplasm, and not attached to the cell surface or inside the nucleus of cancer cells. The flow cytometry indicated that exosome accumulation in cancer cells increases over 24 hours after introduction. These results indicate that the accumulation of naive and GdL labeled exosomes within cancer cells in vitro was similar (figure 23). Next, we found that exposure to MSC exosomes reduced the proliferation of mouse and human osteosarcoma cell lines. The specificity was indicated by a dose-response relationship, and exosomes did not change Annexin V staining. This suggests that the exosomes reduces proliferation by increasing cancer cell population doubling time and not by increasing apoptosis. Our results suggest that the effect of naive-, GdL-labeled or GdL and RhB labeled exosomes on mouse and human osteosarcoma cell proliferation in vitro may differ, but the effect is small and not clearly dose-dependent (figure 21). Additional work is needed to understand whether the new methods employed to introduce the labeling to the exosome or whether the label itself is responsible for these changes in proliferation after labeling.

Other have shown that MSC exosomes are taken up by cancer cell lines or affect the physiology cancer cell lines *in vitro* [97, 181, 187, 188]. For example, Altanerova *et al*. reported that iron oxide labeled MSC exosomes accumulate within prostate cancer cells, and those cancer cells can be killed by magnetic hyperthermia [187]. Similarly, Lee *et al.* found that mouse bone marrow-derived MSC exosomes accumulate in mouse breast cancer cell line 4T1 (mouse) over 24 hours [188]. Note that Lee *et al*. reported that MSC exosomes did not affect the proliferation of breast

cancer cells *in vitro*, but did inhibit tumor progression and angiogenesis *in vivo*. Qi et al. reported that human bone marrow-derived MSCs accumulate in human osteosarcoma cell line MG3 and gastric cancer cell line SGC7901 over 24 hours [97]. In contrast to our observations, Qi J *et al*. reported that MSC derived exosomes *increased* the proliferation of human osteosarcoma MG63 cells and gastric cancer SGC7901 cell lines in a dose-response fashion. Please note that in their work, 200-800 ug/ml exosomes were used in the dose-response study. This represents approximately 3 orders of magnitude more exosomes than used here (67-200 ng/ml). Therefore, one possibility of the difference in the present study and Qi *et al.*'s is the "dose" of exosomes. Another explanation for these differences is the osteosarcoma cell lines were used.

In summary, our *in vitro* work shows that MSC exosomes accumulate within human and mouse osteosarcoma cells over 24 hours and affect cancer cell proliferation at 67-200 ng/ml concentration. Labeling MSC exosomes with GdL or GdL and DiR may have a small toxic effect on human and mouse osteosarcoma cell lines compared to naive exosomes. Together with previous work, it is clear that MSC exosomes accumulate within the cytoplasm of human and mouse cancer cell lines *in vitro* and may affect proliferation of these cell lines in a dose-dependent fashion.

We examined the biodistribution of labeled MSC exosomes in tumor bearing mice after intravenous injection of 5 ug/g bodyweight. In different experiments, one using 14.1 tesla MRI and the other using bioimaging of near infrared dye labeled exosomes, we determined biodistribution. To our knowledge, this is the first report of biodistribution of GdL labeled MSC exosomes in tumor bearing mice. Strikingly, we found the second highest accumulation of GdL exosomes, 18 %, within the tumor 24 hours after intravenous injection, with liver having the highest accumulation of GdL labeled exosomes. It is worth noting that gadolinium MRI contrast

media (commercial name Magnevist®) has been used previously in mouse models of osteosarcoma [189, 190]. However unmodified Magnevist® does not enhance contrast specifically in the tumor as we report here.

In contrast, we found the highest accumulation of DiR labeled exosomes in spleen followed by the liver (with the spleen having about twice the fluorescent intensity as the liver). Next most accumulation was in the tumor and lungs. Notably, the control DiR-labeled liposomes had about equal fluorescent intensity in liver and spleen, followed by tumor and lungs. This suggests different distribution patterns by exosome labeling method. First, note that the spleen was not found to accumulate GdL exosomes in contrast to DiR-exosomes. Second, the accumulation in the tumor by GdL exosomes may be higher than DiR exosome. Future work is needed to confirm this observation. In addition, there appears to be differences in the time-dependent accumulation of DiR labeled exosomes and DiR-labeled liposomes. The control particles, DiR-labeled liposomes, reached a peak fluorescence intensity within the tumor sooner than the DiR-labeled exosomes (at 3 hours), however, the intensity did not change after the 3h observation point (figure 25C). In contrast, the signal intensity for labeled exosomes increased over the 48 hours observation window (figure 25C), and at the 48 hours observation period, the fluorescent signal observed using the labeled exosomes was about double the intensity of the fluorescent liposome control nanoparticle. This data suggests that the GdL labeling of exosomes confers a higher sensitivity than DiR labeling of exosomes to identify tumor cells. Differences were also noted in accumulation of exosomes in spleen between DiR and GdL. Both of these preliminary observations require follow-up.

There is limited information about the biodistribution of MSC exosomes after intravenous injection. For example, distribution to the brain was reported after MSC exosomes labeled with gold nanoparticles were injected into stroke-damaged mice [191, 192]. More biodistribution

information was reported with near-infrared dye labeled MSC exosomes in healthy mice [135], or in mice following acute kidney injury [160]. These reports indicated that DiR labeled MSC exosomes accumulate in most in liver and spleen after intravenous injection in healthy animals [135, 160], and that exosomes may accumulate in tissues that are injured [160] or in a tumor [135]. These reports agree with DiR labeled MSC exosomes' biodistribution reported here.

The study by Wilklander *et al.* compared several different sources of exosomes, and compared the dose effect, the effect of route of injection, the changes in exosome accumulation over time on biodistribution. They found that DiR labeled exosomes regardless of tissue source tend to accumulate most in liver, spleen, gastrointestinal track and heart and lungs. Second, they showed that HEK293T exosomes accumulate in tumor tissue in tumor bearing mice, and while HEK293T exosomes accumulate in tumor, they accumulate at higher levels in liver, spleen, heart and lungs, and the gastrointestinal track at 24 hours, than in tumor. Thus, their observations generally agree with the observations reported here: DiR labeled exosomes accumulate in tumor, but at a lower level than liver and spleen. The Wiklander *et al*. paper suggests that tissue that exosomes originate from may influence exosome accumulation or distribution. This observation agrees with a hypothesis posed by Rana S *et al*. regarding exosomal tetraspanins contributing to target selection [193, 194]. The tissue specificity for exosome accumulation indicated by Rana *et al*. was not observed either by Wilklander *et al*. or in the present paper. This difference may be due to differences in the exosome populations used. Here, we show DiR labeled exosome accumulation in tumor increased continuously over the 48 hours observation period, which was supported by our observations of exosomes over 24-48 hours *in vitro*. In summary, 18 % of GdL labeled exosomes signal was found in tumor at 24 hours after injection and few exosomes were found in spleen using this labeling method. This observation suggests that the labeling method may affect

the biodistribution of exosomes. Since this is the first report of GdL labeled exosomes and their biodistribution, further work is needed to confirm this observation and to understand whether labeling affects exosome biodistribution or pharmacokinetics in vivo or toxicity *in vitro*.

The present report is the first to show that MSC exosomes continuously accumulate within osteosarcoma tumors over 24-48 hours *in vivo*. A limitation of the present work is the use of an ectopic osteosarcoma model. A goal of our work is to utilize labeled exosomes to image cancer metastasis in patients. While the ectopic model used here demonstrated a proof-of-concept, the orthotopic model will be considered for follow on work since it mimics the natural tumor environment and because it may increase the likelihood of metastatic cancer [195]. While exosome accumulated within tumor in vivo, a limitation of our experiments is that we did not demonstrate whether the labeled exosomes entered cancer cells, tumor stromal cells (MSCs) or infiltrating immune cells. Similarly, our experiments suggest that labeling exosomes with GdL may confer greater tumor specificity that labeling with DiR. Finally, while labeled liposomes did not continue to accumulate within the tumor past 3 after intravenous injection, we did not test whether exosomes derived from other cells, such as the HEK293T cells, or GdL labeled liposomes would show a different rate of accumulation within tumor. These critical questions need to be answered in the future.

5. Conclusions

In summary, naive and labeled MSC exosomes entered cancer cells, reside in their cytoplasm, and modestly inhibit human and mouse osteosarcoma cell line proliferation *in vitro* in a dose-dependent fashion. These observations are in agreement with previous work that shows that MSC exosomes enter a variety of tumor cell lines *in vitro* and affect their proliferation. Second, in the first study of its kind, we showed that GdL- or DiR- labeled MSC exosomes introduced into tumor bearing mice accumulate in the tumor over a 24-48 hours period. The accumulation within tumor by DiR labeled exosomes resulted in about double the fluorescence in tumor compared to labeled liposomes used as controls at the 48 hours observation point; similarly, about 18 % of the GdL was found within the tumor 24 hours after injection. Since DiR labeled liposomes did not continue to accumulate within tumor beyond 3 hours after injection, this difference suggests that exosomes continue to leave the vasculature and enter tumor and get sequestered over 24-48 hours. Third, DiR labeled exosomes have a biodistribution that is grossly similar to that seen by other DiR labeled nanoparticles including exosomes derived from other tissues after intravenous injection, with the majority being located in major organs such as liver and spleen. When GdL exosomes were tracked, the highest accumulation was found in liver (38 %) followed by tumor (18 %). Finally, the accumulation of DiR- or GdL labeled exosomes in tumor cells *in vitro* and *in vivo* over 24-48 hours , does not provide strong evidence of special tumor specificity of MSC exosomes. The demonstration of tumor-specific “homing” remains open. Simple extravasation in the tumor bed due to leaky epithelium enables intravenously administered chemotherapeutics to enter (and leave) the tumor. That MSC exosomes accumulate within tumors over 24-48 hours suggests that they are taken up by some cell within the tumor, however, the target specificity previously suggested has yet to be demonstrated conclusively [194].

Bibliography

1. Horstman LL, Ahn YS. Platelet microparticles: a wide-angle perspective. Crit Rev Oncol Hematol. 1999; 30: 111-42.

2. Owens AP, 3rd, Mackman N. Microparticles in hemostasis and thrombosis. Circ Res. 2011; 108: 1284-97.

3. Pan BT, Johnstone RM. Fate of the Transferrin Receptor during Invitro Maturation of Sheep Reticulocytes. Fed Proc. 1983; 42: 605-.

4. Trams EG, Lauter CJ, Salem N, Jr., Heine U. Exfoliation of membrane ecto-enzymes in the form of micro-vesicles. Biochim Biophys Acta. 1981; 645: 63-70.

5. Johnstone RM, Adam M, Hammond JR, Orr L, Turbide C. Vesicle Formation during Reticulocyte Maturation - Association of Plasma-Membrane Activities with Released Vesicles (Exosomes). Journal of Biological Chemistry. 1987; 262: 9412-20.

6. Kulp A, Kuehn MJ. Biological functions and biogenesis of secreted bacterial outer membrane vesicles. Annu Rev Microbiol. 2010; 64: 163-84.

7. Bonucci E. The Origin of Matrix Vesicles and Their Role in Calcification of Cartilage and Bone. Eur J Cell Biol. 1980; 22: 483-.

8. Raposo G, Nijman HW, Stoorvogel W, Leijendekker R, Harding CV, Melief CJM, et al. B lymphocytes secrete antigen-presenting vesicles. Journal of Experimental Medicine. 1996; 183: 1161-72.

9. Ratajczak J, Miekus K, Kucia M, Zhang J, Reca R, Dvorak P, et al. Embryonic stem cell-derived microvesicles reprogram hematopoietic progenitors: evidence for horizontal transfer of mRNA and protein delivery. Leukemia. 2006; 20: 847-56.

10. Valadi H, Ekstrom K, Bossios A, Sjostrand M, Lee JJ, Lotvall JO. Exosome-mediated transfer of mRNAs and microRNAs is a novel mechanism of genetic exchange between cells. Nature Cell Biology. 2007; 9: 654-U72.

11. Guescini M, Genedani S, Stocchi V, Agnati LF. Astrocytes and Glioblastoma cells release exosomes carrying mtDNA. J Neural Transm (Vienna). 2010; 117: 1-4.

12. Balaj L, Lessard R, Dai L, Cho YJ, Pomeroy SL, Breakefield XO, et al. Tumour microvesicles contain retrotransposon elements and amplified oncogene sequences. Nat Commun. 2011; 2: 180.

13. Thakur BK, Zhang H, Becker A, Matei I, Huang Y, Costa-Silva B, et al. Double-stranded DNA in exosomes: a novel biomarker in cancer detection. Cell Res. 2014; 24: 766.

14. Hoshino A, Costa-Silva B, Shen TL, Rodrigues G, Hashimoto A, Mark MT, et al. Tumour exosome integrins determine organotropic metastasis. Nature. 2015; 527: 329-+.

15. Thery C, Ostrowski M, Segura E. Membrane vesicles as conveyors of immune responses. Nature Reviews Immunology. 2009; 9: 581-93.

16. Deatherage BL, Cookson BT. Membrane Vesicle Release in Bacteria, Eukaryotes, and Archaea: a Conserved yet Underappreciated Aspect of Microbial Life. Infection and Immunity. 2012; 80: 1948-57.

17. Brown L, Wolf JM, Prados-Rosales R, Casadevall A. Through the wall: extracellular vesicles in Gram-positive bacteria, mycobacteria and fungi. Nat Rev Microbiol. 2015; 13: 620-30.

18. Takemoto K, Imoto M. Exosomes in mammals with greater habitat variability contain more proteins and RNAs. R Soc Open Sci. 2017; 4: 170162.

19. Rutter BD, Innes RW. Extracellular Vesicles Isolated from the Leaf Apoplast Carry Stress-Response Proteins. Plant Physiol. 2017; 173: 728-41.

20. Gyorgy B, Szabo TG, Pasztoi M, Pal Z, Misjak P, Aradi B, et al. Membrane vesicles, current state-of-the-art: emerging role of extracellular vesicles. Cellular and Molecular Life Sciences. 2011; 68: 2667-88.

21. Kim HG, Kwon K, Suh HW, Lee S, Park KH, Kwon OY, et al. Exosome isolation from hemolymph of Korean rhinoceros beetle, Allomyrina dichotoma (Coleoptera: Scarabaeidae). Entomol Res. 2015; 45: 339-44.

22. Giglio A, Perrotta ID, Brandmayr P. Exosomes: Ultrastructural evidence in epithelial cells of Malpighian tubules. Micron. 2017; 100: 34-7.

23. Andrulis ED, Werner J, Nazarian A, Erdjument-Bromage H, Tempst P, Lis JT. The RNA processing exosome is linked to elongating RNA polymerase II in Drosophila. Nature. 2002; 420: 837-41.

24. Tricarico C, Clancy J, D'Souza-Schorey C. Biology and biogenesis of shed microvesicles. Small GTPases. 2017; 8: 220-32.

25. Das K, Prasad R, Roy S, Mukherjee A, Sen P. The Protease Activated Receptor2 Promotes Rab5a Mediated Generation of Pro-metastatic Microvesicles. Sci Rep. 2018; 8: 7357.

26. Menck K, Sonmezer C, Worst TS, Schulz M, Dihazi GH, Streit F, et al. Neutral sphingomyelinases control extracellular vesicles budding from the plasma membrane. J Extracell Vesicles. 2017; 6: 1378056.

27. Colombo F, Bastoni M, Nigro A, Podini P, Finardi A, Casella G, et al. Cytokines Stimulate the Release of Microvesicles from Myeloid Cells Independently from the P2X7 Receptor/Acid Sphingomyelinase Pathway. Front Immunol. 2018; 9: 204.

28. Konoshenko MY, Lekchnov EA, Vlassov AV, Laktionov PP. Isolation of Extracellular Vesicles: General Methodologies and Latest Trends. Biomed Res Int. 2018; 2018: 8545347.

29. Kowal J, Tkach M, Thery C. Biogenesis and secretion of exosomes. Curr Opin Cell Biol. 2014; 29: 116-25.

30. Schmidt O, Teis D. The ESCRT machinery. Current Biology. 2012; 22: R116-R20.

31. Wenzel EM, Schultz SW, Schink KO, Pedersen NM, Nahse V, Carlson A, et al. Concerted ESCRT and clathrin recruitment waves define the timing and morphology of intraluminal vesicle formation. Nat Commun. 2018; 9: 2932.

32. Baietti MF, Zhang Z, Mortier E, Melchior A, Degeest G, Geeraerts A, et al. Syndecan-syntenin-ALIX regulates the biogenesis of exosomes. Nat Cell Biol. 2012; 14: 677-85.

33. Ghossoub R, Lembo F, Rubio A, Gaillard CB, Bouchet J, Vitale N, et al. Syntenin-ALIX exosome biogenesis and budding into multivesicular bodies are controlled by ARF6 and PLD2. Nature Communications. 2014; 5.

34. Meister M, Banfer S, Gartner U, Koskimies J, Amaddii M, Jacob R, et al. Regulation of cargo transfer between ESCRT-0 and ESCRT-I complexes by flotillin-1 during endosomal sorting of ubiquitinated cargo. Oncogenesis. 2017; 6.

35. Stuffers S, Wegner CS, Stenmark H, Brech A. Multivesicular Endosome Biogenesis in the Absence of ESCRTs. Traffic. 2009; 10: 925-37.

36. Trajkovic K, Hsu C, Chiantia S, Rajendran L, Wenzel D, Wieland F, et al. Ceramide triggers budding of exosome vesicles into multivesicular Endosomes. Science. 2008; 319: 1244-7.

37. Kajimoto T, Okada T, Miya S, Zhang LF, Nakamura SI. Ongoing activation of sphingosine 1-phosphate receptors mediates maturation of exosomal multivesicular endosomes. Nature Communications. 2013; 4.

38. Kajimoto T, Mohamed NNI, Badawy SMM, Matovelo SA, Hirase M, Nakamura S, et al. Involvement of Gbetagamma subunits of Gi protein coupled with S1P receptor on multivesicular endosomes in F-actin formation and cargo sorting into exosomes. J Biol Chem. 2018; 293: 245-53.

39. Troyer DL, Weiss ML. Wharton's jelly-derived cells are a primitive stromal cell population. Stem Cells. 2008; 26: 591-9.

40. Dominici M, Le Blanc K, Mueller I, Slaper-Cortenbach I, Marini F, Krause D, et al. Minimal criteria for defining multipotent mesenchymal stromal cells. The International Society for Cellular Therapy position statement. Cytotherapy. 2006; 8: 315-7.

41. Haasters F, Prall WC, Anz D, Bourquin C, Pautke C, Endres S, et al. Morphological and immunocytochemical characteristics indicate the yield of early progenitors and represent a quality control for human mesenchymal stem cell culturing. Journal of Anatomy. 2009; 214: 759-67.

42. Lindner U, Kramer J, Rohwedel J, Schlenke P. Mesenchymal Stem or Stromal Cells: Toward a Better Understanding of Their Biology? Transfus Med Hemoth. 2010; 37: 75-83.

43. Liao L, Zhao RC. Mesenchymal Stem Cells and Their Immunomodulatory Properties. In: Zhao RC, editor. Stem Cells: Basics and Clinical Translation. Dordrecht: Springer Netherlands; 2015. p. 67-83.

44. Zuk PA, Zhu M, Ashjian P, De Ugarte DA, Huang JI, Mizuno H, et al. Human adipose tissue is a source of multipotent stem cells. Mol Biol Cell. 2002; 13: 4279-95.

45. Kim EY, Lee KB, Kim MK. The potential of mesenchymal stem cells derived from amniotic membrane and amniotic fluid for neuronal regenerative therapy. Bmb Rep. 2014; 47: 135-40.

46. Weiss ML, Anderson C, Medicetty S, Seshareddy KB, Weiss RJ, VanderWerff I, et al. Immune properties of human umbilical cord Wharton's jelly-derived cells. Stem Cells. 2008; 26: 2865-74.

47. Sibov TT, Severino P, Marti LC, Pavon LF, Oliveira DM, Tobo PR, et al. Mesenchymal stem cells from umbilical cord blood: parameters for isolation, characterization and adipogenic differentiation. Cytotechnology. 2012; 64: 511-21.

48. Rasmusson I, Ringden O, Sundberg B, Le Blanc K. Mesenchymal stem cells inhibit lymphocyte proliferation by mitogens and alloantigens by different mechanisms. Exp Cell Res. 2005; 305: 33-41.

49. Wang M, Yang Y, Yang D, Luo F, Liang W, Guo S, et al. The immunomodulatory activity of human umbilical cord blood-derived mesenchymal stem cells in vitro. Immunology. 2009; 126: 220-32.

50. Zhang J, Lv S, Liu X, Song B, Shi L. Umbilical Cord Mesenchymal Stem Cell Treatment for Crohn's Disease: A Randomized Controlled Clinical Trial. Gut Liver. 2018; 12: 73-8.

51. Riordan NH, Morales I, Fernandez G, Allen N, Fearnot NE, Leckrone ME, et al. Clinical feasibility of umbilical cord tissue-derived mesenchymal stem cells in the treatment of multiple sclerosis. J Transl Med. 2018; 16.

52. Wang YL, Xue P, Xu CY, Wang Z, Liu XS, Hua LL, et al. SPK1-transfected UCMSC has better therapeutic activity than UCMSC in the treatment of experimental autoimmune encephalomyelitis model of Multiple sclerosis. Sci Rep-Uk. 2018; 8.

53. Wang LM, Wang LH, Cong XL, Liu GY, Zhou JJ, Bai B, et al. Human Umbilical Cord Mesenchymal Stem Cell Therapy for Patients with Active Rheumatoid Arthritis: Safety and Efficacy. Stem Cells and Development. 2013; 22: 3192-202.

54. Zhao C, Zhang L, Kong W, Liang J, Xu XY, Wu HY, et al. Umbilical Cord-Derived Mesenchymal Stem Cells Inhibit Cadherin-11 Expression by Fibroblast-Like Synoviocytes in Rheumatoid Arthritis. J Immunol Res. 2015.

55. Kim JH, Jo CH, Kim HR, Hwang YI. Comparison of Immunological Characteristics of Mesenchymal Stem Cells from the Periodontal Ligament, Umbilical Cord, and Adipose Tissue. Stem Cells Int. 2018; 2018: 8429042.

56. Nakajima K, Kunimatsu R, Ando K, Ando T, Hayashi Y, Kihara T, et al. Comparison of the bone regeneration ability between stem cells from human exfoliated deciduous teeth, human dental pulp stem cells and human bone marrow mesenchymal stem cells. Biochem Bioph Res Co. 2018; 497: 876-82.

57. Yaneselli KM, Kuhl CP, Terraciano PB, de Oliveira FS, Pizzato SB, Pazza K, et al. Comparison of the characteristics of canine adipose tissue-derived mesenchymal stem cells extracted from different sites and at different passage numbers. Journal of Veterinary Science. 2018; 19: 13-20.

58. Spees JL, Lee RH, Gregory CA. Mechanisms of mesenchymal stem/stromal cell function. Stem Cell Res Ther. 2016; 7.

59. Dabrowski FA, Burdzinska A, Kulesza A, Sladowska A, Zolocinska A, Gala K, et al. Comparison of the paracrine activity of mesenchymal stem cells derived from human umbilical cord, amniotic membrane and adipose tissue. J Obstet Gynaecol Re. 2017; 43: 1758-68.

60. Vignais ML, Caicedo A, Brondello JM, Jorgensen C. Cell Connections by Tunneling Nanotubes: Effects of Mitochondrial Trafficking on Target Cell Metabolism, Homeostasis, and Response to Therapy. Stem Cells International. 2017.

61. Han H, Hu JQ, Yan Q, Zhu JZ, Zhu ZB, Chen YJ, et al. Bone marrow-derived mesenchymal stem cells rescue injured H9c2 cells via transferring intact mitochondria through tunneling nanotubes in an in vitro simulated ischemia/reperfusion model. Mol Med Rep. 2016; 13: 1517-24.

62. Jackson MV, Morrison TJ, Doherty DF, Mcauley DF, Matthay MA, Kissenpfennig A, et al. Mitochondrial Transfer via Tunneling Nanotubes is an Important Mechanism by Which Mesenchymal Stem Cells Enhance Macrophage Phagocytosis in the In Vitro and In Vivo Models of ARDS. Stem Cells. 2016; 34: 2210-23.

63. Wang XQ, Omar O, Vazirisani F, Thomsen P, Ekstrom K. Mesenchymal stem cell-derived exosomes have altered microRNA profiles and induce osteogenic differentiation depending on the stage of differentiation. Plos One. 2018; 13.

64. Luther KM, Haar L, McGuinness M, Wang Y, Lynch TL, Phan A, et al. Exosomal miR-21a-5p mediates cardioprotection by mesenchymal stem cells. J Mol Cell Cardiol. 2018; 119: 125-37.

65. Liu Y, Lou G, Li A, Zhang T, Qi J, Ye D, et al. AMSC-derived exosomes alleviate lipopolysaccharide/d-galactosamine-induced acute liver failure by miR-17-mediated reduction of TXNIP/NLRP3 inflammasome activation in macrophages. Ebiomedicine. 2018.

66. de Witte SFH, Luk F, Sierra Parraga JM, Gargesha M, Merino A, Korevaar SS, et al. Immunomodulation By Therapeutic Mesenchymal Stromal Cells (MSC) Is Triggered Through Phagocytosis of MSC By Monocytic Cells. Stem Cells. 2018; 36: 602-15.

67. Herberts CA, Kwa MSG, Hermsen HPH. Risk factors in the development of stem cell therapy. Journal of Translational Medicine. 2011; 9.

68. Cui LL, Kerkela E, Bakreen A, Nitzsche F, Andrzejewska A, Nowakowski A, et al. The cerebral embolism evoked by intra-arterial delivery of allogeneic bone marrow mesenchymal stem cells in rats is related to cell dose and infusion velocity. Stem Cell Research & Therapy. 2015; 6.

69. Ridge SM, Sullivan FJ, Glynn SA. Mesenchymal stem cells: key players in cancer progression. Molecular Cancer. 2017; 16.

70. Ganta C, Chiyo D, Ayuzawa R, Rachakatla R, Pyle M, Andrews G, et al. Rat umbilical cord stem cells completely abolish rat mammary carcinomas with no evidence of metastasis or recurrence 100 days post-tumor cell inoculation. Cancer Res. 2009; 69: 1815-20.

71. Rachakatla RS, Pyle MM, Ayuzawa R, Edwards SM, Marini FC, Weiss ML, et al. Combination treatment of human umbilical cord matrix stem cell-based interferon-beta gene therapy and 5-fluorouracil significantly reduces growth of metastatic human breast cancer in SCID mouse lungs. Cancer Invest. 2008; 26: 662-70.

72. Rachakatla RS, Marini F, Weiss ML, Tamura M, Troyer D. Development of human umbilical cord matrix stem cell-based gene therapy for experimental lung tumors. Cancer Gene Ther. 2007; 14: 828-35.

73. Lee RH, Pulin AA, Seo MJ, Kota DJ, Ylostalo J, Larson BL, et al. Intravenous hMSCs Improve Myocardial Infarction in Mice because Cells Embolized in Lung Are Activated to Secrete the Anti-inflammatory Protein TSG-6. Cell Stem Cell. 2009; 5: 54-63.

74. Ge JF, Guo L, Wang S, Zhang YL, Cai T, Zhao RCH, et al. The Size of Mesenchymal Stem Cells is a Significant Cause of Vascular Obstructions and Stroke. Stem Cell Rev Rep. 2014; 10: 295-303.

75. Assuncao-Silva RC, Mendes-Pinheiro B, Patricio P, Behie L, Teixeira FG, Pinto L, et al. Exploiting the impact of the secretome of MSCs isolated from different tissue sources on neuronal differentiation and axonal growth. Biochimie. 2018.

76. Damania A, Jaiman D, Teotia AK, Kumar A. Mesenchymal stromal cell-derived exosome-rich fractionated secretome confers a hepatoprotective effect in liver injury. Stem Cell Research & Therapy. 2018; 9.

77. Sarkar P, Redondo J, Kemp K, Ginty M, Wilkins A, Scolding NJ, et al. Reduced neuroprotective potential of the mesenchymal stromal cell secretome with ex vivo expansion, age and progressive multiple sclerosis. Cytotherapy. 2018; 20: 21-8.

78. Sevivas N, Teixeira FG, Portugal R, Direito-Santos B, Espregueira-Mendes J, Oliveira FJ, et al. Mesenchymal Stem Cell Secretome Improves Tendon Cell Viability In Vitro and Tendon-Bone Healing In Vivo When a Tissue Engineering Strategy Is Used in a Rat Model of Chronic Massive Rotator Cuff Tear. Am J Sport Med. 2018; 46: 449-59.

79. Lai RC, Arslan F, Lee MM, Sze NSK, Choo A, Chen TS, et al. Exosome secreted by MSC reduces myocardial ischemia/reperfusion injury. Stem Cell Res. 2010; 4: 214-22.

80. Willis GR, Fernandez-Gonzalez A, Anastas J, Vitali SH, Liu XL, Ericsson M, et al. Mesenchymal Stromal Cell Exosomes Ameliorate Experimental Bronchopulmonary Dysplasia and Restore Lung Function through Macrophage Immunomodulation. Am J Resp Crit Care. 2018; 197: 104-16.

81. Oshima K, Aoki N, Kato T, Kitajima K, Matsuda T. Secretion of a peripheral membrane protein, MFG-E8, as a complex with membrane vesicles - A possible role in membrane secretion. Eur J Biochem. 2002; 269: 1209-18.

82. Fedele C, Singh A, Zerlanko BJ, Iozzo RV, Languino LR. The alpha(v)beta(6) Integrin Is Transferred Intercellularly via Exosomes. Journal of Biological Chemistry. 2015; 290: 4545-51.

83. Cui X, He Z, Liang Z, Chen Z, Wang H, Zhang J. Exosomes From Adipose-derived Mesenchymal Stem Cells Protect the Myocardium Against Ischemia/Reperfusion Injury Through Wnt/beta-Catenin Signaling Pathway. J Cardiovasc Pharmacol. 2017; 70: 225-31.

84. Shimoda A, Tahara Y, Sawada S, Sasaki Y, Akiyoshi K. Glycan profiling analysis using evanescent-field fluorescence-assisted lectin array: Importance of sugar recognition for cellular uptake of exosomes from mesenchymal stem cells. Biochem Bioph Res Co. 2017; 491: 701-7.

85. McAtee CO, Booth C, Elowsky C, Zhao L, Payne J, Fangman T, et al. Prostate tumor cell exosomes containing hyaluronidase Hyal1 stimulate prostate stromal cell motility by engagement of FAK-mediated integrin signaling. Matrix Biol. 2018.

86. Iraci N, Gaude E, Leonardi T, Costa ASH, Cossetti C, Peruzzotti-Jametti L, et al. Extracellular vesicles are independent metabolic units with asparaginase activity. Nat Chem Biol. 2017; 13: 951-+.

87. Meng F, Li Z, Zhang Z, Yang Z, Kang Y, Zhao X, et al. MicroRNA-193b-3p regulates chondrogenesis and chondrocyte metabolism by targeting HDAC3. Theranostics. 2018; 8: 2862-83.

88. Kim J, Kim TY, Lee MS, Mun JY, Ihm C, Kim SA. Exosome cargo reflects TGF-beta1-mediated epithelial-to-mesenchymal transition (EMT) status in A549 human lung adenocarcinoma cells. Biochem Biophys Res Commun. 2016; 478: 643-8.

89. Sharma A. Transgenerational epigenetics: Integrating soma to germline communication with gametic inheritance. Mech Ageing Dev. 2017; 163: 15-22.

90. Shah N, Ishii M, Brandon C, Ablonczy Z, Cai J, Liu Y, et al. Extracellular vesicle-mediated long-range communication in stressed retinal pigment epithelial cell monolayers. Biochim Biophys Acta. 2018; 1864: 2610-22.

91. Smith VL, Cheng Y, Bryant BR, Schorey JS. Exosomes function in antigen presentation during an in vivo Mycobacterium tuberculosis infection. Sci Rep-Uk. 2017; 7.

92. Zhang B, Yeo RWY, Lai RC, Sim EWK, Chin KC, Lim SK. Mesenchymal stromal cell exosome-enhanced regulatory T-cell production through an antigen-presenting cell-mediated pathway. Cytotherapy. 2018; 20: 687-96.

93. Sung BH, Ketova T, Hoshino D, Zijlstra A, Weaver AM. Directional cell movement through tissues is controlled by exosome secretion. Nat Commun. 2015; 6.

94. Huang BX, Lu JF, Ding CY, Zou QY, Wang W, Li H. Exosomes derived from human adipose mesenchymal stem cells improve ovary function of premature ovarian insufficiency by targeting SMAD. Stem Cell Res Ther. 2018; 9.

95. Yuan FL, Wu QY, Miao ZN, Xu MH, Xu RS, Jiang DL, et al. Osteoclast-Derived Extracellular Vesicles: Novel Regulators of Osteoclastogenesis and Osteoclast-Osteoblasts Communication in Bone Remodeling. Front Physiol. 2018; 9: 628.

96. Qi J, Zhou YL, Jiao ZY, Wang X, Zhao Y, Li YB, et al. Exosomes Derived from Human Bone Marrow Mesenchymal Stem Cells Promote Tumor Growth Through Hedgehog Signaling Pathway. Cell Physiol Biochem. 2017; 42: 2242-54.

97. Qi J, Zhou Y, Jiao Z, Wang X, Zhao Y, Li Y, et al. Exosomes Derived from Human Bone Marrow Mesenchymal Stem Cells Promote Tumor Growth Through Hedgehog Signaling Pathway. Cell Physiol Biochem. 2017; 42: 2242-54.

98. Weinberg RA. Oncogenes, Antioncogenes, and the Molecular-Bases of Multistep Carcinogenesis. Cancer Research. 1989; 49: 3713-21.

99. Kumar S, Weaver V. Mechanics, malignancy, and metastasis: The force journey of a tumor cell. Cancer Metast Rev. 2009; 28: 113-27.

100. Horanyi G. Rules of Hungarian Chemical Nomenclature - Physicochemical Definitions and Symbols - the Absolute Electrode Potential - an Explanatory Note. Magy Kem Foly. 1988; 94: 553-63.

101. Kumar D. Pathology of Bone and Soft Tissue Sarcomas. In: Henshaw RM, editor. Sarcoma: A Multidisciplinary Approach to Treatment. Cham: Springer International Publishing; 2017. p. 23-41.

102. Lukes RJ, Collins RD. Immunologic characterization of human malignant lymphomas. Cancer-Am Cancer Soc. 1974; 34: suppl:1488-503.

103. Al-Tubaikh JA. Leukemia. In: Al-Tubaikh JA, editor. Internal Medicine: An Illustrated Radiological Guide. Berlin, Heidelberg: Springer Berlin Heidelberg; 2010. p. 313-8.

104. Cronin KA, Lake AJ, Scott S, Sherman RL, Noone AM, Howlader N, et al. Annual Report to the Nation on the Status of Cancer, part I: National cancer statistics. Cancer. 2018; 124: 2785-800.

105. Society AC. Global Cancer Facts & Figures 3rd Edition. American Cancer Society; Atlanta, Georgia; 2015.

106. Montagnana M, Lippi G. Cancer diagnostics: current concepts and future perspectives. Ann Transl Med. 2017; 5: 268.

107. Stewart BW, Wild C, International Agency for Research on Cancer, World Health Organization. World cancer report 2014. Lyon, France Geneva, Switzerland: International Agency for Research on Cancer WHO Press; 2014.

108. Hanahan D, Weinberg RA. The hallmarks of cancer. Cell. 2000; 100: 57-70.

109. Hanahan D, Weinberg RA. Hallmarks of cancer: the next generation. Cell. 2011; 144: 646-74.

110. Wood MD, Mukherjee J, Pieper RO. Neurofibromin knockdown in glioma cell lines is associated with changes in cytokine and chemokine secretion in vitro. Sci Rep-Uk. 2018; 8.

111. Lau TS, Chan LKY, Wong ECH, Hui CWC, Sneddon K, Cheung H, et al. A loop of cancer-stroma-cancer interaction promotes peritoneal metastasis of ovarian cancer via TNF alpha-TGF alpha-EGFR. Oncogene. 2017; 36: 3576-87.

112. Obata Y, Horikawa K, Takahashi T, Akieda Y, Tsujimoto M, Fletcher JA, et al. Oncogenic signaling by Kit tyrosine kinase occurs selectively on the Golgi apparatus in gastrointestinal stromal tumors. Oncogene. 2017; 36: 3661-72.

113. Fujimura K, Wang H, Watson F, Klemke RL. KRAS oncoprotein expression is regulated by a self-governing eIF5A-PEAK1 feed-forward regulatory loop. Cancer Research. 2018.

114. Ozaki T, Nakagawara A. Role of p53 in Cell Death and Human Cancers. Cancers (Basel). 2011; 3: 994-1013.

115. Levine AJ. Targeting Therapies for the p53 Protein in Cancer Treatments. Annual Review of Cancer Biology. 2019; 3: null.

116. Duhen T, Duhen R, Montler R, Moses J, Moudgil T, de Miranda NF, et al. Co-expression of CD39 and CD103 identifies tumor-reactive CD8 T cells in human solid tumors. Nat Commun. 2018; 9: 2724.

117. Silva IG, Yasinska IM, Sakhnevych SS, Fiedler W, Wellbrock J, Bardelli M, et al. The Tim-3-galectin-9 Secretory Pathway is Involved in the Immune Escape of Human Acute Myeloid Leukemia Cells. Ebiomedicine. 2017; 22: 44-57.

118. El-Badawy A, Ghoneim NI, Nasr MA, Elkhenany H, Ahmed TA, Ahmed SM, et al. Telomerase reverse transcriptase coordinates with the epithelial-to-mesenchymal transition through a feedback loop to define properties of breast cancer stem cells. Biol Open. 2018; 7.

119. Riggi N, Aguet M, Stamenkovic I. Cancer Metastasis: A Reappraisal of Its Underlying Mechanisms and Their Relevance to Treatment. Annu Rev Pathol-Mech. 2018; 13: 117-40.

120. Chen ZL, Zhao XH, Wang JW, Li BZ, Wang Z, Sun J, et al. microRNA-92a promotes lymph node metastasis of human esophageal squamous cell carcinoma via E-cadherin. J Biol Chem. 2011; 286: 10725-34.

121. Ma L, Young J, Prabhala H, Pan E, Mestdagh P, Muth D, et al. miR-9, a MYC/MYCN-activated microRNA, regulates E-cadherin and cancer metastasis. Nat Cell Biol. 2010; 12: 247-U52.

122. Endres M, Kneitz S, Orth MF, Perera RK, Zernecke A, Butt E. Regulation of matrix metalloproteinases (MMPs) expression and secretion in MDA-MB-231 breast cancer cells by LIM and SH3 protein 1 (LASP1). Oncotarget. 2016; 7: 64244-59.

123. Zhou WY, Fong MY, Min YF, Somlo G, Liu L, Palomares MR, et al. Cancer-Secreted miR-105 Destroys Vascular Endothelial Barriers to Promote Metastasis. Cancer Cell. 2014; 25: 501-15.

124. Yin MZ, Zhou HJJ, Zhang JQ, Lin CX, Li HM, Li X, et al. ASK1-dependent endothelial cell activation is critical in ovarian cancer growth and metastasis. Jci Insight. 2017; 2.

125. Maolake A, Izumi K, Natsagdorj A, Iwamoto H, Kadomoto S, Makino T, et al. Tumor necrosis factor-alpha induces prostate cancer cell migration in lymphatic metastasis through CCR7 upregulation. Cancer Sci. 2018; 109: 1524-31.

126. Mukherjee S. The emperor of all maladies : a biography of cancer. 1st Scribner hardcover ed. New York: Scribner; 2010.

127. Nguyen TD, Pitchaimani A, Aryal S. Engineered Nanomedicine with Alendronic Acid Corona Improves Targeting to Osteosarcoma. Sci Rep. 2016; 6: 36707.

128. Pitchaimani A, Nguyen TDT, Aryal S. Natural killer cell membrane infused biomimetic liposomes for targeted tumor therapy. Biomaterials. 2018; 160: 124-37.

129. Lopez-Chaves C, Soto-Alvaredo J, Montes-Bayon M, Bettmer J, Llopis J, Sanchez-Gonzalez C. Gold nanoparticles: Distribution, bioaccumulation and toxicity. In vitro and in vivo studies. Nanomed-Nanotechnol. 2018; 14: 1-12.

130. Mishra V, Baranwal V, Mishra RK, Sharma S, Paul B, Pandey AC. Titanium dioxide nanoparticles augment allergic airway inflammation and Socs3 expression via NF-kappaB pathway in murine model of asthma. Biomaterials. 2016; 92: 90-102.

131. Blanco E, Shen H, Ferrari M. Principles of nanoparticle design for overcoming biological barriers to drug delivery. Nat Biotechnol. 2015; 33: 941-51.

132. Wilhelm S, Tavares AJ, Dai Q, Ohta S, Audet J, Dvorak HF, et al. Analysis of nanoparticle delivery to tumours. Nat Rev Mater. 2016; 1.

133. Kamerkar S, LeBleu VS, Sugimoto H, Yang S, Ruivo CF, Melo SA, et al. Exosomes facilitate therapeutic targeting of oncogenic KRAS in pancreatic cancer. Nature. 2017; 546: 498-503.

134. Hong Y, Nam GH, Koh E, Jeon S, Kim GB, Jeong C, et al. Exosome as a Vehicle for Delivery of Membrane Protein Therapeutics, PH20, for Enhanced Tumor Penetration and Antitumor Efficacy. Adv Funct Mater. 2018; 28.

135. Wiklander OP, Nordin JZ, O'Loughlin A, Gustafsson Y, Corso G, Mager I, et al. Extracellular vesicle in vivo biodistribution is determined by cell source, route of administration and targeting. J Extracell Vesicles. 2015; 4: 26316.

136. Yuan ZQ, Kolluri KK, Gowers KHC, Janes SM. TRAIL delivery by MSC-derived extracellular vesicles is an effective anticancer therapy. Journal of Extracellular Vesicles. 2017; 6.

137. Mendt M, Kamerkar S, Sugimoto H, McAndrews KM, Wu CC, Gagea M, et al. Generation and testing of clinical-grade exosomes for pancreatic cancer. Jci Insight. 2018; 3.

138. Smith JR, Pfeifer K, Petry F, Powell N, Delzeit J, Weiss ML. Standardizing Umbilical Cord Mesenchymal Stromal Cells for Translation to Clinical Use: Selection of GMP-Compliant Medium and a Simplified Isolation Method. Stem Cells International. 2016.

139. Momen-Heravi F. Isolation of Extracellular Vesicles by Ultracentrifugation. Methods Mol Biol. 2017; 1660: 25-32.

140. Pachler K, Lener T, Streif D, Dunai ZA, Desgeorges A, Feichtner M, et al. A Good Manufacturing Practice-grade standard protocol for exclusively human mesenchymal stromal cell-derived extracellular vesicles. Cytotherapy. 2017; 19: 458-72.

141. Aryal S, Key J, Stigliano C, Ananta JS, Zhong M, Decuzzi P. Engineered magnetic hybrid nanoparticles with enhanced relaxivity for tumor imaging. Biomaterials. 2013; 34: 7725-32.

142. Aryal S, Stigliano C, Key J, Ramirez M, Anderson J, Karmonik C, et al. Paramagnetic Gd(3+) labeled red blood cells for magnetic resonance angiography. Biomaterials. 2016; 98: 163-70.

143. Pitchaimani A, Nguyen TDT, Wang HW, Bossmann SH, Aryal S. Design and characterization of gadolinium infused theranostic liposomes. Rsc Adv. 2016; 6: 36898-905.

144. Qian ZQ, Martyna A, Hard RL, Wang J, Appiah-Kubi G, Coss C, et al. Discovery and Mechanism of Highly Efficient Cyclic Cell-Penetrating Peptides. Biochemistry-Us. 2016; 55: 2601-12.

145. Gercel-Taylor C, Atay S, Tullis RH, Kesimer M, Taylor DD. Nanoparticle analysis of circulating cell-derived vesicles in ovarian cancer patients. Analytical Biochemistry. 2012; 428: 44-53.

146. Chernyshev VS, Rachamadugu R, Tseng YH, Belnap DM, Jia YL, Branch KJ, et al. Size and shape characterization of hydrated and desiccated exosomes. Anal Bioanal Chem. 2015; 407: 3285-301.

147. Pi FM, Binzel DW, Lee TJ, Li ZF, Sun MY, Rychahou P, et al. Nanoparticle orientation to control RNA loading and ligand display on extracellular vesicles for cancer regression. Nature Nanotechnology. 2018; 13: 82-+.

148. Kim DK, Kang B, Kim OY, Choi DS, Lee J, Kim SR, et al. EVpedia: an integrated database of high-throughput data for systemic analyses of extracellular vesicles. J Extracell Vesicles. 2013; 2.

149. Keerthikumar S, Chisanga D, Ariyaratne D, Saffar H, Anand S, Zhao KN, et al. ExoCarta: A Web-Based Compendium of Exosomal Cargo. Journal of Molecular Biology. 2016; 428: 688-92.

150. Smith JR, Pfeifer K, Petry F, Powell N, Delzeit J, Weiss ML. Standardizing Umbilical Cord Mesenchymal Stromal Cells for Translation to Clinical Use: Selection of GMP-Compliant Medium and a Simplified Isolation Method. Stem Cells Int. 2016; 2016: 6810980.

151. Liu Y, Peterson DA, Kimura H, Schubert D. Mechanism of cellular 3-(4,5-dimethylthiazol-2-yl)-2,5-diphenyltetrazolium bromide (MTT) reduction. J Neurochem. 1997; 69: 581-93.

152. Waterman RS, Henkle SL, Betancourt AM. Mesenchymal stem cell 1 (MSC1)-based therapy attenuates tumor growth whereas MSC2-treatment promotes tumor growth and metastasis. PLoS One. 2012; 7: e45590.

153. Qiu Y, Guo J, Mao R, Chao K, Chen BL, He Y, et al. TLR3 preconditioning enhances the therapeutic efficacy of umbilical cord mesenchymal stem cells in TNBS-induced colitis via the TLR3-Jagged-1-Notch-1 pathway. Mucosal Immunol. 2017; 10: 727-42.

154. Wang Y, Chen XD, Cao W, Shi YF. Plasticity of mesenchymal stem cells in immunomodulation: pathological and therapeutic implications. Nature Immunology. 2014; 15: 1009-16.

155. Mulder WJ, Strijkers GJ, van Tilborg GA, Griffioen AW, Nicolay K. Lipid-based nanoparticles for contrast-enhanced MRI and molecular imaging. NMR Biomed. 2006; 19: 142-64.

156. Wu S, Ju GQ, Du T, Zhu YJ, Liu GH. Microvesicles Derived from Human Umbilical Cord Wharton's Jelly Mesenchymal Stem Cells Attenuate Bladder Tumor Cell Growth In Vitro and In Vivo. Plos One. 2013; 8.

157. Lee JK, Park SR, Jung BK, Jeon YK, Lee YS, Kim MK, et al. Exosomes Derived from Mesenchymal Stem Cells Suppress Angiogenesis by Down-Regulating VEGF Expression in Breast Cancer Cells. Plos One. 2013; 8.

158. Alarifi S, Ali H, Alkahtani S, Alessia MS. Regulation of apoptosis through bcl-2/bax proteins expression and DNA damage by nano-sized gadolinium oxide. Int J Nanomed. 2017; 12: 4541-51.

159. Ormerod MG, Sun XM, Brown D, Snowden RT, Cohen GM. Quantification of apoptosis and necrosis by flow cytometry. Acta Oncol. 1993; 32: 417-24.

160. Grange C, Tapparo M, Bruno S, Chatterjee D, Quesenberry PJ, Tetta C, et al. Biodistribution of mesenchymal stem cell-derived extracellular vesicles in a model of acute kidney injury monitored by optical imaging. Int J Mol Med. 2014; 33: 1055-63.

161. Wiklander OPB, Nordin JZ, O'Loughlin A, Gustafsson Y, Corso G, Mager I, et al. Extracellular vesicle in vivo biodistribution is determined by cell source, route of administration and targeting. J Extracell Vesicles. 2015; 4.

162. Tokumitsu H, Hiratsuka J, Sakurai Y, Kobayashi T, Ichikawa H, Fukumori Y. Gadolinium neutron-capture therapy using novel gadopentetic acid-chitosan complex nanoparticles: in vivo growth suppression of experimental melanoma solid tumor. Cancer Letters. 2000; 150: 177-82.

163. Laurent S, Burtea C, Elst LV, Muller RN. Synthesis and characterization of new low-molecular-weight lysine-conjugated Gd-DTPA contrast agents. Contrast Media Mol I. 2011; 6: 229-35.

164. Beam AS, Moore KG, Gillis SN, Ford KF, Gray T, Steinwinder AH, et al. GBCAs and Risk for Nephrogenic Systemic Fibrosis: A Literature Review. Radiol Technol. 2017; 88: 583-9.

165. Knoepp F, Bettmer J, Fronius M. Gadolinium released by the linear gadolinium-based contrast-agent Gd-DTPA decreases the activity of human epithelial Na(+) channels (ENaCs). Biochim Biophys Acta. 2017; 1859: 1040-8.

166. Wang J, Zheng Y, Zhao M. Exosome-Based Cancer Therapy: Implication for Targeting Cancer Stem Cells. Front Pharmacol. 2016; 7: 533.

167. Golombek SK, May JN, Theek B, Appold L, Drude N, Kiessling F, et al. Tumor targeting via EPR: Strategies to enhance patient responses. Adv Drug Deliv Rev. 2018.

168. Kim MS, Haney MJ, Zhao Y, Mahajan V, Deygen I, Klyachko NL, et al. Development of exosome-encapsulated paclitaxel to overcome MDR in cancer cells. Nanomed-Nanotechnol. 2016; 12: 655-64.

169. Zhang HY, Wang Y, Bai M, Wang JY, Zhu KG, Liu R, et al. Exosomes serve as nanoparticles to suppress tumor growth and angiogenesis in gastric cancer by delivering hepatocyte growth factor siRNA. Cancer Sci. 2018; 109: 629-41.

170. Brune JC, Tormin A, Johansson MC, Rissler P, Brosjo O, Lofvenberg R, et al. Mesenchymal stromal cells from primary osteosarcoma are non-malignant and strikingly similar to their bone marrow counterparts. International Journal of Cancer. 2011; 129: 319-30.

171. Bonuccelli G, Avnet S, Grisendi G, Salerno M, Granchi D, Dominici M, et al. Role of mesenchymal stem cells in osteosarcoma and metabolic reprogramming of tumor cells. Oncotarget. 2014; 5: 7575-88.

172. Cortini M, Massa A, Avnet S, Bonuccelli G, Baldini N. Tumor-Activated Mesenchymal Stromal Cells Promote Osteosarcoma Stemness and Migratory Potential via IL-6 Secretion. Plos One. 2016; 11.

173. Fang S, Xu C, Zhang Y, Xue C, Yang C, Bi H, et al. Umbilical Cord-Derived Mesenchymal Stem Cell-Derived Exosomal MicroRNAs Suppress Myofibroblast Differentiation by Inhibiting the Transforming Growth Factor-beta/SMAD2 Pathway During Wound Healing. Stem Cells Transl Med. 2016; 5: 1425-39.

174. Jiang W, Tan Y, Cai M, Zhao T, Mao F, Zhang X, et al. Human Umbilical Cord MSC-Derived Exosomes Suppress the Development of CCl4-Induced Liver Injury through Antioxidant Effect. Stem Cells Int. 2018; 2018: 6079642.

175. Li T, Yan Y, Wang B, Qian H, Zhang X, Shen L, et al. Exosomes derived from human umbilical cord mesenchymal stem cells alleviate liver fibrosis. Stem Cells Dev. 2013; 22: 845-54.

176. Li X, Liu L, Yang J, Yu Y, Chai J, Wang L, et al. Exosome Derived From Human Umbilical Cord Mesenchymal Stem Cell Mediates MiR-181c Attenuating Burn-induced Excessive Inflammation. EBioMedicine. 2016; 8: 72-82.

177. Loy H, Kuok DIT, Hui KPY, Choi MHL, Yuen W, Nicholls JM, et al. Therapeutic implications of human umbilical cord mesenchymal stromal cells in attenuating influenza A/H5N1-associated acute lung injury. J Infect Dis. 2018.

178. Sun L, Xu R, Sun X, Duan Y, Han Y, Zhao Y, et al. Safety evaluation of exosomes derived from human umbilical cord mesenchymal stromal cell. Cytotherapy. 2016; 18: 413-22.

179. Wang L, Gu Z, Zhao X, Yang N, Wang F, Deng A, et al. Extracellular Vesicles Released from Human Umbilical Cord-Derived Mesenchymal Stromal Cells Prevent Life-Threatening Acute Graft-Versus-Host Disease in a Mouse Model of Allogeneic Hematopoietic Stem Cell Transplantation. Stem Cells Dev. 2016; 25: 1874-83.

180. Xiong ZH, Wei J, Lu MQ, Jin MY, Geng HL. Protective effect of human umbilical cord mesenchymal stem cell exosomes on preserving the morphology and angiogenesis of placenta in rats with preeclampsia. Biomed Pharmacother. 2018; 105: 1240-7.

181. Zhao X, Wu X, Qian M, Song Y, Wu D, Zhang W. Knockdown of TGF-beta1 expression in human umbilical cord mesenchymal stem cells reverts their exosome-mediated EMT promoting effect on lung cancer cells. Cancer Lett. 2018; 428: 34-44.

182. Zou XY, Yu Y, Lin S, Zhong L, Sun J, Zhang G, et al. Comprehensive miRNA Analysis of Human Umbilical Cord-Derived Mesenchymal Stromal Cells and Extracellular Vesicles. Kidney Blood Press Res. 2018; 43: 152-61.

183. Mutlu BR, Edd JF, Toner M. Oscillatory inertial focusing in infinite microchannels. Proc Natl Acad Sci U S A. 2018; 115: 7682-7.

184. Oeyen E, Van Mol K, Baggerman G, Willems H, Boonen K, Rolfo C, et al. Ultrafiltration and size exclusion chromatography combined with asymmetrical-flow field-flow fractionation for the isolation and characterisation of extracellular vesicles from urine. J Extracell Vesicles. 2018; 7: 1490143.

185. Gupta S, Rawat S, Arora V, Kottarath SK, Dinda AK, Vaishnav PK, et al. An improvised one-step sucrose cushion ultracentrifugation method for exosome isolation from culture supernatants of mesenchymal stem cells. Stem Cell Res Ther. 2018; 9: 180.

186. Diaz G, Bridges C, Lucas M, Cheng Y, Schorey JS, Dobos KM, et al. Protein Digestion, Ultrafiltration, and Size Exclusion Chromatography to Optimize the Isolation of Exosomes from Human Blood Plasma and Serum. J Vis Exp. 2018.

187. Altanerova U, Babincova M, Babinec P, Benejova K, Jakubechova J, Altanerova V, et al. Human mesenchymal stem cell-derived iron oxide exosomes allow targeted ablation of tumor cells via magnetic hyperthermia. Int J Nanomedicine. 2017; 12: 7923-36.

188. Lee JK, Park SR, Jung BK, Jeon YK, Lee YS, Kim MK, et al. Exosomes derived from mesenchymal stem cells suppress angiogenesis by down-regulating VEGF expression in breast cancer cells. PLoS One. 2013; 8: e84256.

189. Ge P, Sheng F, Jin Y, Tong L, Du L, Zhang L, et al. Magnetic resonance imaging of osteosarcoma using a bis(alendronate)-based bone-targeted contrast agent. Biomed Pharmacother. 2016; 84: 423-9.

190. Kobayashi H, Sato N, Kawamoto S, Saga T, Hiraga A, Ishimori T, et al. 3D MR angiography of intratumoral vasculature using a novel macromolecular MR contrast agent. Magn Reson Med. 2001; 46: 579-85.

191. Betzer O, Perets N, Angel A, Motiei M, Sadan T, Yadid G, et al. In Vivo Neuroimaging of Exosomes Using Gold Nanoparticles. ACS Nano. 2017; 11: 10883-93.

192. Otero-Ortega L, Gomez de Frutos MC, Laso-Garcia F, Rodriguez-Frutos B, Medina-Gutierrez E, Lopez JA, et al. Exosomes promote restoration after an experimental animal model of intracerebral hemorrhage. J Cereb Blood Flow Metab. 2018; 38: 767-79.

193. Rana S, Yue S, Stadel D, Zoller M. Toward tailored exosomes: the exosomal tetraspanin web contributes to target cell selection. Int J Biochem Cell Biol. 2012; 44: 1574-84.

194. Rana S, Zoller M. Exosome target cell selection and the importance of exosomal tetraspanins: a hypothesis. Biochem Soc Trans. 2011; 39: 559-62.

195. MacEwen EG, Pastor J, Kutzke J, Tsan R, Kurzman ID, Thamm DH, et al. IGF-1 receptor contributes to the malignant phenotype in human and canine osteosarcoma. J Cell Biochem. 2004; 92: 77-91.

Appendix A

Table 12. List of antibodies for Flow cytometry of Mesenchymal Stroma Cells.

Antibody name	Description	Cat. #	Brand
CD90 FITC (Clone: 5E10)	hMSC Positive Cocktail	51-9007663	BD Bioscience
CD105 PerCP-Cy5.5 (Clone: 266)			
CD73 APC (Clone: AD2)			
mIgG1, κ FITC (Clone: X40)	hMSC Positive Isotype Control Cocktail	51-9007664	BD Bioscience
mIgG1, κ PerCP-Cy5.5 (Clone: X40)			
mIgG1, κ APC (Clone: X40)			
CD34 PE (Clone:581)	PE hMSC Negative Cocktail	51-9007661	BD Bioscience
CD11b PE (Clone: ICRF44)			
CD19 PE (Clone: HIB19)			
CD45 PE (Clone: HI30)			
HLA-DR PE (Clone: G46-6)			
mIgG1, κ PE (Clone: X40)	PE hMSC Negative Isotype Control Cocktail	51-9007662	BD Bioscience
mIgG2a, κ PE (Clone:G155-178)			
CD90 FITC (Clone: 5E10)	FITC Mouse Anti-human CD90	51-9007657	BD Bioscience
CD44 PE (Clone: G44-26)	PE Mouse Anti-Human CD44	51-9007656	BD Bioscience
CD105 PerCP-CyTM5.5 (Clone: 266)	PerCP-CyTM5.5 Mouse Anti-Human CD105	51-9007648	BD Bioscience
CD73 APC (Clone:AD2)	APC Mouse Anti-Human CD73	51-9007649	BD Bioscience
mIgG2b, κ (Clone: 27-35)	PE Mouse IgG2b, κ Isotype Control	51-9007655	BD Bioscience

Table 13. List of antibodies for Exosomes Characterization.

Antibody name	Description	Cat. #	Brand
CD 9 (C-4)	Tetraspanin, mouse monoclonal	sc-13118	Santa Cruz Biotecnology Inc.
CD 63 (MX-49.129.5)	Tetraspanin, mouse monoclonal	sc-5275	Santa Cruz Biotecnology Inc.
CD 81 (5A6)	Tetraspanin, mouse monoclonal	sc-23962	Santa Cruz Biotecnology Inc.
HSP 70	Heat shock proteins 70 kDa	sc-32239	Santa Cruz Biotecnology Inc.
Na+/K+-ATPase β3 (46)	Oligomeric plasma membrane complex	sc-135998	Santa Cruz Biotecnology Inc.
m-IgGκ BP-HRP	anti-mouse IgG secondary antibodies conjugated to horseradish peroxidase (HRP)	sc-516102	Santa Cruz Biotecnology Inc.
β-Actin (8H10D10)	Monoclonal antibody human β-actin.	3700	Cell Signaling Technology

Appendix B

Analysis of HUC-MSC-293 by flow cytometry.

Batch Analysis Report

Run Date: 2/21/18 2:16 PM Experiment: 9Feb18
User ID: Guest
Statistics Output: N/A
Worksheet PDF Output: D:\BDExport\Reports\Batch Analysis Reports\9Feb18-Batch_Analysis_2102 2018141602.pdf

Specimen_001

Tube	Status	Run Time
FMO1	OK	2/21/18 2:16 PM
FMO2	OK	2/21/18 2:16 PM
FMO3	OK	2/21/18 2:16 PM
FMO4	OK	2/21/18 2:16 PM
Isotype	OK	2/21/18 2:16 PM
Cocktail	OK	2/21/18 2:16 PM
Positive Isotype	OK	2/21/18 2:16 PM
Positive Cocktail	OK	2/21/18 2:16 PM

Compensation Controls

Tube	Status	Run Time
Unstained Control	OK	2/21/18 2:16 PM
FITC Stained Control	OK	2/21/18 2:16 PM
PE Stained Control	OK	2/21/18 2:16 PM
PerCP-Cy5-5 Stained Control	OK	2/21/18 2:16 PM
APC Stained Control	OK	2/21/18 2:16 PM

BD FACSDiva 8.0.1

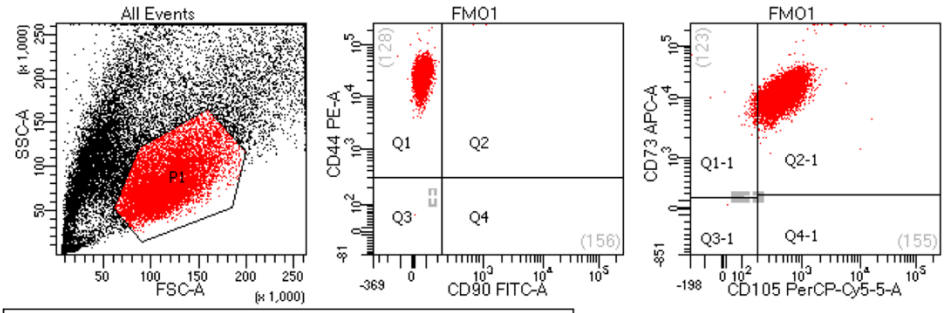

Tube: FMO1

Population	#Events	%Parent	%Total
All Events	25,016	####	100.0
P1	10,000	40.0	40.0
Q1	9,997	100.0	40.0
Q2	2	0.0	0.0
Q3	1	0.0	0.0
Q4	0	0.0	0.0
Q1-1	162	1.6	0.6
Q2-1	9,837	98.4	39.3
Q3-1	1	0.0	0.0
Q4-1	0	0.0	0.0

FMO1 (-) CD90

Tube #: 6

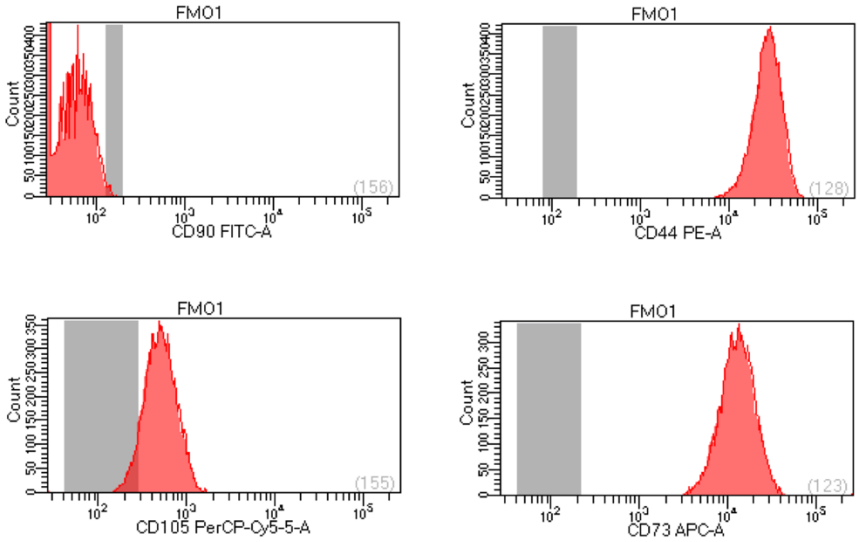

BD FACSDiva 8.0.1

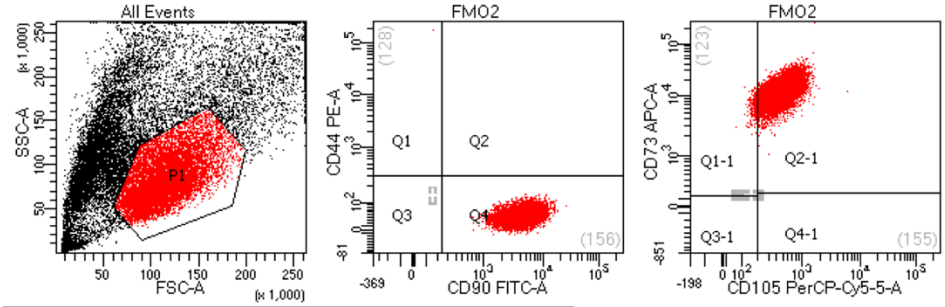

Tube: FMO2

Population	#Events	%Parent	%Total
All Events	24,630	####	100.0
P1	10,000	40.6	40.6
Q1	1	0.0	0.0
Q2	0	0.0	0.0
Q3	0	0.0	0.0
Q4	9,999	100.0	40.6
Q1-1	240	2.4	1.0
Q2-1	9,760	97.6	39.6
Q3-1	0	0.0	0.0
Q4-1	0	0.0	0.0

FMO2 (-) CD44

Tube #: 7

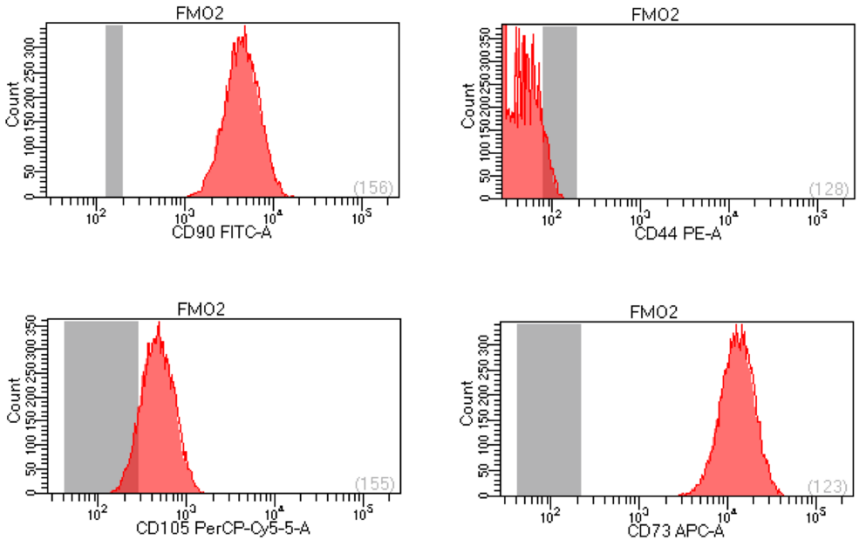

BD FACSDiva 8.0.1

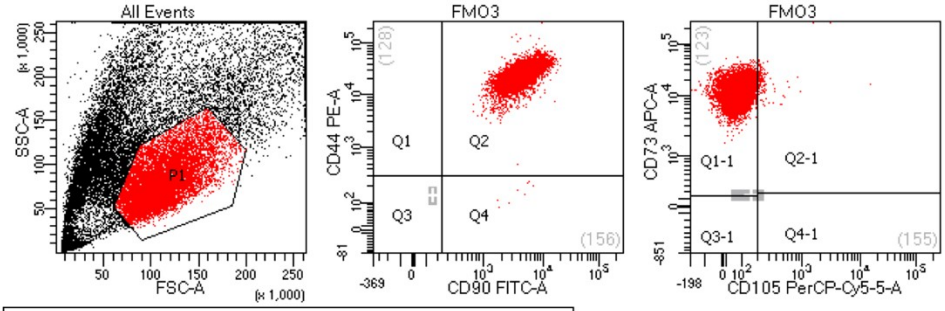

Tube: FMO3

Population	#Events	%Parent	%Total
All Events	25,116	####	100.0
P1	10,000	39.8	39.8
Q1	0	0.0	0.0
Q2	9,992	99.9	39.8
Q3	0	0.0	0.0
Q4	8	0.1	0.0
Q1-1	9,856	98.6	39.2
Q2-1	144	1.4	0.6
Q3-1	0	0.0	0.0
Q4-1	0	0.0	0.0

FMO3 (-) CD105

Tube #: 8

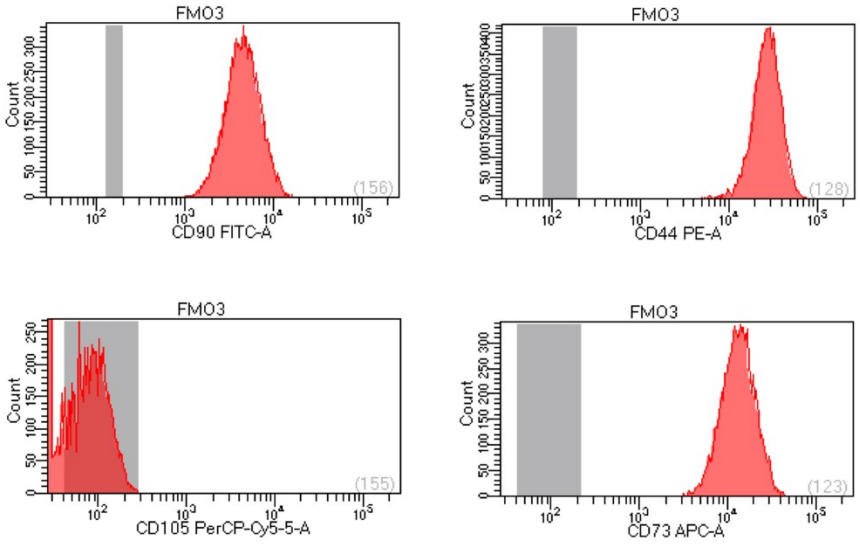

Global Sheet2

Printed on: Wed Feb 21, 2018 02:16:16 CST

BD FACSDiva 8.0.1

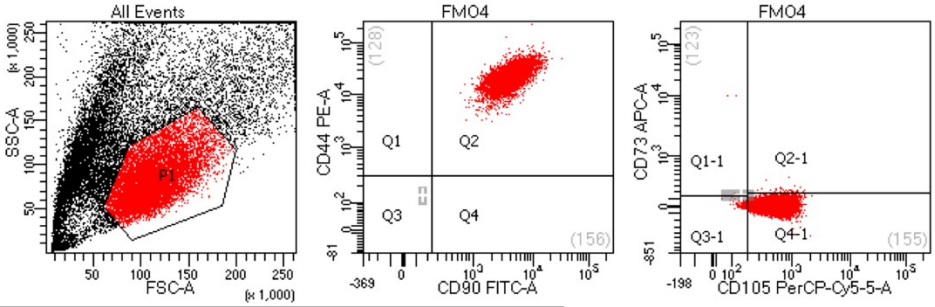

Tube: FMO4

Population	#Events	%Parent	%Total
All Events	24,186	####	100.0
P1	10,000	41.3	41.3
Q1	0	0.0	0.0
Q2	10,000	100.0	41.3
Q3	0	0.0	0.0
Q4	0	0.0	0.0
Q1-1	5	0.0	0.0
Q2-1	45	0.4	0.2
Q3-1	204	2.0	0.8
Q4-1	9,746	97.5	40.3

FMO4 (-) CD73

Tube #: 9

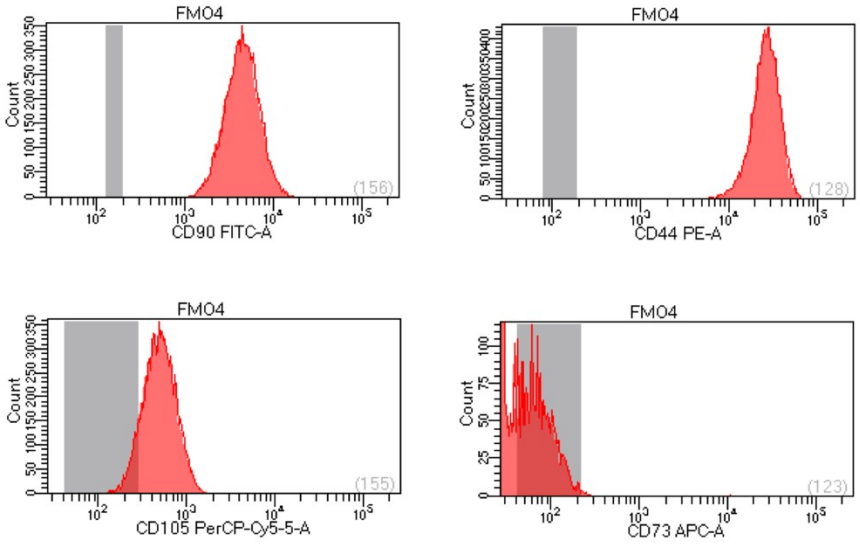

BD FACSDiva 8.0.1

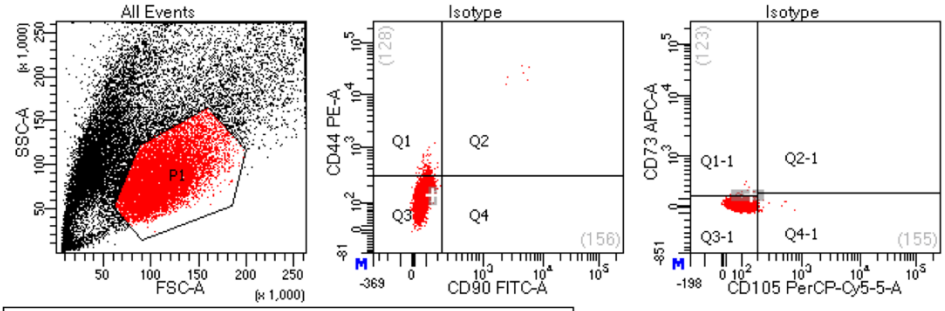

Tube: Isotype

Population	#Events	%Parent	%Total
All Events	25,976	####	100.0
P1	10,000	38.5	38.5
Q1	128	1.3	0.5
Q2	6	0.1	0.0
Q3	9,866	98.7	38.0
Q4	0	0.0	0.0
Q1-1	20	0.2	0.1
Q2-1	0	0.0	0.0
Q3-1	9,957	99.6	38.3
Q4-1	23	0.2	0.1

hMSC Positive Isotype Control Cocktail

PE hMSC Negative Isotype Control Cocktail

Tube #: 10

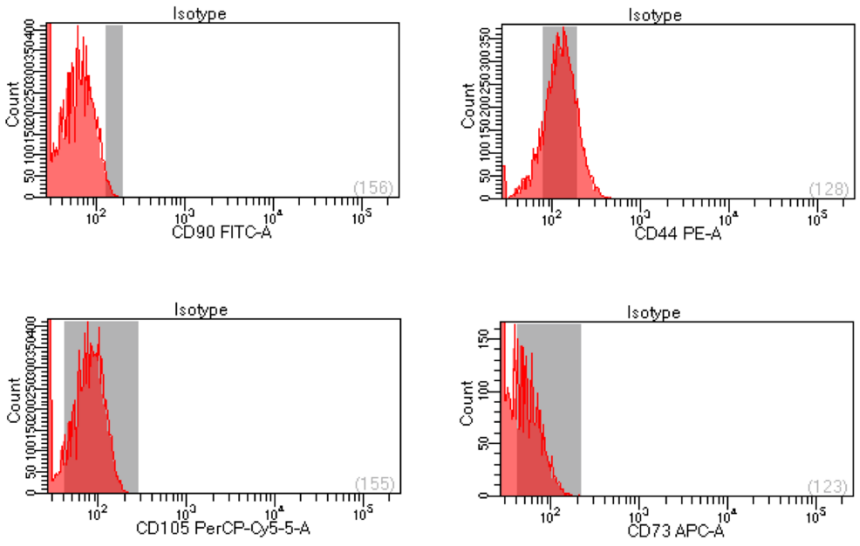

Global Sheet2

Printed on: Wed Feb 21, 2018 02:16:17 CST

BD FACSDiva 8.0.1

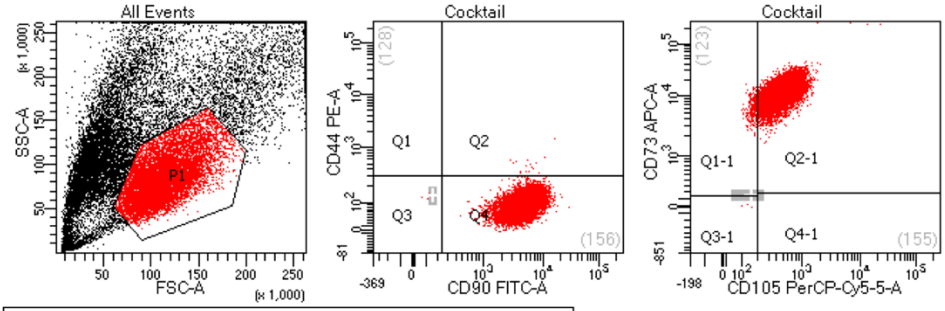

Tube: Cocktail

Population	#Events	%Parent	%Total
All Events	24,941	####	100.0
P1	10,000	40.1	40.1
Q1	0	0.0	0.0
Q2	16	0.2	0.1
Q3	4	0.0	0.0
Q4	9,980	99.8	40.0
Q1-1	324	3.2	1.3
Q2-1	9,672	96.7	38.8
Q3-1	4	0.0	0.0
Q4-1	0	0.0	0.0

hMSC Positive Cocktail

PE hMSC Negative Cocktail

Tube #: 11

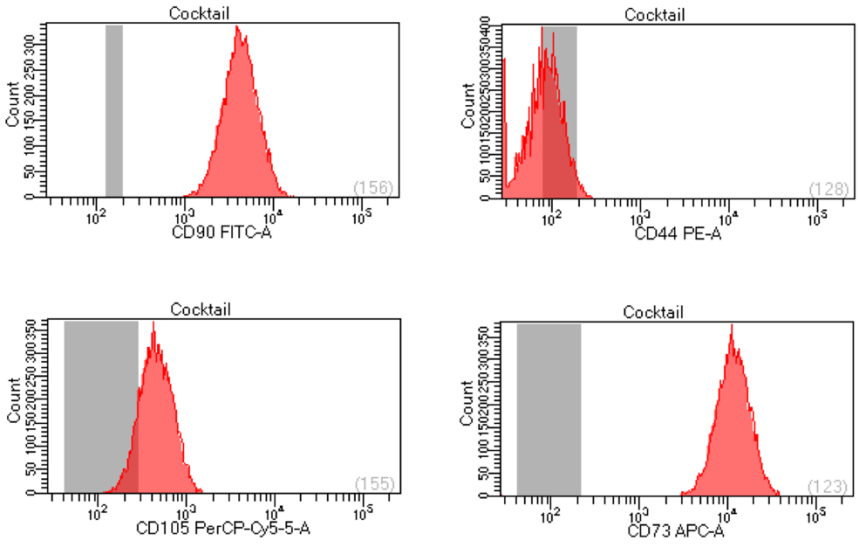

BD FACSDiva 8.0.1

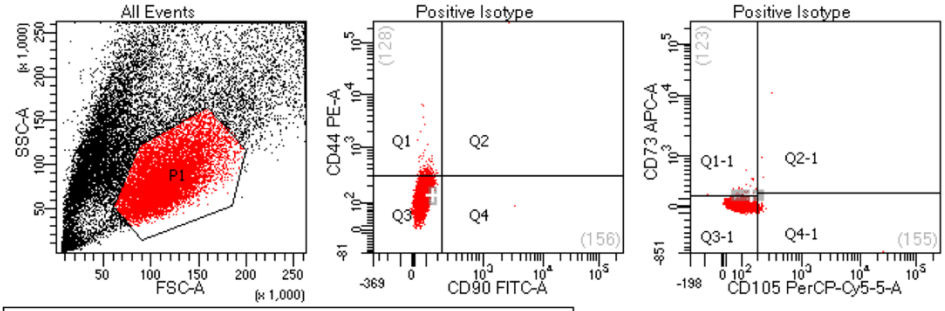

Tube: Positive Isotype

Population	#Events	%Parent	%Total
All Events	24,903	####	100.0
P1	10,000	40.2	40.2
Q1	185	1.8	0.7
Q2	1	0.0	0.0
Q3	9,813	98.1	39.4
Q4	1	0.0	0.0
Q1-1	29	0.3	0.1
Q2-1	3	0.0	0.0
Q3-1	9,926	99.3	39.9
Q4-1	42	0.4	0.2

hMSC Positive Isotype Control Cocktail

PE Mouse IgG, k Isotype Control

Tube #: 12

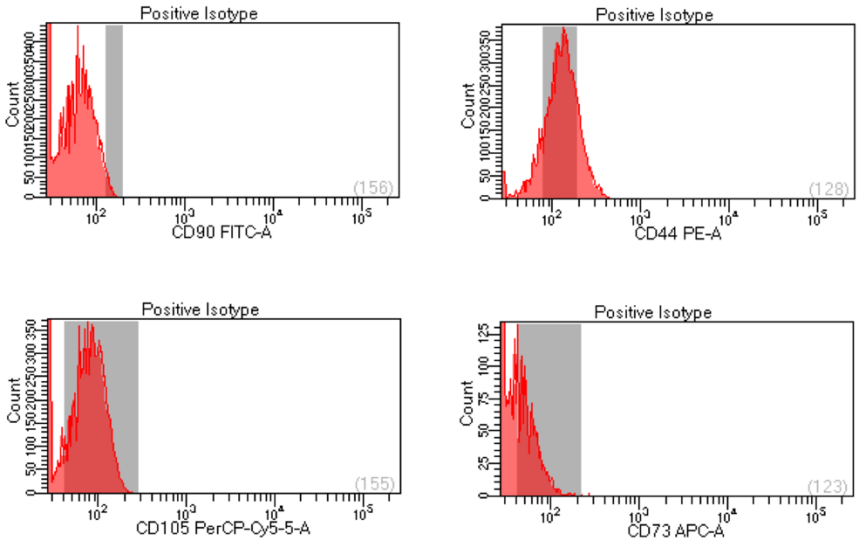

BD FACSDiva 8.0.1

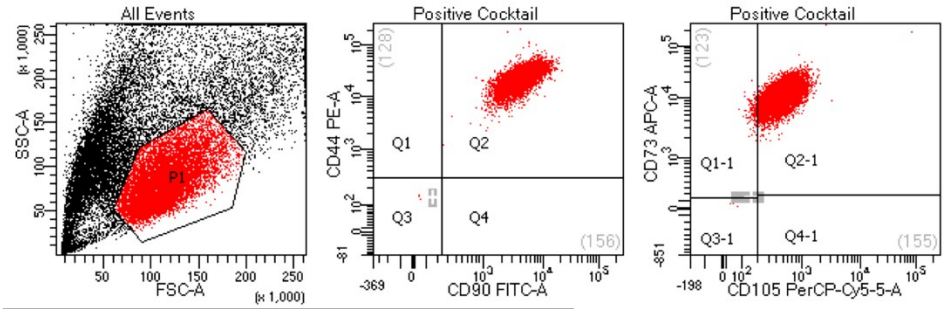

Tube: Positive Cocktail

Population	#Events	%Parent	%Total
All Events	25,232	####	100.0
P1	10,000	39.6	39.6
Q1	0	0.0	0.0
Q2	9,997	100.0	39.6
Q3	3	0.0	0.0
Q4	0	0.0	0.0
Q1-1	146	1.5	0.6
Q2-1	9,851	98.5	39.0
Q3-1	3	0.0	0.0
Q4-1	0	0.0	0.0

hMSC Positive Cocktail

PE Mouse Anti-Human CD44

Tube #: 13

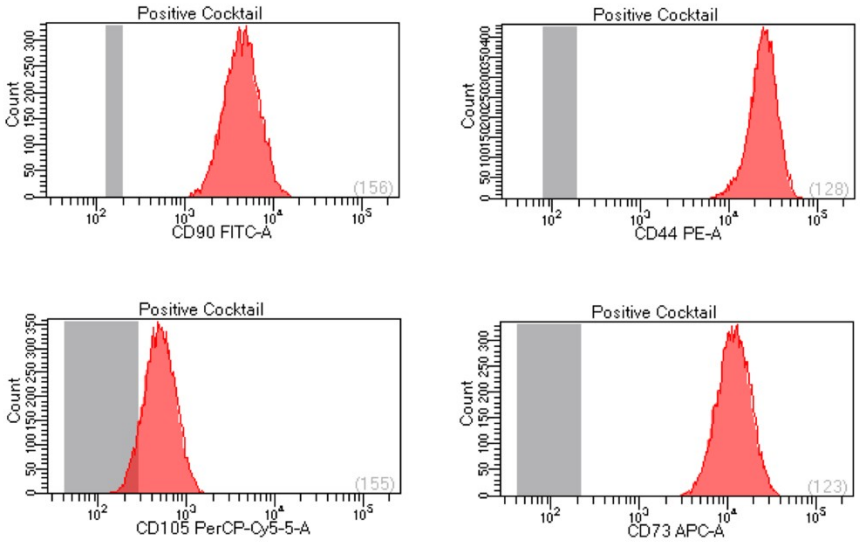

BD FACSDiva 8.0.1

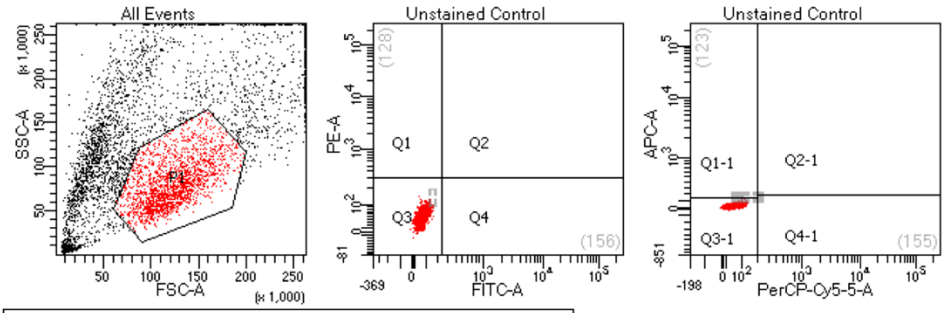

Tube: Unstained Control

Population	#Events	%Parent	%Total
All Events	5,000	####	100.0
P1	1,886	37.7	37.7
Q1	0	0.0	0.0
Q2	0	0.0	0.0
Q3	1,886	100.0	37.7
Q4	0	0.0	0.0
Q1-1	0	0.0	0.0
Q2-1	0	0.0	0.0
Q3-1	1,886	100.0	37.7
Q4-1	0	0.0	0.0

Unstained Control

Tube #: 5

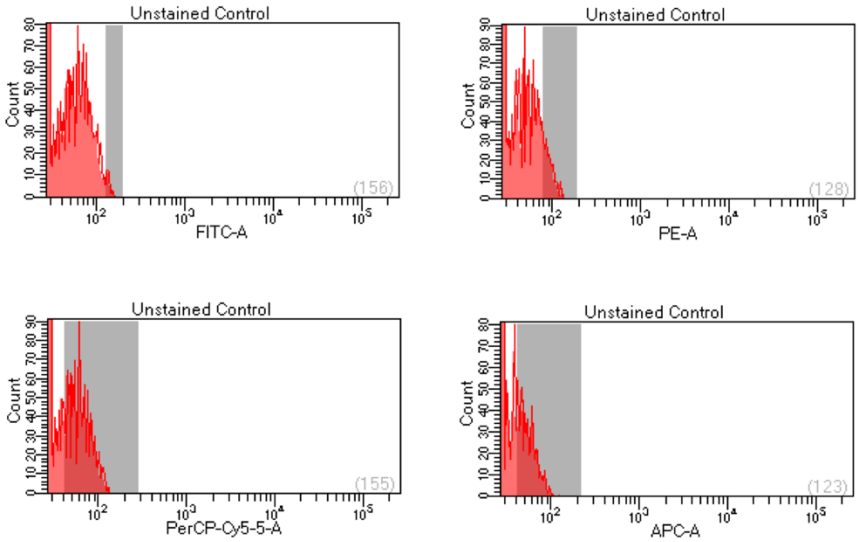

Global Sheet2

Printed on: Wed Feb 21, 2018 02:16:20 CST

BD FACSDiva 8.0.1

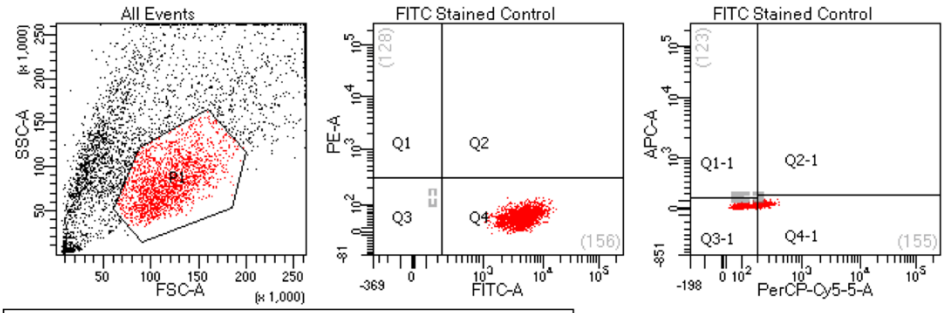

Tube: FITC Stained Control

Population	#Events	%Parent	%Total
All Events	5,000	####	100.0
P1	1,890	37.8	37.8
Q1	0	0.0	0.0
Q2	0	0.0	0.0
Q3	0	0.0	0.0
Q4	1,890	100.0	37.8
Q1-1	0	0.0	0.0
Q2-1	0	0.0	0.0
Q3-1	1,545	81.7	30.9
Q4-1	345	18.3	6.9

FITC CD90

Tube #: 1

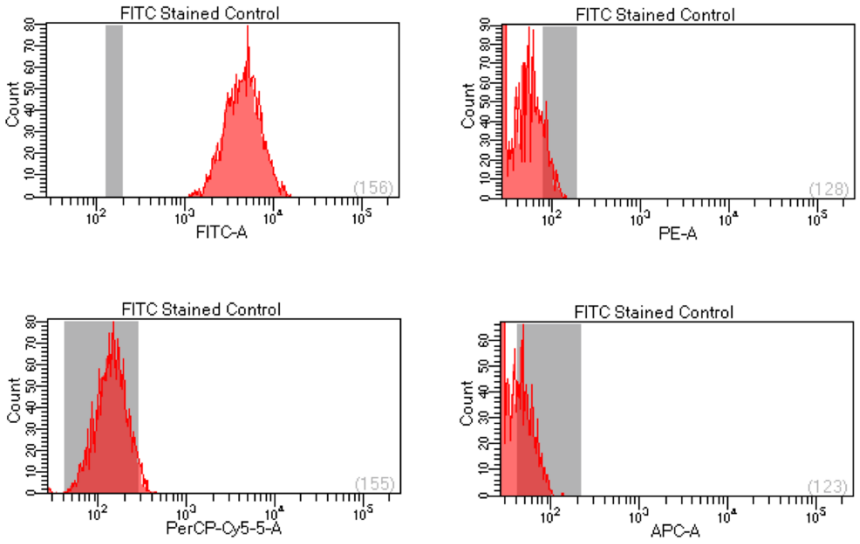

BD FACSDiva 8.0.1

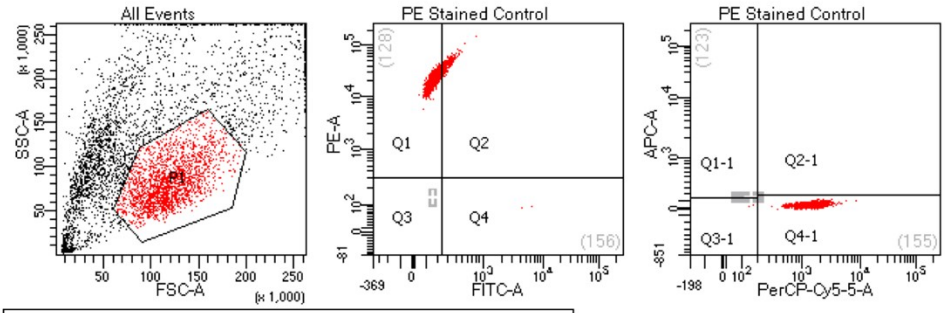

Tube: PE Stained Control

Population	#Events	%Parent	%Total
All Events	5,000	####	100.0
P1	1,945	38.9	38.9
Q1	1,609	82.7	32.2
Q2	334	17.2	6.7
Q3	0	0.0	0.0
Q4	2	0.1	0.0
Q1-1	0	0.0	0.0
Q2-1	0	0.0	0.0
Q3-1	2	0.1	0.0
Q4-1	1,943	99.9	38.9

PE CD44

Tube #: 2

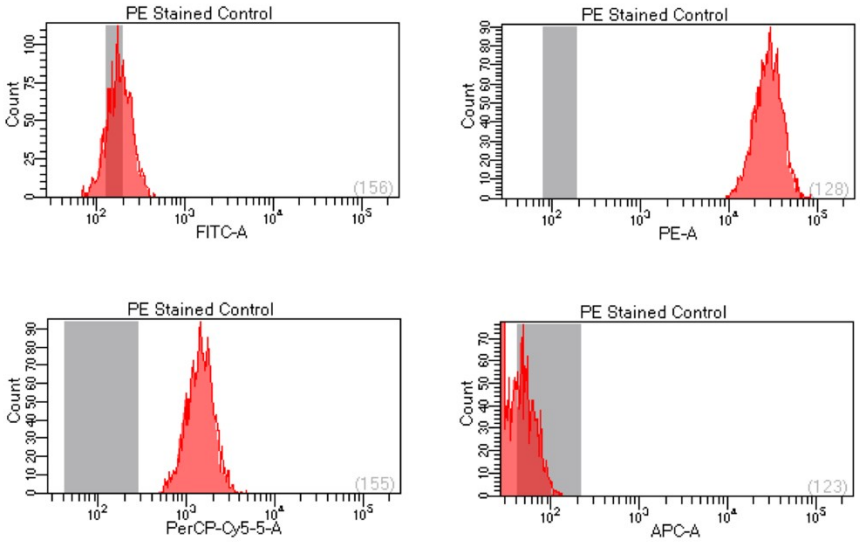

BD FACSDiva 8.0.1

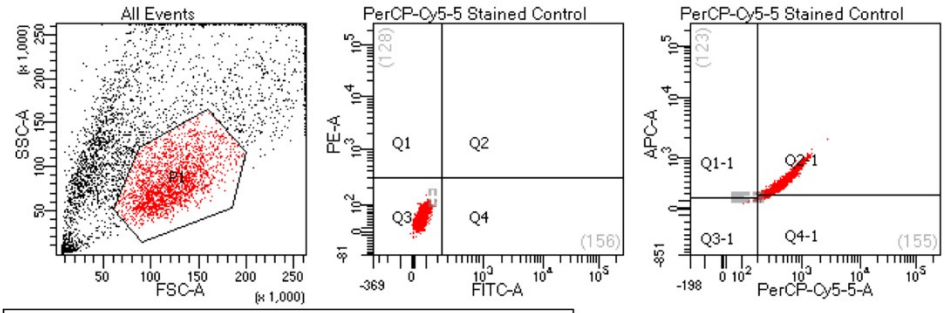

Tube: PerCP-Cy5-5 Stained Control

Population	#Events	%Parent	%Total
All Events	5,000	####	100.0
P1	1,977	39.5	39.5
Q1	0	0.0	0.0
Q2	0	0.0	0.0
Q3	1,977	100.0	39.5
Q4	0	0.0	0.0
Q1-1	10	0.5	0.2
Q2-1	1,781	90.1	35.6
Q3-1	32	1.6	0.6
Q4-1	154	7.8	3.1

PerCp-Cy 5.5 CD105

Tube #: 3

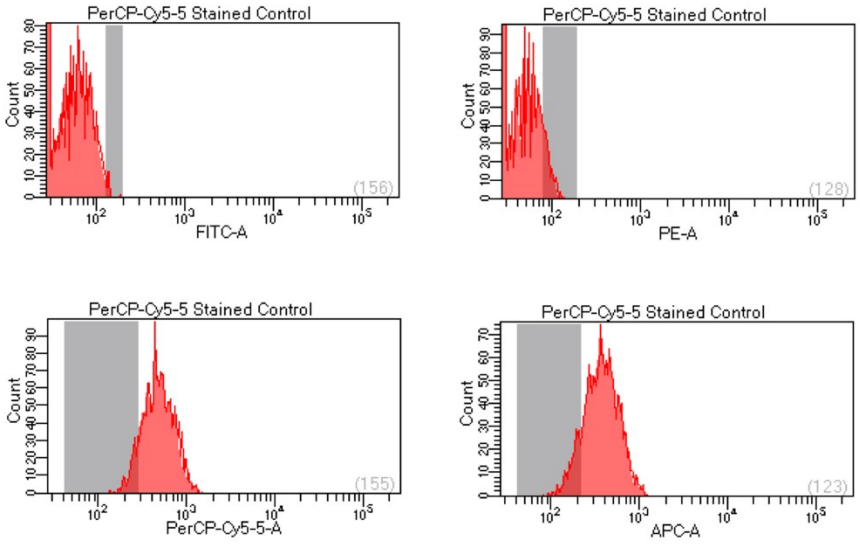

BD FACSDiva 8.0.1

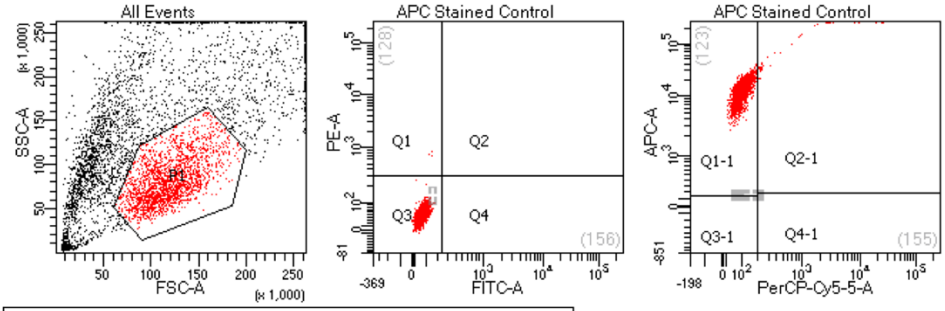

Tube: APC Stained Control

Population	#Events	%Parent	%Total
All Events	5,000	####	100.0
P1	1,917	38.3	38.3
Q1	3	0.2	0.1
Q2	0	0.0	0.0
Q3	1,914	99.8	38.3
Q4	0	0.0	0.0
Q1-1	1,872	97.7	37.4
Q2-1	45	2.3	0.9
Q3-1	0	0.0	0.0
Q4-1	0	0.0	0.0

APC CD73

Tube #: 4

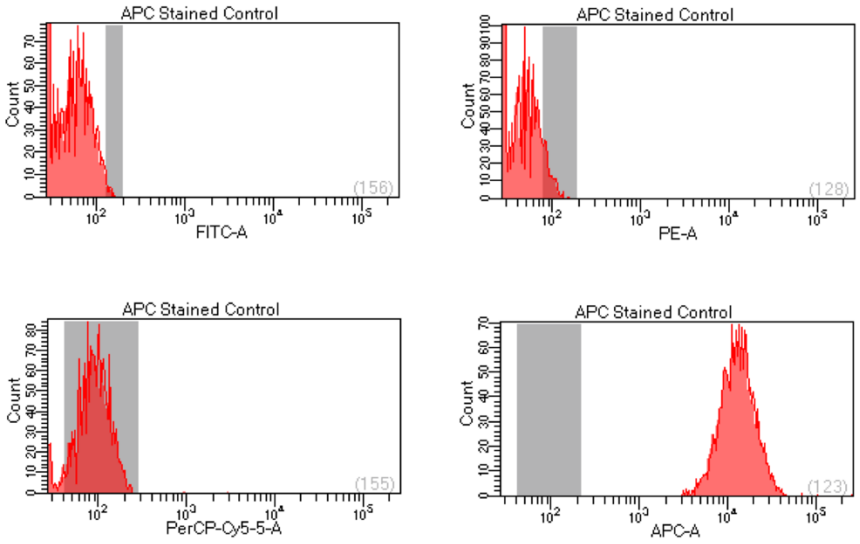

Appendix C

Table 14. List of chemicals used in each experiment.

Experiment	Chemicals	Cat.#	Brand
Human Umbilical Cord Mesenchymal Stromal Cells isolation	Povidone Iodine Prep solution	1416	Dynarex Corp.
	1 % antibiotic-antimycotic	15240062	Gibco™
	Dulbecco's phosphate buffered saline	14190144	Gibco™
	Collagenase Type I	17100017	Thermo Fisher Scientific
	Hyaluronidase		
	Calcium chloride	C79-500	Fisher Scientific
	red blood cell lysing buffer Hybri-Max™	R7775-100	Sigma-Aldrich
	acridine orange/propidium iodide	CS2-0106	Nexcelom Bioscience
	StemPro® kits	A10070-01, A10071-01, A10072-01	Thermo Fisher Scientific
	BD Stemflow™ assay kit	562245	BD Stemflow™
Synthesis of Gadolinium Lipid	1,2-distearoyl-sn-glycero-3-phosphoethanolamine (DSPE)	850715	Avanti lipid
	triethylamine	AC157910025	Sigma-Aldrich
	1,4,7,10-Tetraazacyclododecane-1,4,7,10-tetraacetic acid mono-N-hydroxysuccinimide ester (DOTA-NHS ester)	170908-81-3	Macrocyclics
	Gadolinium acetate	325678	Sigma-Aldrich
Labeling of exosomes	L-α-Phosphatidylethanolamine-N-(lissamine rhodamine B sulfonyl) (Ammonium Salt) (Egg Liss Rhod PE)	810146C	Avanti lipid

	DiR'; DiIC18(7) (1,1'-Dioctadecyl-3,3,3',3'-Tetramethylindotricarbocyanine Iodide)	D12731	Thermo Fisher Scientific
Transmission Electron Microscopy	Uranyl acetate	22400	Electron Microscopy Sciences
Protein Quantification	bicinchoninic acid assay	786571	G-Bioscience
Whole Cell lysate preparation	lysis buffer- Pierce® RIPA Buffer	89900	Thermo Fisher Scientific
	phosphatase inhibitor	1862495	Thermo Fisher Scientific
	protease inhibitor	1862209	Thermo Fisher Scientific
Exosomes Lysis	LDS Sample Buffer	NP0007	Thermo Fisher Scientific
SDS-PAGE	Tris-Glycine polyacrylamide gels	10XP04125BOX	Thermo Scientific, Inc. Novex™
	pre-stained protein standard	LC5800	Thermo Fisher Scientific, Inc. Novex®
Protein Transfer	Polyvinylidene fluoride (PVDF) membrane	Merck Millipore Ltd., Immobilon®-P	IPVH00010
	Ponceau S solution	P7170	Sigma-Aldrich
Immuno Blotting	non-fat dry milk	170-6404	Bio-Rad
	SuperSignal® West Femto substrate	34094	Thermo Fisher Scientific
GdL-labelling efficiency	Nitric acid	231-714-2	Sigma-Aldrich
Magnetic Properties of Exo-GdL	Magnevist-Diethylenetriaminepentaacetic acid gadolinium(III) dihydrogen salt hydrate	381667-25G	Sigma-Aldrich

In-vitro assays	phenol free DMEM	11054020	Gibco
	MTT (3-(4,5-Dimethylthiazol-2-yl)-2,5-Diphenyltetrazolium Bromide)	M6494	Thermo Fisher Scientific Inc
Cellular Uptake of Exosomes	DMEM	11054020	Gibco
	paraformaldehyde	P6148-500	Sigma-Aldrich
	Glutaraldehyde	111-30-8	Fisher Scientific
	4',6-diamidino-2-phenylindole	D9542-5	Sigma-Aldrich
	Fluoromount™Aqueous Mounting Medium	F4680-25	Sigma-Aldrich
Apoptosis Assay	FITC Annexin-V Apoptosis Detection Kit I		BD Pharmingen™
HUC-MSC stimulation assay	polynosinic-polycytidic acid	P9582-5MG	Sigma-Aldrich
	lipopolysaccharides of *Escherichia coli*	L31129-25MG	Sigma-Aldrich
	RNA*later*™ Stabilization Solution	AM7021	ThermoFisher Scientific
	recombinant human IFN−γ (FN−γ)	PHC4031	ThermoFisher Scientific
HUC-MSCs RNA extraction	RNeasy Mini Kit	74106	Qiagen
Synthesis of HUC-MSC complementary DNA (cDNA)	SuperScript™ IV First-Strand Synthesis System	18091200	ThermoFisher Scientific

Table 15. List of equipment used in the experiments

Experiment	Equipment	Cat.#	Brand
Human Umbilical Cord Mesenchymal Stromal Cells isolation	automatic tissue dissociator	130-093-235	GentleMACS™
	automated cell counter	Cellometer® 2000	Nexcelom Bioscience
	flow cytometer	LSR Fortessa X20	BD-Bioscience
Pooled Human Platelet Lysate Depleted Exosomes	Centrifugation	L-90K	Beckman Counter
	Swinging bucket rotor	SW-41-Ti	Beckman
Exosome Isolation	benchtop centrifuge	5810R	Eppendorf
	swing bucket rotor A-4-62	FL08517291	Eppendorf
	Centrifugation	L-90K	Beckman Counter
Labeling of exosomes	Ultrasonic	CPX-952-338R	Branson
	Sonic Vibracell	VCX130	Sonics
	Amicon Ultra-4 centrifugal filter	Z648035	Sigma-Aldrich
Dynamic Light Scattering and Z-potential	Zetasizer Nano ZS		Malvern Instruments
	folded capillary cell	DTS1070	Malvern Instruments
	disposable polystyrene cuvettes	ZEN0040	Malvern Instruments
Nanoparticle tracking Analysis	NanoSight	LM-10	Malvern Instruments
Transmission Electron Microscopy	Formvar-coated 200 mesh copper grid	215-412-8400	Electron Microscopy Science
	Tecnai™ G^2 Spirit BioTWIN		FEI™ Company
Protein Quantification	SpectraMax®i3 microplate reader		Molecular Devises
SDS-PAGE	XCell SureLock™ Mini-Cell Electrophoresis System	EI0001	Thermo Fisher Scientific
	Gel Doc™ XR+ imaging system		Bio-Rad

Protein transfer	semi-dry electrophoretic transfer system	170-3940	Bio-Rad. Trans-Blot® SD
Immuno Blotting	Kodak Image Station 4000		
GdL-labelling efficiency	inductively coupled plasma mass spectrometry	NEXion 350X	PerkinElmer
Magnetic Properties of Exo-GdL	Bruker 600 MHz Avance III with microimaging capability		Bruker
Cellular Uptake of Exosomes	Cell incubator	NU-4950	NuAire Autoflo
	8-Well Chambered Cover Glass	C8-1.5-H-N	Cellvis
	confocal laser scanning microscopy	LSM-700	Carl Zeiss
Apoptosis Assay	Flow cytometer	LSR Fortessa X20	BD-Bioscience
HUC-MSCs RNA extraction	spectrophotometer	NanoDrop™ 2000	ThermoFisher Scientific
Endpoint polymerase chain reaction	Phusion High-Fidelity PCR Master Mix	F531L	ThermoFisher Scientific
Reverse transcription polymerase chain reaction (RT-PCR)	RT2 SYBR® Green qPCR Mastermixes	330500	Qiagen
NIR bioimaging	Pearl® Trilogy imaging system		LI-COR®